Technische Universität München
Fakultät für Chemie

Max-Planck-Institut für Biochemie
Abteilung für Molekulare Strukturbiologie

Correlative cryo-electron tomography studies of artificial β-protein aggregates in mammalian cells

Tillman Klaus Schäfer

Vollständiger Abdruck der von der Fakultät für Chemie
der Technischen Universität München
zur Erlangung des akademischen Grades eines
Doktors der Naturwissenschaften (Dr. rer. nat.)
genehmigten Dissertation

Vorsitzender:	Prof. Dr. Bernd Reif
Prüfer der Dissertation:	1. Hon.-Prof. Dr. Wolfgang Baumeister
	2. Prof. Dr. Sevil Weinkauf

Die Dissertation wurde am 14.08.2018 an der Technischen Universität München eingereicht und durch die Fakultät für Chemie am 26.11.2018 angenommen.

Contents

List of Figures

List of Tables

Summary

Neurodegenerative diseases such as Alzheimer's, Parkinson's or Huntington's disease induce an increasing load on our healthcare systems, as the prevalence of these age-associated diseases is rising in our aging societies. However, after decades of research, the underlying causes of these diseases are still elusive due to their complexity and slow progression. The main commonalities in neurodegeneration are the occurrence of protein aggregates within neuronal tissue and neuronal cell death. These protein aggregates may exert toxicity on cells via two main mechanisms: loss of native function and gain of toxic function. When proteins aggregate, they lose their native function. The loss of critical protein functions can lead to toxicity effects. However, these protein aggregates can generate toxicity through aberrant interactions as well, thereby gaining a toxic function. In order to reduce the complexity and study the common effects of protein aggregation in the context of neurodegeneration, this work aims to elucidate the cellular roles of toxic gain of function in isolation. To that end, we studied artificial β-protein aggregates *in situ* using correlative cryo-electron tomography on focus ion beam milled mammalian cells. β-protein aggregation affected a variety of cellular components. Most strikingly, β-protein aggregates impaired the lysosomal system in neuronal cells. Neurons containing aggregates showed abnormally enlarged autolysosomes filled with multilamellar membrane structures, reminiscent to those observed in patients of neurodegenerative and lysosomal storage diseases. Lysosomal function was concomitantly impaired, likely due to the sequestration of AP-3 µ3A, a critical component of the lysosomal trafficking machinery, at β-protein aggregates. These findings are consistent with increasing evidence that neurodegenerative diseases are closely associated with a decline in a neurons proteostasis machinery with age, especially the lysosomal degradative system. Thus, the expression of an artificial aggregating protein recapitulates critical features of human disease. These data suggest that restoring proteostasis may be paramount to treating the effects and perhaps the causes of neurodegeneration.

Zusammenfassung

Neurodegenerative Krankheiten wie die Alzheimer, Parkinson oder Huntington Krankheit werden zunehmend zur Belastung für unsere Gesundheitssysteme, da die Prävalenz dieser altersabhängigen Krankheiten in unserer alternden Gesellschaft ansteigt. Durch ihre Komplexität und langsame Entwicklung sind, trotz jahrzehntelanger Forschung, die zugrundeliegenden Ursachen dieser Krankheiten immer noch unbekannt. Die wichtigsten Gemeinsamkeiten neurodegenerativer Krankheiten sind das Auftreten von Proteinaggregaten in neuronalem Gewebe und das Absterben neuronaler Zellen. Diese Proteinaggregate üben über zwei Hauptmechanismen Toxizität auf Zellen aus: über den Verlust ihrer nativen Funktion und das Erlangen einer toxischen Funktion. Wenn Proteine aggregieren, verlieren sie ihre native Funktion. Der Verlust kritischer Proteinfunktionen kann zu Toxizitätseffekten führen. Diese Proteinaggregate können jedoch auch durch pathologische Wechselwirkungen Toxizität erzeugen und dadurch eine toxische Funktion erlangen. Um die Komplexität der neurodegenerativen Proteinaggregation zu reduzieren und deren zugrundeliegenden Effekte zu untersuchen, zielt diese Arbeit darauf ab, allein die zellulären Effekte dieses toxischen Funktionsgewinns aufzuklären. Zu diesem Zweck wurden künstliche β-Proteinaggregate *in situ* mittels korrelativer Kryo-Elektronentomographie in Säugerzellen nach Präparation mittels fokussiertem Ionenstrahl untersucht. Eine Vielzahl von zellulären Bestandteilen war durch die β-Protein-Aggregation beeinflusst. Dabei war am auffälligsten, dass β-Proteinaggregate das lysosomale System in neuronalen Zellen beeinträchtigten. Neuronen, die Aggregate enthielten, zeigten abnorm vergrößerte Autolysosomen, die voll mit multilamellaren Membranstrukturen waren. Diese Autolysosomen zeigten Ähnlichkeiten mit solchen aus Patienten die an neurodegenerativen und lysosomalen Speicherkrankheiten leiden. Zusätzlich waren lysosomale Funktionen beeinträchtigt, was vermutlich aufgrund der Sequestrierung von AP-3 µ3A, einem kritischen Bestandteil der lysosomalen Transportmaschinerie, an ß-Proteinaggregaten beruhte. Diese Ergebnisse stimmen mit der zunehmenden Erkenntnis überein, dass neurodegenerative Erkrankungen eng mit einem Rückgang der neuronalen Proteostasemaschinerie mit zunehmendem Alter verbunden sind, insbesondere der des lysosomalen Systems. Deshalb spiegelt die Expression von künstlichen aggregierenden Proteinen kritische Merkmale menschlicher Krankheiten wider. Die aus diesen Daten gewonnenen Erkenntnisse deuten darauf hin, dass die Wiederherstellung der Proteostase für die Behandlung der Effekte der Neurodegeneration und eventuell dessen Ursachen von entscheidender Bedeutung sein kann.

1. Introduction

1.1. Neurodegenerative diseases

Neurodegenerative diseases (NDD) are an ever growing threat to human health. In 2015, the World Health Organization estimated that almost 50 million people suffer from NDDs worldwide, a number that would increase to 75 million by 2030 (WHO 2015). As these are commonly age-dependent diseases, the increasing fraction of elderly people within the population is paralleled by an increase in NDD incidence (Hardiman et al. 2016). The main common hallmarks of NDDs are the loss of neuronal cells and the occurrence of protein aggregates within neurons (Taylor, Hardy, and Fischbeck 2002). Although the explicit causes of NDDs are diverse and largely elusive, the most important risk factor is age (Beart et al. 2017). Age is important as the development of large protein aggregates is often a very slow process progressing over the time course of years, and because protective functions against protein misfolding within cells noticeably decline at old age (Klaips, Jayaraj, and Hartl 2018). Although great effort has been put into finding treatments for these diseases, their complexity and difficulty to diagnose early have led to only few successful treatments, mainly of their symptoms (Hardiman et al. 2016). The four most prevalent NDDs are Alzheimer's, Parkinson's, Huntington's and Amyotrophic lateral sclerosis (Beart et al. 2017).

Alzheimer's disease (AD) is the most common NDD, with a prevalence of 24% to 33% in people over the age of 85 (Hardiman et al. 2016). Its symptoms are characterized by an impairment in memory functions, cognitive deterioration, neuropsychiatric symptoms and functional decline (Hardiman et al. 2016). On a cellular level, AD is characterized by a loss of neuronal cells and extracellular amyloid plaques and intracellular neurofibrillary tangles. Amyloid plaques are comprised of β amyloid protein, which is produced by the cleavage of the amyloid precursor protein (APP) (Singh et al. 2016). Among others, mutations in genes involved in the cleavage of APP such as PSEN1 and PSEN2 have been associated with a high risk for AD (Karch and Goate 2015). The physiological function of APP is not fully known, but it is likely involved in processes such as neuronal growth, cell adhesion, calcium metabolism, protein trafficking and transmembrane signal transduction (Singh et al. 2016). Neurofibrillary tangles are comprised of hyperphosphorylated microtubule-associated tau proteins (Wang and Mandelkow 2016). Tau proteins bind to and stabilize microtubules and are involved in their assembly (Wang and Mandelkow 2016). Although these protein aggregates are involved in generating toxicity on neuronal cells, they are not its sole trigger, and the precise mechanism behind neuronal cell death in AD is not known (Hardiman et al. 2016).

Parkinson's disease (PD) is the second most common NDD with approximately 6.3 million patients worldwide (Hardiman et al. 2016). Among others, its symptoms are characterized by rigidity, rest tremor, postural instability, dementia and depression. On a cellular level PD is characterized by the loss of neurons in the substantia nigra pars compacta and intracellular α-synuclein aggregates called

Lewy bodies. α-synuclein is predominantly expressed in the brain and has been proposed to fulfill multiple activities such as the suppression of apoptosis, glucose level regulation, chaperone activity, neuronal differentiation and more, but its exact function is still unknown (Emamzadeh 2016). While most PD cases are of sporadic nature, mutations in a number of genes can increase the risk of PD (Emamzadeh 2016). Mutations in the genes coding for α-synuclein, Parkin, PINK1, DJ-1, LRRK2 and GBA have been associated with a higher risk for PD (Emamzadeh 2016).

Huntington's disease (HD) is one of the few NDDs for which the exact cause is known. It is an inherited disease caused by an expansion of the CAG trinucleotide (coding for glutamine) repeat in the huntingtin gene (Hardiman et al. 2016). While the expansion of CAG repeats up to 35 does not result in HD, lengths up to 39 will increase the risk of HD substantially and patients with repeat lengths of 40 and more will certainly develop HD (Nopoulos 2016). Interestingly, the length of the CAG repeats is highly correlated to the time of disease onset, and repeats larger than 50 will often cause childhood onset (Hardiman et al. 2016). HDs symptoms include behavioral changes, short-term memory loss, difficulty in voluntary movement and progressive involuntary movements (chorea), from which its alternative name Huntington's chorea is derived (Hardiman et al. 2016). HD patients show a progressive loss of neuronal cells throughout the brain, starting in the. Neurons contain large aggregates composed of mutant huntingtin protein. Huntingtin is a large, ubiquitously expressed protein and has been found to interact with more than 200 proteins (Nopoulos 2016). Although huntingtin is involved in a plethora of processes, such as vesicular transport, brain-derived neurotrophic factor production, neuronal gene transcription and has been shown to be anti-apoptotic, its native functions are not yet fully understood (Saudou and Humbert 2016). This may be significantly facilitated by the high resolution structure of huntingtin, recently solved in our group (Guo, Bin, et al. 2018).

Amyotrophic lateral sclerosis (ALS) differs from the previously described NDDs as it predominantly afflicts the motor neurons in the spinal cord, brain stem and the motor cortex (Sendtner 2014). Symptoms of ALS are therefore less often of neuropsychiatric nature and primarily afflict motor functions, beginning with symptoms such as gait disturbance or difficulty with fine movement, which progress until the majority of patients die due to respiratory failure (Hardiman et al. 2016). Protein aggregates found in afflicted neurons are comprised of a variable variety of proteins such as p62, SOD1, TDP-43, FUS, OPTN, UBQLN2, ATXN2 and dipeptide repeat proteins resulting from aberrant translation of an expansion of intronic repeats in the C9ORF72 gene (Blokhuis et al. 2013). Some of these proteins, such as FUS and TDP-43, contain low complexity domains that increase their aggregation propensity. However, why mutations in these ubiquitously expressed proteins lead to aggregation in and degeneration of motor neurons is not known (Blokhuis et al. 2013).

1.2. Protein aggregation

Although the function and structure of disease proteins differ considerably in NDDs, the major common hallmark of these diseases is the occurrence of protein aggregates. Proteins need to be folded in a specific way. However, especially large proteins and proteins with a high amount of intrinsically unstructured regions are prone to misfolding (Hartl, Bracher, and Hayer-Hartl 2011). The underlying thermodynamic properties of a protein pushes it towards a thermodynamically most stable conformation (**Figure 1.2-1**). However, this conformation is often not the same as the proteins functional conformation. In order for these large and unstructured proteins to fold into their correct conformation, they are often reliant on the proteostasis network (PN), most often in the form of chaperones to guide them during folding. The PN has been found to decline in efficiency with age (Klaips, Jayaraj, and Hartl 2018).

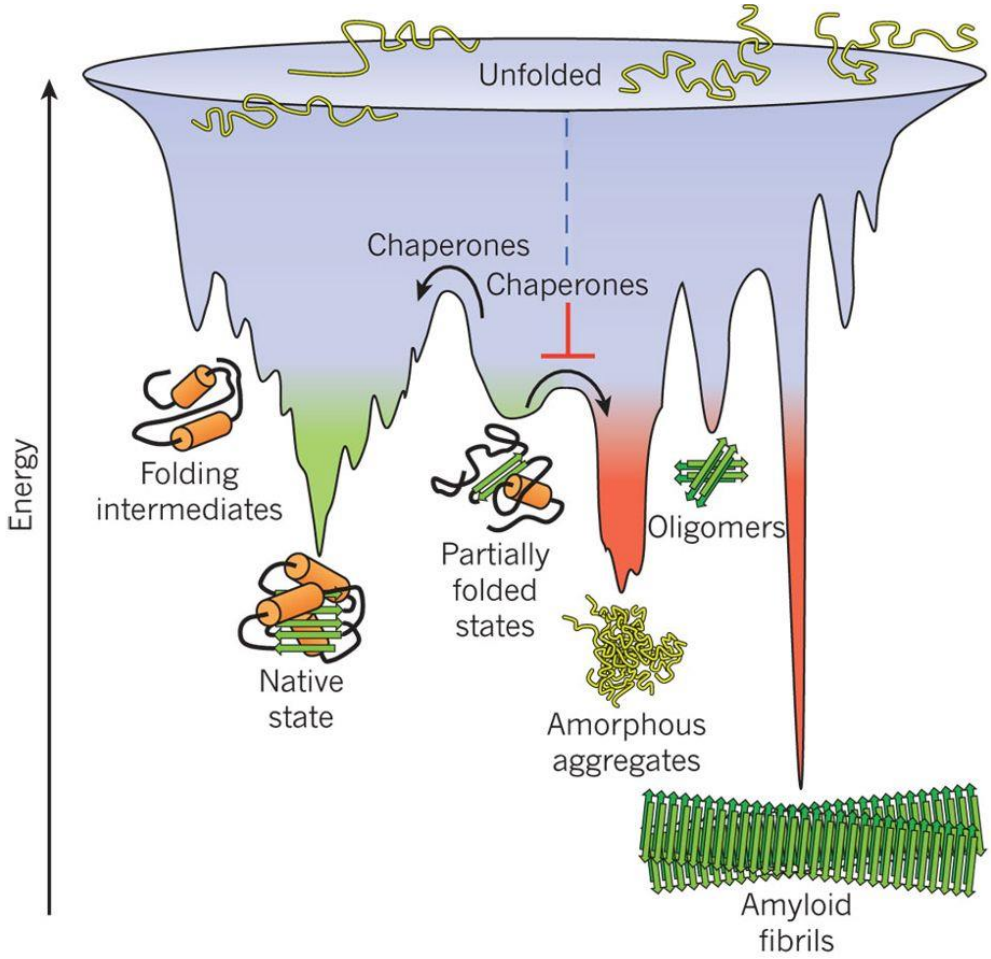

Figure 1.2-1: Scheme of thermodynamic landscape of protein folding states. Proteins may acquire different folding states situated in thermodynamic local minima. Molecular chaperones can induce correct folding states or deter thermodynamically stable, but nonnative folding states. If chaperones are hindered in their function, misfolded proteins may form more stable amyloid fibrils or amorphous aggregates. With permission from (Hartl, Bracher, and Hayer-Hartl 2011).

When proteins misfold, chaperones commonly try to induce their refolding (Hartl, Bracher, and Hayer-Hartl 2011). If this refolding does not function as well, misfolded proteins are degraded by the PN mediated through degradation by the ubiquitin-proteasome system (UPS) and by chaperone-mediated autophagy (Kaushik and Cuervo 2012). However, if the proteins are unable to be degraded and accumulate within the cytosol, they will often form protein oligomers, which may then assemble into filaments, which in turn create large aggregates (Hipp, Park, and Hartl 2014). Amyloid fibrils are formed by oligomers in which the polypeptide sequence forms β-sheets, which stack upon each other forming a cross-β fibril structure (Glabe 2008). As these aggregates are often resistant to degradation by the UPS and may even impair UPS function (Bence, Sampat, and Kopito 2001), they may be degraded via macroautophagy (Johnston, Ward, and Kopito 1998; Wong and Cuervo 2010).

Protein aggregates may exert toxicity on the cell via two general mechanisms: loss of function and gain of function toxicity (Winklhofer, Tatzelt, and Haass 2008). When proteins misfold, they not only burden the PN and might form aggregates, but very importantly do not function in the way they are intended to. If only small numbers of a specific protein are misfolded, cells may be able to compensate by increasing the expression levels of that particular protein. However, if a large portion of the proteins are misfolded, their cellular function will be compromised. This can exert toxicity on the cell, as downstream cellular mechanisms which are dependent on the native function of the misfolded protein are also impaired (Winklhofer, Tatzelt, and Haass 2008). This toxic loss of function effect is increased by the sequestration properties of many aggregates, which act as a protein sink of newly formed proteins, increasing the toxicity of the loss of this proteins function in a vicious circle (Yang and Hu 2016). Complicating this further, the functions of many proteins forming aggregates in NDDs are not very well known (Hiltunen, van Groen, and Jolkkonen 2009; Hardiman et al. 2016; Emamzadeh 2016). Loss of function toxicity effects may therefore be difficult to identify as such.

At the same time, protein aggregates can directly interact with cellular components, therefore gaining a toxic function (Winklhofer, Tatzelt, and Haass 2008). These toxicity effects may be very diverse in their nature. Aggregates and the fibrils they are comprised of have been shown to interact with a whole array of proteins and organelles (Hosp et al. 2017; Chiti and Dobson 2017). These interactions can lead to damage of the interaction partner, for example the disruption of membranes (Bauerlein et al. 2017; Milanesi et al. 2012), but may also hinder the interaction partner in fulfilling its native function (Hosp et al. 2017). For example, if an interacting protein is permanently sequestered, it is thus removed from the pool of functional proteins. Protein aggregates may also detract large numbers of critical elements of the PN (Guo, Lehmer, et al. 2018), which lack in the rest of the cell, leading to further toxicity effects (Labbadia and Morimoto 2015). The presence of protein aggregates and damaged neurons within the brain also induces an inflammatory response which, when chronically induced, can lead to further deterioration (Chitnis and Weiner 2017). For instance, amyloid plaques consistent of amyloid β induce inflammatory responses which can lead to further neuronal damage, but also impairment of the neuroinflammatory response itself, increasing the toxicity effects of amyloid β (Wyss-Coray and Rogers 2012; Belanger and Magistretti 2009).

1.3. The autophagy-lysosomal system is impaired in neurodegeneration

One major common deficiency in NDDs is the impairment of the autophagy-lysosomal system. Autophagy is an important component of the PN that has been found to decline during aging (Hipp, Park, and Hartl 2014). This is especially true in long living, postmitotic cells such as neurons, which cannot relieve toxicity effects of protein misfolding by retention of aggregates within one cell during mitosis (Wang et al. 2018). Unlike the degradation of proteins by the UPS, autophagy is capable of degrading not only single proteins (Cuervo and Wong 2014), but also whole aggregates and even organelles such as mitochondria (Hubbard et al. 2012).

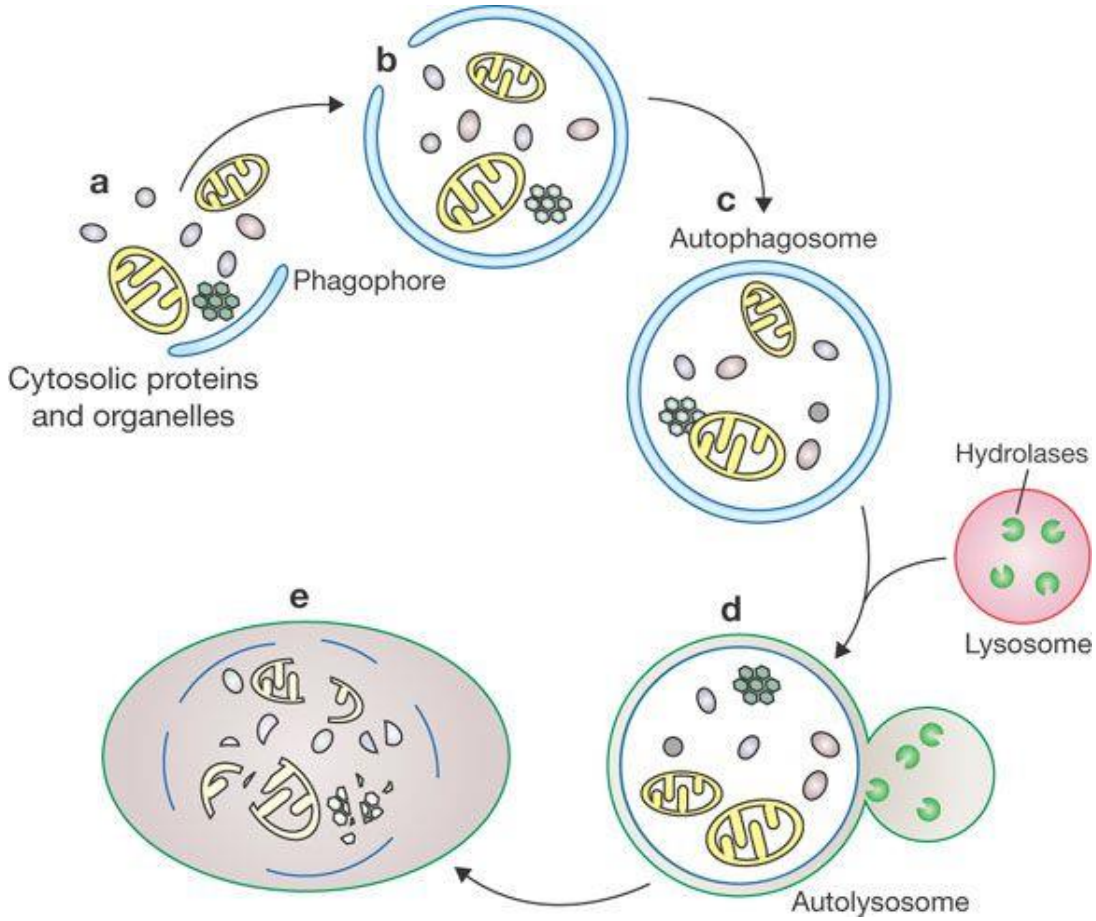

Figure 1.3-1: Scheme of autophagy system. (a, b) Cellular material is engulfed by a cup shaped phagophore, (c) which fuses at its opening during maturation, forming an autophagosome. (d) The autophagosome fuses with a lysosome containing hydrolytic enzymes, creating an autolysosome. (e) Hydrolases are released into the autolysosome lumen and degrade its cargo. With permission from (Xie and Klionsky 2007).

In autophagy cellular material designated for degradation is engulfed by a cup shaped pre-autophagic membrane structure termed phagophore (**Figure 1.3-1 a, b**) (Nixon 2007). During its maturation, the phagophore closes up at the cup opening, forming an autophagosome (**Figure 1.3-1 c**). This autophagosome fuses with the lysosome, forming a so called autolysosome (**Figure 1.3-1 d**). Lysosomes are formed by the progressive maturation of early endosomes into late endosomes and finally into mature lysosomes (Saftig and Klumperman 2009). During this process, hydrolytic enzymes

are accumulated within the lumen of the endosomes, and the pH is gradually decreased from approximately pH 6 in early endosomes to approximately pH 4.5 in mature lysosomes (Saftig and Klumperman 2009). The fusion of autophagosomes with lysosomes releases the hydrolytic enzymes into the lumen of the autolysosome, which then start degrading the cytosolic cargo (**Figure 1.3-1 e**) (Metaxakis, Ploumi, and Tavernarakis 2018). The components of this cargo, such as amino acids and lipids, are then recycled into the cytosol to enable the synthesis of new proteins and membranes.

Defects in the autophagy/lysosome system have been linked to NDDs in a number of ways (Wang et al. 2018; Metaxakis, Ploumi, and Tavernarakis 2018). In mice expressing polyQ-expanded huntingtin the transport of autophagosomes has been found to be reduced (Wong and Holzbaur 2014), and huntingtin has been proposed to possess a scaffolding function in selective autophagy (Ochaba et al. 2014) that could be impaired in HD . In PD, the disruption of hydrolase trafficking has been found to reduce lysosomal function (Mazzulli, Zunke, Isacson, et al. 2016) and mitophagy dysfunction has been found to be a cause for this disease (Whitworth and Pallanck 2017). Additionally, lysosomal V-ATPase dysfunction due to the disruption of a PD-associated V-ATPase subunit gene generates autophagy defects that lead to neurodegeneration in mice (Dubos et al. 2015). Furthermore, in AD the function of lysosomes is impaired (Lee et al. 2010) and autophagic vacuoles have been found to cause neuritic swellings (Nixon 2017; Nixon et al. 2005). Genes associated with increased risk for AD, such as PSEN1 and PSEN2, often have functions involved in the endolysosomal system (Nixon 2017). Finally, a number of genetic mutations associated with NDDs have been found to lead to an impaired lysosomal degradation (Menzies, Fleming, and Rubinsztein 2015) and impaired autophagy has been found to cause neurodegeneration (Komatsu et al. 2006). In addition to lysosomal impairment in NDDs, lysosomes are also dysfunctional in a different disease family called lysosomal storage diseases, many of which show neurological symptoms as well (Ferreira and Gahl 2016).

1.4. Artificial β-sheet proteins / aggregates

One main difficulty in the research of NDDs is their overwhelming complexity. As previously mentioned, protein aggregates in NDDs may exert toxicity via gain and loss of function toxicity. However, the function of many disease proteins is not well understood. In addition, toxic gain of function effects may be very complex themselves, and although common features have been identified in many NDDs, many effects vary (Winklhofer, Tatzelt, and Haass 2008).

In order to reduce this complexity, the goal of this thesis was to study the toxic gain-of-function effects of protein aggregates in isolation from any other factors. To that end, artificial aggregating β-sheet proteins (β-proteins) were employed in this study. β-proteins were designed *de novo* from a combinatorial library specifically to create β-sheet fibrils and form amyloid aggregates (West et al. 1999). This was accomplished by selecting amino acid (AA) sequences in which polar and nonpolar residues alternate. This promotes β-sheet folding and aggregation, as the nonpolar residues are buried within the β-sheet structure (Xiong et al. 1995). β-proteins were designed to contain a total of 63 AA,

coding for six β-strands of seven AA connected by five turns of four AA (West et al. 1999). This β-strand length was selected to mimic that of natural amyloid fibrils, while the turn length was selected to ensure the formation of antiparallel strands and to deter the formation of non-β-sheet structures. The mass of a monomeric β-protein was estimated at 6.9 kDa. Multiple different sequences were created by varying the amino acid sequence, creating proteins with differing hydrophobicity and β-sheet propensity.

In a later work by Olzscha and colleagues, three of these β-proteins (β4, β17 and β23) were utilized to study the effects of β-protein aggregation in mammalian cells (Olzscha et al. 2011). It was demonstrated that β-proteins exert toxicity when expressed in HEK293 cells, with β23 showing the highest toxicity after three days of expression. Of the three, β23 shows the highest hydrophobicity and β-sheet propensity. It was shown that β-proteins form amyloid-like aggregates within cells and interact with a number of different proteins. These interactors possess a variety of functions and are natively located in multiple organelles, but share structural and physicochemical properties. They are characterized by a high molecular weight, low hydrophobicity, a high amount of intrinsically unstructured regions and a tendency towards β-sheet folds. In addition, β-protein interacting proteins were found to often be critical, highly connected “hub” proteins with essential functions in their native interactor network.

Study of cells affected by β-protein aggregation as a model for aggregation in NDD has multiple advantages. The greatest advantage is, as β-proteins do not have a native function within the cell, no loss of function toxicity is observed. Therefore, the observed toxicity can be exclusively attributed to gain-of-function effects, which might be applicable to multiple NDDs. Furthermore, as different β-proteins with differing sequences, hydrophobicity, and β-sheet propensity can be studied, the effects of these parameters on the toxicity of protein aggregates can be further resolved. Finally, the effects of interaction and sequestration of cellular proteins within β-protein aggregates on the cell can also be investigated.

However, the study of β-protein aggregates in transfected cells demonstrated how heterogeneous β-sheet aggregation and toxicity effects are as well, especially concerning the time of aggregation onset. Therefore, in another project, protein aggregates of a different type of artificial protein were studied. This protein, derived from the human FK506 binding protein 12 protein, was termed AgDD (Miyazaki et al. 2016). AgDD-GFP was stably expressed in HEK293 cells and, when stabilized by a ligand, is distributed homogeneously within the cells (Miyazaki et al. 2016). By removing the ligand, AgDD immediately starts to form aggregates (Miyazaki et al. 2016), which allows the study of protein aggregation in a time-resolved manner (see section 3.2).

1.5. Microscopy

Ever since Robert Hooke's discovery of the "little boxes" he called cells (Hooke 1665), microscopy has been one of the driving methods in biology. The human eye can only resolve structures if they are apart from each other farther than approximately 75 µm (Egerton 2016). To observe and distinguish smaller features, microscopy is necessary. Light microscopes (LM) are capable of resolving the next three orders of magnitude. However, classical light microscopy is limited in resolution by the visible wavelength (Egerton 2016). Electron microscopes (EM) allow to observe even smaller structures within their cellular context. There are of course also other modes of microscopy, such as atomic force microscopy, but here we will focus on the two main methods used in this thesis, LM and EM.

1.5.1. Microscopy criteria

1.5.1.1. Resolution

As previously mentioned, the principle of why microscopy is employed is to increase an observer's power to resolve structures too small to be distinguished by the human eye. Resolution can be defined as the minimal distance between two features at which they may still be observed as separate (Egerton 2016). In microscopy, resolution may be defined according to the Rayleigh criterion, stating that two points are resolved as separate if the maximum of the Airy disk of one point coincides with the first minimum of the Airy disk of the other point. Practically, the resolution δ depends on the wavelength of the incident beam λ and the angular aperture α of the objective:

$$\delta = \frac{0.6\lambda}{\alpha}$$

1.5.1.2. Contrast

Alongside resolution, contrast is an equally important criterion in microscopy, as to be able to distinguish two points they must also provide contrast. Contrast is defined by the difference in signal intensity that two points provide (Williams and Carter 2009). In LM and in EM contrast is commonly generated by two mechanisms: amplitude contrast and phase contrast. By altering the intensity of the incident beam, the specimen produces amplitude contrast. On the other hand, by shifting the phase of the incident beam, the specimen produces phase contrast.

1.5.2. Light microscopy

Light microscopy is an excellent method to acquire information in the size range of millimeters to micrometers. With LM, it is possible to study live specimens, often in their native environment, in a technically relatively straightforward way, without severely damaging the specimen. However, the simplest form of LM in brightfield mode is not very effective for biological samples, as they often absorb only very little light and therefore produce very little amplitude contrast. On the other hand, due to variations of the refractive index within the sample, for instance due to density differences, biological specimens alter the phase of the light beam. Therefore, one method to achieve high-contrast images is phase contrast microscopy, where variations in phase contrast are translated to amplitude contrast. In short, this is achieved by separating the unchanged incident light wave-front from the specimen-diffracted light at the back focal plane (Sawyer, Grubb, and Meyers 2008). The incident wave is reduced in intensity by a filter and shifted in phase by 90° by a phase ring. The diffracted wave is shifted in phase by the specimen. Both waves constructively interfere on the image plane, resulting in an intensity difference to the background, therefore creating contrast.

A different form of light microscopy that produces amplitude contrast is fluorescence LM (FLM). In FLM, the specimen is not imaged as a whole, but only specific structures previously tagged by a fluorescent marker are imaged. During fluorescence, a photon of a specific wavelength is absorbed by a fluorophore. A new photon with a specific, but longer wavelength is emitted shortly after (Stokes shift). This photon is then detected, producing an image of the structure that is fluorescing.

The main limitation of light microscopy is its resolution. The limit in resolution of a standard light microscope is half of the wavelength that is applied for imaging. As the shortest wavelength of visible light is approximately 400 nm, this limits the attainable lateral resolution through classical LM methods to approximately 200 nm and its axial resolution to approximately 500 nm. However, this resolution may only be achieved under optimal imaging conditions, i.e. by using a suitable, well aligned microscope coupled with a high magnification oil-immersion objective that possesses a high numerical aperture. In modern super-resolution fluorescence light microscopy higher resolutions of up to ~20 nm can be achieved (Gottfert et al. 2013). In this type of LM, different physical effects or stochastic procedures are utilized to circumvent the resolution limit of classical LM. These methods have their own unique caveats, one of which is that the specimen can never be imaged as whole. Also, as these are FLM techniques, only previously marked structures may be imaged.

1.5.3. Electron microscopy

Electron microscopy is superior to LM in two major regards. First, the limit of the resolution that may be achieved due to the applied wavelength is far greater than biologically relevant sizes. Second, unlike in FLM, structures within cells can be imaged within the context of the rest of the cell. However, the

property that gives electron microscopy its resolution power at the same time makes it very impractical and incompatible with the study of living things. Electrons will interact with matter that is in the beam's path with a high probability. Therefore, a high vacuum is needed within the microscope to ensure that the electron beam will interact only with the specimen and the camera. However, organisms are not capable of living in a vacuum, which makes EM very impractical for the study of live samples. In addition, the electrons interacting with the specimen introduce large amounts of energy, thereby destroying biomolecules and hindering the analysis of live cells.

1.5.3.1. Transmission & scanning electron microscopy

Electron microscopes can be split into two general categories, depending on how information is gathered from the specimen: Transmission electron microscopes (TEM) and scanning electron microscopes (SEM).

TEMs work similarly to conventional light microscopes in that a beam is sent through the specimen, acquiring information in the form of a projection image of the whole volume of the specimen. Modern transmission electron microscopes are comprised of the following basic common components (**Figure 1.5-1**) (Frank 2006b). The electron beam is generated by a field emission gun (FEG), which consists of a filament acting as a cathode, an extraction anode, which serves to extract electrons from the cathode, and an acceleration anode, which accelerates the electrons to high keV (**Figure 1.5-1 d-1**). The beam is then shaped by the condenser lens into a coherent form and size (**Figure 1.5-1 d-2**), and passes the condenser aperture, which blocks part of the beam, making it more parallel. Next, the beam goes through the specimen, which is held in place by a computerized goniometer stage capable of tilting the sample (**Figure 1.5-1 d-3**). After passing the specimen, the objective lens forms and magnifies the first image (**Figure 1.5-1 d-4**), and strongly scattered electrons are blocked by the objective aperture located in the back focal plane (**Figure 1.5-1 d-5**). The beam then passes intermediate and projector lenses (**Figure 1.5-1 d-6**), which magnify the image further and project it onto a fluorescent viewing screen (**Figure 1.5-1 d-7**). Alternatively, the screen can be retracted and the beam is sent through an optional energy filter and is detected by a digital camera.

Until recently, digital cameras capable of detecting electrons were based on charge coupled device (CCD) technology (Booth and Mooney 2013). In these cameras electrons are converted into photons by a scintillator, and the photons are subsequently detected and converted into an electronic signal by a CCD chip. These multiple conversion events introduce noise, making CCD cameras relatively ineffective. In contrast, modern direct electron detectors are based on CMOS technology. Here, the camera chip can directly translate the signal of an incoming electron into an electronic signal, therefore suppressing noise and supplying a significantly increased detection efficiency (Booth and Mooney 2013). In addition, these direct electron detector cameras have noticeably decreased readout times, allowing the recording of multi-frame movies per image. These frames can be subsequently aligned

into a final image, correcting for image-blur introduced by specimen movement and substantially increasing resolution (Ruskin, Yu, and Grigorieff 2013).

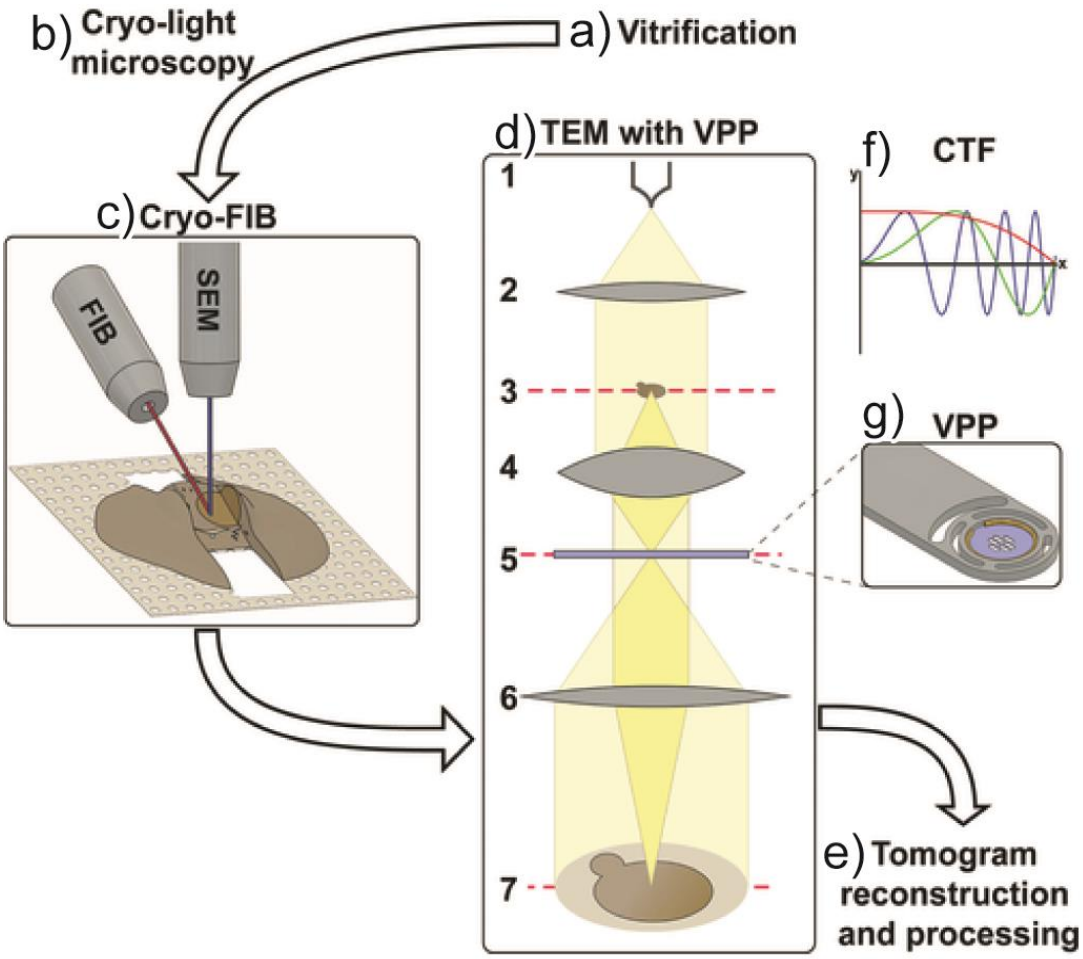

Figure 1.5-1: Scheme of a cryo-TEM equipped for VPP imaging and the corresponding workflow for *in-situ* cryo-ET on cryo-FIB-milled samples. (a) Cells are vitrified, (b) identified by cryo-light microscopy and (c) thinned by cryo-FIB-milling in a cryo FIB/SEM. (d) Samples are transferred to a cryo-TEM and imaged using VPP cryo-ET. (e) Acquired tilt-series are reconstructed and resulting tomograms are processed further. The path of the electron beam is schematically indicated within the TEM (d) at: (1) the electron gun, (2) the condenser lens, (3) the sample, (4) the objective lens, (5) the back focal plane, (6) the projector lens and (7) the fluorescent screen or camera. (f) CTF plot: Imaging without a phase plate at -2 µm (green line) creates low contrast in the low frequency ranges. By defocusing to -7 µm (blue line), the CTF is compressed, increasing contrast at low frequency but decreasing the resolution at high frequencies. The VPP (g), inserted at the back focal plane (5), induces a phase shift (red line), increasing contrast especially in the low frequency ranges. Modified from (Wagner, Schaffer, and Fernandez-Busnadiego 2017) with permission.

In scanning electron microscopes (SEM), on the other hand, the beam targeted at the specimen does not penetrate the complete volume of the specimen, and information from the surface layer of the sample is detected. Scanning electron microscopes are composed of similar components as TEMs. These are arranged in a way that the column containing the electron gun and lenses is situated at the top of the microscope, the sample is below the column in a larger specimen chamber, and the detector is situated at an angle, off the beam's axis (Egerton 2016). The electron gun creates an electron beam,

which is subsequently focused on the specimen into a single small point by condenser and objective lenses. For this reason, SEM are operated in a scanning mode, scanning over the sample in small increments. In order to scan this beam over the sample, additional scan coils placed between the condenser and objective lenses modulate the path of the electron beam in a lateral fashion. The interaction of the beam with the specimen induces secondary electrons, which are attracted towards an electrode and detected by a scintillator. By scanning the beam over the sample point by point, the information of each point can be used to reconstruct a complete image.

1.5.3.2. Resolution in transmission electron microscopy

In practice, the resolution achievable on biological samples in an EM is not limited by the wavelength of the electron beam. A microscope operating at 300kV produces a beam with a wavelength of ~0.02 Å, far below the size of biologically relevant structures (Förster et al. 2012). However, the achievable resolution in EM is limited by aberrations introduced by the microscope's lenses and the quality of the detectors. Three main types of aberration limit the resolution of a TEM image: astigmatism, spherical aberration and chromatic aberration (Williams and Carter 2009). Astigmatism is caused by a rotationally asymmetrical magnetic fields resulting in asymmetrically distorted images. Spherical aberration arises when a ray going through the edge of a lens is focused more strongly than a ray passing through the center of the lens, resulting in a focus disk, rather than a point. Chromatic aberration leads to a similar effect, but is due to changes in the wavelength of a ray. Lower energy electrons are focused more strongly by a lens, again resulting in a focus disk. Changes in electron wavelength are mainly generated by inelastic scattering events at the specimen, diminishing an electrons energy and therefore increasing its wavelength (Williams and Carter 2009). Using modern methods, structures of biological specimen such as protein complexes have been solved to higher resolutions than 2 Å (Merk et al. 2016), and their small size is the main limitation in further resolving the structure of proteins (Khoshouei et al. 2017).

1.5.3.3. Contrast in transmission electron microscopy

Image contrast in TEM of thin biological samples is generally not achieved by absorption, but by scattering of the electrons by the atoms of the sample (Williams and Carter 2009). There are two types of electron scattering: elastic scattering caused by interactions with an atomic nucleus and inelastic scattering, caused by interactions with the atomic electrons. While elastic scattering transfers almost no energy, inelastic scattering may lead to a noticeable change in energy of the electron. When energy is transferred to the sample during inelastic scattering, secondary electrons and X-rays can be released and electrons may reach excited energy states. As inelastic scattering can occur multiple times within a sample, an electron may exit the sample at a distance to the first point of entry. Therefore, the

detection of inelastically scattered electrons contributes to noise in the image. This noise can be reduced through the application of an energy filter (Egerton 2016). An energy filter is a magnetic prism coupled with a slit that separates the path of electrons depending on their wavelength. As inelastically scattered electrons have a different energy and therefore possess a different wavelength, they can thereby be separated from the elastically and unscattered electrons. The slit of the energy filter can be calibrated in such a way that only electrons with a specific wavelength range can pass, thus reducing the amount of inelastically scattered electrons detected.

As elastic scattering is caused by interaction with the nucleus, it is dependent on the atomic number of the atom and the distance between electron and nucleus (Reimer and Kohl 2008). A large atomic number and small distance between the electron and the nucleus results in a large scattering angle. Electrons scattered at large angles are blocked by the objective aperture. They create amplitude contrast, together with inelastically scattered electrons absorbed by the specimen. Similarly to LM, unstained biological samples imaged via cryo-EM generate only very little amplitude contrast (Toyoshima and Unwin 1988), as atoms in biological samples typically possess a small atomic number.

As previously mentioned, contrast may also be diminished by noise caused by scattering. The probability of an electron being scattered by an atom is determined by the interaction cross section (Williams and Carter 2009). This cross section is dependent on the energy of the incident electron and the atomic number of the atom. The higher the energy of the incident electron and the lower the atomic number, the lower the probability of an electron scattering event. The inverse of the total cross-section of a sample defines the mean free path length of an electron, which is the average distance an electron travels between scattering events in a sample. As the total cross section of a sample is additionally dependent on its thickness and density, the sample must be thin enough in order to avoid multiple scattering events.

In cryo-EM phase contrast is the main effect generating image contrast (Frank 2006b). It is generated by the interference of unscattered and elastically scattered electron waves which have passed through the sample in different areas (Frank 2006b). Elastic scattering events on the specimen induce a phase shift within the electron wave. However, as unstained biological samples possess only low atomic numbers, the resulting phase shift is very small. Therefore, interference with the unscattered wave produces only very little contrast. By defocusing the image, an additional phase shift determined by the magnitude of the defocus can be introduced, increasing the phase contrast (Frank 2006b).

The final contrast generated in an image is described by the contrast transfer function (CTF) (Williams and Carter 2009). The CTF is the Fourier transform of the point spread function, the real space modification of the information of the specimen by the imaging system (Williams and Carter 2009). The CTF modifies the contrast of each spatial frequency in an oscillating fashion, dampening it towards higher frequency (**Figure 1.5-1 f,** CTF plot). It is described by the aperture function, the envelope function and the phase-distortion function (Williams and Carter 2009). The aperture function limits the spatial frequencies dependent on the size of the objective aperture. The dampening is due to the effect of the envelope function, which is caused by partial spatial and temporal incoherence of the electrons. The phase-distortion function is affected by spherical aberration, defocus and astigmatism. As

mentioned before, by defocusing the image, the image contrast can be altered. However, this increases the dampening effect of the envelope function at high frequencies, reducing image resolution (**Figure 1.5-1**) (Frank 2006a).

A different method of increasing phase contrast is the introduction of a phase plate. Similarly to LM, the phase plate in EM introduces an additional phase shift. However, phase plate imaging in EM is technically difficult and was not employed routinely until recently. Phase plates in electron microscopes are inserted into the back focal plane in place of the objective aperture (**Figure 1.2-1 g**). Until recently, the most successful phase plate for EM was the Zernike phase plate, consisting of a thin film of amorphous carbon with a small hole in its center (Danev, Glaeser, and Nagayama 2009). However, the use of the Zernike phase plate has noticeable drawbacks, such as its short life span and difficulty to align. A newer type of phase plate, which was employed in this work, is the Volta phase plate (VPP) (Danev et al. 2014). The VPP consists of a thin film of carbon as well, but in this case the film is continuous. The phase shift is achieved by irradiating this carbon film with the electron beam, producing a charging effect on the film, which leads to a dose-dependent phase shift (**Figure 1.5-1 f**) (Danev et al. 2014). This, however, makes the final phase shift also dependent on charging effects originating from the sample, particularly from non-conductive samples such as lamellae created by FIB-milling. To improve the sample conductivity, an additional layer of conductive material such as platinum can be applied on the sample. Although the platinum can create additional image artifacts, especially in cryo-tomography, these can be computationally alleviated (Fernandez et al. 2016).

1.5.3.4. Electron tomography

As previously mentioned, a TEM is similar to a LM, as the beam travels through the specimen, thereby collecting information that may then be detected by a camera. The resulting image is a projection, a superposition of the information obtained over the whole height of the sample. This creates an anisotropic image, as the planar resolution is high but the z-resolution is the height of the sample. To increase the z-resolution, the sample can be tomographically imaged (Frank 2006a). By acquiring projections of the same sample region at different angles, information that is superimposed within a projection at one angle is distinct at a different angle. Information from the resulting series of projections (tilt series) can then be computationally back projected into a virtual volume resulting in a three dimensional model of the imaged volume (tomogram). If the tilt series were acquired over a range of 180°, the resulting tomogram would be an isotropic representation of the sample. However, the path of the beam through the sample gets larger at high tilts, and the electrons passing through a too thick sample are largely inelastically scattered. In addition, the size of the grid holder limits the maximum tilt-angle due to space limitations within the microscope. Therefore, tilt series in electron tomography are typically acquired over a range of only 120° (**Figure 1.5-2**) (Frank 2006a). The resulting 60° wedge of missing information creates an elongation of the z-information within the tomogram, thereby reducing its resolution along that axis (Frank 2006a).

In addition to the information lost in the missing wedge, information is also lost because the sample is imaged at discrete angles. A projection of the sample corresponds to a central section in the 3D Fourier transform of that sample with a thickness inverse to the samples real-space thickness (Frank 2006a). Therefore, the sample information in Fourier space could be acquired through the acquisition of a tilt series over the whole range of 180° and with small angular increments. However, as decreasing the angular increment results in a higher electron dose applied to the specimen, the amount of total angles that can be acquired is limited. This also limits the sampling rate at high frequencies in Fourier space (Crowther criterion, **Figure 1.5-2 b**), thereby reducing the resolution of the high frequencies in the tomogram (Frank 2006a).

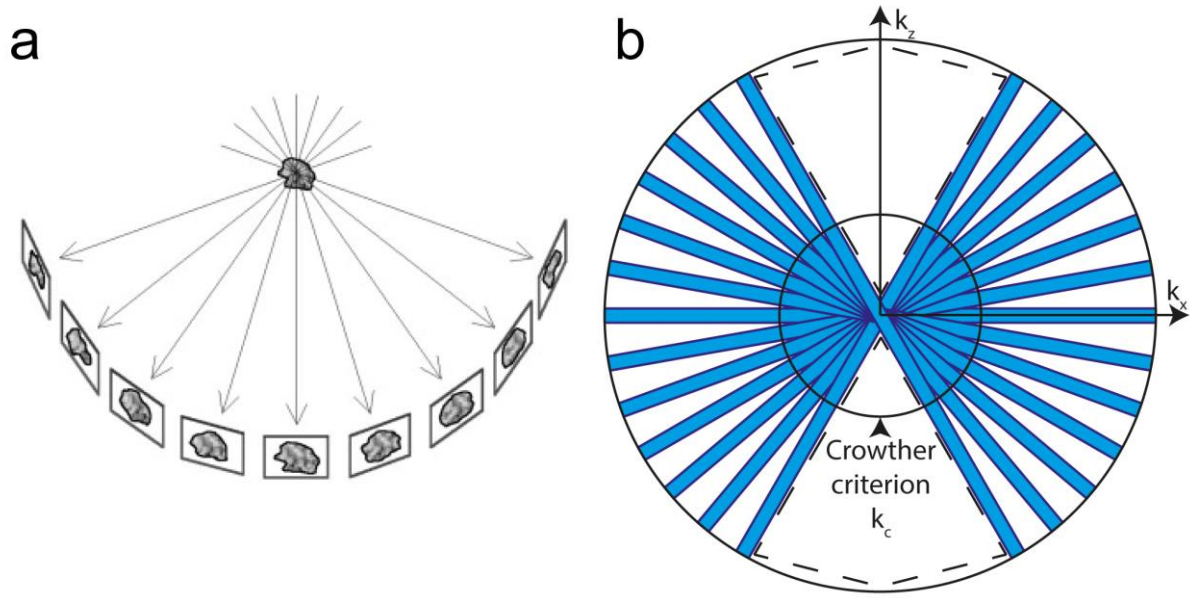

Figure 1.5-2: Scheme of tomography principle and 3D Fourier transform sections sampled by tomography. (a) The sample is tilted over a range of 120° within which projections are acquired at discrete angles (b) Due to limitations at high tilt-angles, a missing wedge of information is formed (areas indicated by dotted lines). Due to the limited amount of total angles imaged, the information is only homogeneously acquired up to the Crowther criterion (spatial frequency k_c). (a) with permission from (Grünewald et al. 2002), (b) inspired by (Lucic, Forster, and Baumeister 2005) Figure 3.

1.5.4. Cryo-Electron microscopy

The most important aspect of any microscopy is sample preparation. If the information within the specimen is destroyed or altered, even the best microscope will not be able to retrieve it. Additionally, and perhaps even more importantly, if a structure within the specimen is altered by the sample preparation in a way the observer is not aware of, such artifacts may be interpreted as true. In the worst case, this would mislead the observer to believe in a false observation.

To overcome the limitations introduced by the vacuum and electron beam, biological specimens have to be fixed prior to imaging. Classically, this meant that the specimen is chemically fixed with a reagent such as formaldehyde or glutaraldehyde. Any residual water is then extracted from the specimen,

which is then embedded in resin. In order to better be able to discern between structures, the sample may also be stained with heavy metals. This sort of preparation has the advantage that the specimen is very robust and can withstand the harsh conditions within the EM. However, the downside to this method is the introduction of artifacts into the specimen, and the highest resolution that can be achieved is at the size level of the fixative used. Molecules and structures smaller than that are not resolvable any more. To overcome this, cryo-electron microscopy (cryo-EM) may be used.

By freezing samples within their native environment, the introduction of fixation artifacts can be largely circumvented. In addition, it is possible to introduce frozen samples into a vacuum without changing their state. However, freezing samples introduces a new level of difficulty and complexity into the imaging process. First, as water solidifies during slow freezing, it rearranges into a crystalline form. These ice crystals drastically alter the structure of the specimen, as solutes within the water are pushed out of the forming crystals, thereby increasing their concentration and destroying their structure in the process. In addition, crystalline ice has a lower density than water and the expansion resulting in this change in density during crystallization deforms cellular structures. In order to circumvent this problem, the water within the specimen needs to be frozen with such a velocity that the water molecules do not have time to rearrange into a crystalline form. Ice formed this way is called vitreous ice. However, vitreous Ice crystalizes at approximately -140 °C (Dubochet et al. 1988). Therefore, vitreous samples need to be preserved at temperatures well below -140 °C at all times.

As previously mentioned, electrons substantially damage biological specimen. This damage is first observed in the fine details of the sample, such as the structure of macromolecules (Baker and Rubinstein 2010). In order to acquire as much information as possible on these fine details, the amount of electrons applied to the specimen (electron dose) in cryo-EM is restricted. However, this leads to a very low signal to noise ratio and severely limits the total amount of information that can be gathered in one image. An additional factor affecting the signal to noise ratio is the thickness of a sample. The thicker a sample is, the higher probability of inelastic scattering events contributing to noise. Therefore, in order to reduce noise and increase the signal to noise ratio, samples in cryo-EM need to be very thin, typically below 300 nm thickness (Arnold et al. 2016).

While chemical fixation does introduce artifacts and limits the achievable resolution, a chemically fixed sample may be stained with the use of heavy metals which bind to specific intracellular molecules such as lipids. In contrast, vitreous samples cannot be stained after vitrification, as the required chemical processes do not occur at cryo-temperatures. This generates the issue that samples may only be observed in their native form and specific structures can only be identified via their morphology. Especially in cellular cryo-tomography, this may prohibit the accurate identification of morphologically similar organelles such as the different components of the endosomal system. In order to circumvent this problem, structures would need to be labeled prior to vitrification. However, these labeling methods need to perturb the cell as little as possible, in order to preserve it in a close-to-native state. To achieve intracellular labeling, a number of methods are being investigated. One example is the introduction of gold labeled antibodies to stain specific structures and proteins in the living cell. This method was investigated within this thesis (see section 3.3).

1.5.4.1. Cryo-fixation

The most common vitrification method used in cryo-EM is plunge-freezing. For this, samples in the form of protein solutions for single particle EM and e.g. cells for tomography, are placed on an EM grid. Typically, a carbon film covers the grid, providing support for the sample, but at the same time being electron transparent, allowing imaging through the film. As imaging this carbon film may introduce artifacts and reduces the electron beam intensity, carbon films commonly possess holes, over which cells may easily span and in which molecules are kept in place within a liquid film by surface tension. After the sample is applied to the grid, it is suspended in a guillotine like device, and excess liquid is removed from the grid by blotting with filter paper. The freezing device is typically composed of a cryogen container at the bottom and a weighted arm at the top into which the specimen can be placed. By releasing a mechanism holding the arm, it is accelerated together with the sample and plunged into a cryogen at high velocities. In order to provide sufficient freezing velocities, this cryogen needs to possess a number of properties. First, it needs to be liquid at cryo-temperatures (at least -140 °C). Second, the cryogen needs to be able to absorb heat in a very short time, in order to provide a fast freezing velocity. Lastly, the cryogen may not vaporize during the vitrification process in such a way that a resulting gaseous layer insulates the sample from further contact with the cryogen (Leidenfrost effect). Commonly, ethane or a mixture of ethane and propane are used a cryogen. It is kept at liquid nitrogen temperatures by a surrounding bath of liquid nitrogen. By plunging the specimen into the cryogen, the specimen is cooled quickly enough to ensure that the water contained within the sample is flash frozen, thereby creating vitreous ice (Frank 2006b).

While plunge freezing is mechanically relatively simple, it has a number of limitations. One limitation is the small sample size that can be frozen quick enough to achieve vitrification. The vitrification velocity achieved via plunge freezing is approximately 10^5 °/s at the surface of a sample and is reduced significantly inside the sample. This limits the thickness at which a sample is successfully vitrified by plunge freezing to a few µm. Therefore the largest specimen that may be frozen via plunge freezing are single cell organisms or a thin layer of mammalian cells. But parts of mammalian cells are often beyond the size limit, and cryo-protectants such as glycerol often need to be applied to ensure vitrification in central areas of the cell. Thicker samples such as mammalian tissue are much too thick for plunge freezing, resulting in a crystalline ice formation within the sample (Frank 2006b). Additionally, multiple samples should be as consistent as possible in terms of ice distribution and thickness. Therefore, the amount of liquid applied on each grid and the amount removed by blotting need to be monitored precisely. However, as specimen sizes for plunge-freezing need to be very small, small environmental variations such as ambient temperature or humidity in between freezing iterations may noticeably alter the amount of liquid present on the grid before blotting. In addition, changes in the tools such as the tweezers or the filter paper can alter the amount of liquid removed during blotting. Blotting may also introduce artifacts, as the surface tension of the receding liquid can compress the sample, and particles within the liquid can accumulate at the air-water interface.

A vitrification method allowing an increased sample volume is high pressure freezing (HPF). With this method, samples with a maximum diameter of a few millimeters and a thickness of several hundred micrometers can be frozen while still producing vitreous ice within the sample (Moor 1987). Samples are typically placed in a sandwich of two carriers, while the space that is not occupied by the sample is filled with a cryoprotectant. These carriers are then placed into a holder within the high pressure freezer and are frozen with liquid nitrogen applied at very high pressures of approximately 2000 bar (Moor 1987). The combined low temperature and high pressure lead to a high freezing velocity of approximately 5000 °/s, allowing the vitrification of relatively thick samples (Moor 1987).

However, the resulting sample then possesses the thickness corresponding to the height of the volume between the two carrier halves, i.e. at least a few hundred microns. Further thinning of such a large volume introduces multiple new issues to overcome, such as finding the exact position of a cell of interest or the technical difficulty in thinning down such large samples. In order to circumvent these issues, a previously published high pressure freezing protocol (Harapin et al. 2015) was tested in this thesis, in which the cryoprotectant needed to fill up the volume that is not occupied by the sample is replaced by 2-Methylpentane (Pentane) (see section 3.4).

1.5.5. Cryo-FIB-milling

As previously mentioned, another main limitation of cryo-ET is the very low sample thickness that is required. Traditionally, this was achieved by cutting the sample into thin slices through the use of a cryo ultra-microtome (Al-Amoudi et al. 2004). However, the mechanical forces introduced during this process deform the sample, thereby introducing artifacts which are difficult to remove post imaging (Frank 2006a). Cryo-focused ion beam (FIB) milling guided by SEM (cryo-FIB/SEM) circumvents the need for mechanical cutting of the sample. In addition to the electron column, a FIB/SEM contains an additional ion column that generates an ion beam. This focused ion beam is used to mill away certain regions of the sample at an angle almost parallel to the EM grid supporting the sample, while the electron beam is used to monitor the milling from an angle almost perpendicular to the grid (**Figure 1.5-1 c**) (Rigort et al. 2012). The focused ion beam is formed by extracting gallium ions from a gallium source, which are then accelerated towards and focused on the sample (Munroe 2009). The beam is scanned in a similar manner to the electron beam. As the interaction of the beam with sample creates secondary electrons and ions, these can be detected in a similar fashion as those generated by the electron beam, resulting in an image. However, as the energy of the ions is much larger than that of electrons due to their large mass, the ion beam removes part of the samples surface material during the imaging process, which can be utilized to mill away specific parts of the specimen.

By milling the material of a cell above and below a region of interest, only a slice termed a lamella is left. The thickness of the lamella can be controlled by the amount of material that is removed, and the sample is typically thinned to ranges of approximately 100 to 200 nm. FIB-milling has the advantage that no mechanical stress is exerted on the sample during the thinning process. However, the

drawback of this technique is that the material that is milled is lost, and each lamella represents only a very small fraction of the total volume of the cell. The thickness of a lamella is therefore always a compromise between good signal to noise ratio in cryo-ET and volume size that can be imaged. In order to be able to image specific cellular structures by cryo-ET, the location of a lamella can be guided by correlating the SEM image of a cell with fluorescence information obtained prior to FIB-milling.

1.5.6. Cryo-LM and correlative cryo-microscopy

In order to combine the strengths of LM and EM, correlative light and electron microscopy is used (de Boer, Hoogenboom, and Giepmans 2015). Here, a sample may be tagged with a fluorescent label, making it possible, for example, to identify specific cells in a cell population or regions within a cell. After light microscopic imaging, the sample is fixed, transferred to the EM, and regions of interest are imaged at high resolutions within their cellular context (Sartori et al. 2007).

To be able to image specific structures in a cell using cryo-ET on a FIB-milled cell, the position of this structure can be identified within the cell using cryo-FLM prior to FIB-milling (**Figure 1.2-1 b**) (Rigort et al. 2010). Cells vitrified on an EM grid are transferred to a cryo-stage specifically designed for light microscopic imaging under cryo-conditions (Arnold et al. 2016). This stage is cooled by nitrogen vapor released from liquid nitrogen and is separated from the atmosphere to prevent the accumulation of atmospheric water on the cold surface of the sample. The EM grid can then be imaged and specific cells or sites within the cells can be identified via fluorescent labels. After cryo-FLM imaging, the grids are transferred to the cryo-FIB/SEM and are imaged via SEM (**Figure 1.5-1 c**) (Rigort et al. 2010). The coordinates of the information obtained via cryo-FLM are then converted to the coordinate system of the SEM by three-point correlation, allowing the precise planar localization of a site of interest. If milling precision in the z-dimension of the sample is required, images acquired with the ion beam, which are acquired at an angle to the sample, can be used to transform z-coordinates previously acquired by cryo-FLM into the coordinate system of the FIB as well (Arnold et al. 2016). After FIB-milling, the sample is finally transferred to the TEM, were the prepared lamellae can be easily localized and imaged (**Figure 1.5-1 d**). To guide sites for tomography on the lamella, the light microscopic information can be superimposed onto low magnification TEM images (Arnold et al. 2016).

1.6. Correlative cryo-ET on cells showing β-protein aggregation

By combining cryo-FLM, cryo-FIB/SEM and VPP cryo-ET in a correlative cryo-FLM/cryo-ET approach on FIB-milled mammalian cells and murine neurons, this thesis aims to elucidate the structural alterations induced by gain of function toxicity generated by β-protein aggregates. To gain additional mechanistic understanding, Identified structural alterations were analyzed further on a functional level.

2. Materials & Methods

2.1. Materials

Table 2.1-1: Materials: Antibodies, buffers and consumables

Type	Designation	Name	Manufacturer	Ref #
Antibody	AP-3 µ3A AB	AP3M1 Polyclonal Antibody	ThermoFisher Scientific	PA5-21162
Antibody	ATG5 AB	Atg5 (D5F5U) Rabbit mAb	Cell Signaling	12994
Antibody	BCN1 AB	Beclin-1 Antibody	Cell Signaling	3738
Antibody	DDK AB	Clone OTI4C5, Anti-DDK (FLAG) monoclonal antibody	OriGene	TA50011-100
Antibody	Green secondary AB	anti-mouse IgG (H+L), F(ab')2 Fragment Alexa Fluor® 488 Conjugate	Life Technologies	A11017
Antibody	HPRT AB	Anti-HPRT antibody	Abcam	ab10479
Antibody	LAMP1 AB	Anti-LAMP1 antibody - Lysosome Marker	Abcam	ab24170
Antibody	LC3 AB	LC3B (D11) XP® Rabbit mAb	Cell Signaling	3868
Antibody	mitochondrial ATPase AB	Anti-ATP5A antibody [15H4C4] - Mitochondrial Marker (FITC)	Abcam	ab119688
Antibody	NPC AB	Mouse monoclonal [Mab414] to Nuclear Pore Complex Proteins	Abcam	ab24609
Antibody	Vimentin AB	Anti-Vimentin antibody [RV202]	Abcam	ab8978
Buffer	Borate Buffer	Borate Buffer	Thermo Scientific™	28341
Consumable	10 cm Dish	Tissue culture dishes	BD Falcon	353003
Consumable	FIB Autogrid	Auto Loader Grid	GEWO Feinmechanik	Q1192
Consumable	EM Grid	R 2/1 Holey Carbon Au 200 mesh	Quantifoil	Q14150
Consumable	Filter paper	Filter papers No. 1 70mm	Whatman	1001-070
Consumable	Glass bottom culture dishes	35 mm Dish | No. 1.5 Coverslip | 7 mm Glass Diameter | Uncoated	MatTek	P35G-1.5-7-C
Consumable	HPF carriers	Specimen Carriers Aluminum Ø 6 mm x 0.5 mm 0.1 / 0.2 mm	TECHNOTRADE	610-100
Consumable	HPF carriers	Specimen Carriers Aluminum Ø 6 mm x 0.5 mm 0.3 mm	TECHNOTRADE	611-100
Consumable	Ibidi imaging dish	µ-Dish 35mm, high, glass bottom	Ibidi	81158

Table 2.1-2: Materials: Chemicals

Type	Designation	Name	Manufacturer	Ref #
Chemical	Bafilomycin	Bafilomycin A1	Sigma-Aldrich	B1793-10UG
Chemical	BSA	Bovine Serum Albumin	ThermoFisher Scientific	BP1600-100
Chemical	BSA gold	Gold Colloid 10 nm	BioCell	EM.GL10
Chemical	DMSO	Dimethyl sulfoxide	Jena BioScience	CPP-A01L
Chemical	EDTA	2,2',2",2'''-(ethane-1,2-diyldinitrilo) tetraacetic acid	Carl Roth GmbH	1410.1
Chemical	Ethane / propane	Ethane 37%, propane 63%	Linde	1965
Chemical	FCCP	Carbonyl cyanide-4-(trifluoromethoxy)phenylhydrazone	Enzo Life Sciences	BML-CM120-0010
Chemical	Formaldehyde	Formaldehyde solution, ACS reagent, 37 W	Sigma-Aldrich	252549-500ML
Chemical	Glycerol	Glycerol molecular biology reagent	Sigma-Aldrich	G5516-100ML
Chemical	heparin	Heparin Natrium	ThermoFisher Scientific	10551944
Chemical	laminin	laminin	Sigma-Aldrich	L2020-1MG
Chemical	pentane	2-Methylpentane	Alfa Aesar	L03001
Chemical	poly-lysine	poly-D-lysine	Sigma-Aldrich	P6407-5MG
Chemical	SDS	sodium dodecyl sulfate	neoLab Migge Laborbedarf	1177KG001
Chemical	TritonX100	Triton™ X-100	Sigma-Aldrich	9002-93-1
Chemical		n-Dodecyl β-D-maltoside	Sigma-Aldrich	D4641

Table 2.1-3: Materials: Culture reagents and dyes

Type	Designation	Name	Manufacturer	Ref #
Culture reagent	B-27	B-27™ Supplement (50X), serum free	Gibco™	17504044
Culture reagent	FBS	Fetal Bovine Serum, Qualified, E.U. Appr.	Life Technologies	10270106
Culture reagent	HBSS	Hanks' balanced salt solution	Life Technologies	14025050
Culture reagent	l-glutamine	L-Glutamine (200 mM)	Life Technologies	25030024
Culture reagent	non-essential AA	MEM NEAA 100x	Life Technologies	11140035
Culture reagent	PBS	Phosphate-buffered saline, pH 7.2	Life Technologies	20012019
Culture reagent	PenStrep	Penicillin-Streptomycin (10,000 U/mL)	Life Technologies	15140122
Culture reagent	rDD	recombinant DD_{FKBP}	Kopito Lab, Stanford University	N/A
Culture reagent	S1	Shield-1	Kopito Lab, Stanford University	N/A
Culture reagent	trypsine	TrypLE Express (1X), Phenol Red	Life Technologies	12605010
Dye	Annexin	Annexin V, Alexa Fluor 488 conjugate	Life Technologies	A13201
Dye	DAPI	4',6-diamidino-2-phenylindole	Sigma-Aldrich	32670-25MG-F
Dye	Dextran Cascade blue	Dextran, Cascade Blue™, 10,000 MW, Anionic, Lysine Fixable	ThermoFisher Scientific	D1976
Dye	Dextran Oregon green	Dextran, Oregon Green™ 488; 10,000 MW, Anionic	ThermoFisher Scientific	D7170
Dye	GFP	GFP Recombinant Aequorea victoria Protein, N-His Tag	ThermoFisher Scientific	13105S07E250
Dye	Lysotracker Green	LysoTracker™ Green DND-26	ThermoFisher Scientific	L7526
Dye	Mitotracker green	MitoTracker™ Green FM	ThermoFisher Scientific	M7514
Dye	Mitoview blue	MitoView™ 405	Biotium	70052
Dye	Z-FR-R110	Rhodamine 110, bis-(N-CBZ-L-phenylalanyl-L-arginine amide), dihydrochloride	Biotium	10209

Table 2.1-4: Materials: Kits, Media and transfection reagents

Type	Designation	Name	Manufacturer	Ref #
Kit	cDNA synthesis kit	High-Capacity cDNA Reverse Transcription Kit	Applied Biosystems	4368814
Kit	Innova gold conjugation kit	InnovaCoat® GOLD – 20OD 10nm Gold Conjugation Kit	Expedeon	228-0005
Kit	PVDF membranes	polyvinylidene fluoride membranes	Life Technologies	LC2002
Kit	qPCR Master Mix	Luna Universal Probe qPCR Master Mix	New England BioLabs	M3004S
Kit	RNA isolation kit	Crystal RNA mini Kit	Biolab	31-010-402
Medium	DMEM	DMEM, High Glucose, no Glutamine	Life Technologies	11960085
Medium	L-15	Leibovitz's L-15	Life Technologies	11415049
Medium	Neurobasal medium	Neurobasal™ Medium	Gibco™	21103049
Medium	Opti-MEM	Opti-MEM™ I Reduced Serum Medium	Life Technologies	31985062
Transfection reagent	dfTAT	dimerized fluorescent TAT	Pellois Lab, Texas A&M University	N/A
Transfection reagent	Fugene	FuGENE 6	Promega	E2693
Transfection reagent	Lipofectamine	Lipofectamine 2000	Life Technologies	11668030

2.1.1. Compound solutions

Table 2.1-5: Compound solutions

Designation	Contents
Cell culture medium	DMEM, 10% FBS, 0.5 mM l-glutamine, 1% non-essential AA, 1% PenStrep
Experiment culture medium	DMEM, 10% FBS, 0.5 mM l-glutamine, 1% non-essential AA
Neurobasal culture medium	Neurobasal medium, 5% FBS, 2% B-27, 0.5 mM l-glutamine
dfTAT inactivation medium	L-15, 1 mg/ml heparin
Fixation buffer	PBS, 4% formaldehyde
Permeabilization buffer	PBS, 0.1% TritonX100
Blocking solution	PBS, 0.1% TritonX100, 5% BSA

2.1.2. Expression Plasmids

1. Expression plasmid for AP-3 µ3A: OriGene Ap3m1 (BC024595) Mouse Tagged ORF Clone, Ref#: MR206629
2. Expression plasmid for ER-GFP-KDEL: Invitrogen pShooter Mammalian Expression Vector (pCMV/myc/ER/GFP), Ref#: V82320
3. Expression plasmid for mCherry and basis for β-protein constructs: Clontech pmCherry-N1 Vector, Ref# 632523
    a. For β23-mCherry: AA sequence of insert between Kpn1 and Age1 of pmCherry-N1 coding for Myc-β23: (Myc, **β-sheet**, *turn*) MCEQKLISEEDLGMQISM**DYQLEIE***GNDN***KVELQLN***DSGG***EVKLQIR***GPGG***RVHFNVH***SSGS***NLEVNFN***NDGG***EVQFHMH**
    b. For β4-mCherry: AA sequence of insert between Kpn1 and Age1 of pmCherry-N1 coding for Myc-β4: (Myc, **β-sheet**, *turn*) MCEQKLISEEDLGMQISM**DYNIQFH***NNGN***EIQFEID***DSGG***DIEIEIR***GPGG***RVHIQLN***DGHG***HI KVDFN***NDGG***ELQIDMH**

2.1.3. Equipment

Table 2.1-6: Technical equipment

Designation	**Name**	**Manufacturer**
Carbon coater	MED 020	BAL-TEC
Cell culture hood	Herasafe HR18	Heraeus
Plasma cleaner	PDC-3XG	Harrick
Light microscope	CorrSight	FEI
LM Objective	63x oil immersion objective (Plan Achromat, NA 1.4)	Carl Zeiss
LM Objective	5x air objective (Plan-ApoChromat, NA 0.16)	Carl Zeiss
LM Objective	40x air objective (EC Plan-Neofluar, NA 0.9)	Carl Zeiss
LM camera	Digital Camera C10600 ORCA-R2	Hamamatsu
LM cryo-module	Cryo-Stage	FEI
Dual-beam FIB/SEM	Quanta 3D FEG	FEI
FIB/SEM cryo-loading system	PP3000T	Quorum
TEM Titan	Titan Krios transmission electron microscope	FEI
TEM Polara	Tecnai F30 Polara	FEI
TEM energy filter	GIF post-column energy filter	Gatan
TEM camera	K2 Summit direct detection camera	Gatan
High pressure freezer	EM ICE	Lecia
Cryo-microtome	EM FC6	Leica
Spectrophotometer	Nanodrop	PeqLab

2.2. Methods

All materials mentioned in this text refer to the designation given in the tables in the Materials section.

2.2.1. Cell culture and transfection:

2.2.1.1. Grid pretreatment

Quantifoil gold 200 mesh R2/1 EM grids were coated with approximately 20 nm of carbon in a carbon coater (Table 2.1-6), made hydrophilic for 45 s in a plasma cleaner, UV sterilized in the cell culture hood for 30 min and prepared for cell or neuronal culture.

For neuronal culture, EM grids were sterilized in ethanol for 10 min, washed several times in double distilled water and transferred to culture dishes containing water. Grids and dishes were coated with poly-lysine (1 mg/ml in borate buffer) for 24 h and washed three times with water. Subsequently, the grids were coated with laminin (5.0 µg/ml in PBS) for 24 h, washed three times with PBS and placed in neurobasal culture medium. During washes and medium exchange steps, grids were transferred to another dish containing appropriate liquid to prevent grids from drying.

2.2.1.2. HeLa culture

HeLa cells were grown in cell culture medium at 37 °C and 5% CO_2. Before experiments the cell culture medium was exchanged for experiment culture medium (Table 2.1-5). For electron microscopy experiments, approximately 25000 cells were seeded in 35 mm dishes containing four pre-treated EM grids 24 h prior to transfection. For light microscopy experiments, approximately 100000 cells were seeded in 35 mm imaging dishes (Ibidi or Mattek) 24 h prior to transfection. For western blot experiments, cells were plated in 6 cm dishes 24 h prior to transfection. When appropriate, HeLa cells were transfected 24 h before experiments. Using Fugene transfection reagent, cells were transfected with the appropriate construct according to the manufacturer's instructions.

2.2.1.3. Neuronal culture

Neuronal culture and transfection was performed by Archana Mishra (MPI of Neurobiology). Mice (C57BL/6 background) were housed in a specific pathogen free facility with 12:12 h light/dark cycle and food/water available ad libitum. All animal experiments were performed in compliance with institutional policies approved by the government of upper Bavaria. For preparation of neurons, one

E14 pregnant mice was sacrificed by cervical dislocation, the uterus was removed from the abdominal cavity and placed into a 10 cm sterile petri dish containing cold HBSS on ice. Each fetus was isolated, heads of embryos were quickly cut, brains were removed from the skull and immersed in ice cold HBSS. Subsequently, cortical hemispheres were dissected and meninges were removed under a stereo-microscope. For each sample, cortical tissue from typically six to seven embryos (from one litter) was cut into smaller pieces, transferred to 15 ml sterile tube and digested with 0.25% trypsin containing 1 mM EDTA for 20 min at 37 °C. The enzymatic digestion was stopped by removing the supernatant and washing the tissue twice with neurobasal culture medium. The tissue was resuspended in 2 ml medium and triturated 10 strokes with the tip of a Pasteur pipette. Single cell suspension was achieved by triturating an additional 10 strokes with a fire-polished pipette. Cells were spun at 180 x g, the supernatant was removed and the cell pellet was resuspended in medium. Neurons were plated on the pre-treated EM grids within 24-well plates (60,000 per well). After 6 days in culture at 37 °C in 5% CO_2, neurons were transfected with the appropriate construct using Lipofectamine transfection reagent according to the manufacturer's protocol.

2.2.1.4. HEK293 AgDD culture

All solutions that came into contact with AgDD-sfGFP-expressing HEK293 cells prior to experiments contained additional 1 µM S1. HEK293 cells were grown in cell culture medium at 37 °C and 5% CO_2. Before experiments the cell culture medium was exchanged for experiment culture medium (Table 2.1-5). For electron microscopy experiments, approximately 25000 cells were seeded in 35 mm dishes containing four pre-treated EM grids 24 h prior to experiments. Prior to plunge freezing, rDD was added to a concentration of 5 µM, titrating intracellular S1 out of the cells. Cells were frozen at the appropriate time point.

2.2.1.5. dfTAT mediated cargo transduction

For dfTAT cellular delivery experiments, HeLa cells were cultured as previously stated. Cells were washed three times with PBS and incubated for 1 h in dfTAT-cargo delivery medium. For LM experiments, dfTAT-cargo delivery medium consisted of L-15 medium, 5 µM dfTAT and 1 mM GFP or 20 µg/ml mitochondrial ATPase antibody (AB), NPC AB or gold-conjugated NPC AB. For EM experiments, dfTAT-cargo delivery medium consisted of L-15 medium, 10 µM dfTAT, 1 mM GFP and 20 µg/ml gold-conjugated NPC AB or 5% 10 nm gold particle solution (Innova gold or BSA gold). Conjugation of 10 nm gold to NPC AB was performed with an Innova gold conjugation kit according to the manufacturer's instructions. Cells were washed three times with dfTAT inactivation medium. Cells were either vitrified by plunge-freezing, imaged via live-cell imaging or fixed with fixation buffer for 10 min for immunostaining.

2.2.2. Sample vitrification

2.2.2.1. Plunge freezing

Cells were vitrified using a home-made manual gravity-driven plunge-freezer. Before plunge-freezing, cells were treated with 10% glycerol in experiment culture medium as a cryoprotectant for 1 – 5 min. In addition, in some cases cells expressing β-proteins or mCherry were stained for dead cells using 3% Annexin 15 minutes prior to vitrification. During plunge-freezing, EM grids were blotted for 8 s with filter paper from the backside and immediately frozen in liquid ethane/propane kept at liquid nitrogen temperature. Grids were transferred to liquid nitrogen and excess ethane/propane was blotted with pre-cooled filter paper. Grids were stored in liquid nitrogen until further use.

2.2.2.2. High-pressure freezing

For HPF a Leica EM ICE high-pressure freezing machine was used. This machine is designed to allow vitrification of samples within large 6 mm aluminum carriers, which are large enough to hold EM grids. The bottom carrier disk had a 100 micrometer high indentation while the lid was without indentation, minimizing the volume needed to be vitrified. Grids were blotted from the back for 6 s to remove any excess medium. Simultaneously, carriers were pre-filled with pentane. Next, the grids were inserted into the carrier, while pentane filling was continued. As pentane rapidly evaporates at room temperature, continuous filling and fast sample handling was important to avoid gas pockets inside the carrier cavity. After inserting the grid, the carrier was immediately closed and the sample was frozen.

2.2.3. Light Microscopy

Samples were imaged using widefield, brightfield and epifluorescence microscopy in a CorrSight microscope using FEI MAPS 2.1 software unless otherwise stated. Low magnification overview images were acquired with a Zeiss 5x air objective. For high magnification images, a Zeiss 63x oil immersion objective was used at non-cryo-conditions and a Zeiss 40x air objective was used at cryo-conditions. Images were acquired with a 1344 x 1024 pixel camera (pixel size 6.4 µm, Hamamatsu Digital Camera C10600 ORCA-R2).

2.2.3.1. Immunofluorescence light microscopy

Medium from imaging dishes containing cells was aspirated and cells were fixed in fixation buffer for 10 min. Cells were washed once with PBS and permeabilized with permeabilization buffer for 5 min. Permeabilization buffer was aspirated and cells were incubated in blocking solution for one hour. Blocking solution was replaced with fresh blocking solution containing primary antibodies diluted to the appropriate concentration (Table 2.2-1) and cells were incubated over night at 4 °C. Primary antibody solution was aspirated and cells were washed three times with PBS for 5 min. Cells were either directly imaged or treated with green secondary antibodies and/or DAPI.

When applicable, cells were incubated with green secondary AB diluted to 1 µg/ml in blocking solution for two to three hours. Secondary antibody solution was aspirated and cells were either incubated with 500 nM DAPI in PBS for 5 min and then washed three times with PBS for 5 min or directly washed.

For immunostaining of cells transduced with antibody via dfTAT, chemically fixed cells were washed once with PBS and permeabilized with permeabilization buffer for 5 min. Permeabilization buffer was aspirated and cells were incubated in blocking solution for one hour. Blocking solution was replaced with fresh blocking solution containing green secondary AB diluted to 1 µg/ml in blocking solution and cells were incubated for three hours. Secondary antibody solution was aspirated and cells were either incubated with 500 nM DAPI in PBS for 5 min and then washed three times with PBS for 5 min or directly washed.

Cells were kept in PBS for imaging. Z-stacks were acquired in 500 nm steps over the whole cell height using FEI MAPS 2.1 software.

Table 2.2-1: Primary antibody dilutions for immunofluorescence

Antibody	**Dilution**
AP-3 µ3A AB	1/50
DDK AB	1/1000
mitochondrial ATPase AB	1/100
NPC AB	1/5000
Vimentin AB	1/1000

2.2.3.2. Live cell light microscopy

Cells were kept on a 37 °C heated stage in a homemade climate chamber infused with humidified air and 5% CO_2 gas. Z-stacks were acquired in 500 nm steps over the whole cell height using FEI MAPS 2.1 software.

For the analysis of lysosome size and number, neuronal cultures expressing β23-mCherry, β4-mCherry or mCherry were dyed with 75nM LysoTracker Green for 30 min according to manufacturer's

instructions. Cells showing mCherry signal were imaged. The mCherry signal was used to assess the cell perimeter and only lysosomes within were measured. The mCherry signal of each cell was isolated by automatic thresholding using a homemade script written for Fiji software (Schindelin et al. 2012). The size of each lysosome was manually measured in its in-focus plane using Fiji software.

For lysosomal pH measurements, neuronal cultures expressing β23-mCherry, β4-mCherry or mCherry were incubated with 0.5 mg/ml dextran Oregon green and 0.5 mg/ml dextran Cascade blue for 1 h a few hours after transfection. Medium was exchanged, cells were incubated for 24 h and cells showing mCherry signal were imaged. The mCherry signal was used to assess the cell perimeter and only lysosomes within were measured. The mCherry signal of each cell was isolated by automatic thresholding using a homemade script written for Fiji software. The fluorescence intensity of each manually picked lysosome was measured in its in-focus plane in both green and blue channels using Fiji software. Intensity ratios indicating relative pH were calculated per lysosome.

For mitochondrial membrane potential measurements, neuronal cultures expressing β23-mCherry, β4-mCherry or mCherry were dyed with 200 nM Mitotracker Green and 50 nM Mitoview Blue for 15 min. Medium was replaced after incubation and cells were imaged. To acquire base intensity values, the membrane potential was depleted by adding FCCP to a final concentration of 1 µM and cells were immediately imaged again. Cells showing mCherry signal were imaged. The mCherry signal was used to assess the cell perimeter and only mitochondria within were measured. The mCherry signal of each cell was isolated followed by the isolation of each mitochondria by automatic thresholding using a homemade script written for Fiji software. Mitochondria were marked by their signal in the membrane potential independent green channel in each slice over the whole cell using Fiji software. Signal intensities were measured in both green and blue channels and signals of each cell were averaged. Signal intensities for each condition were averaged per channel. Average values were used to calculate the membrane potential ratios per condition.

The lysosomal cathepsin activity experiment was performed by Archana Mishra (MPI for Neurobiology). Cathepsin activity was measured in situ using the cysteine protease substrate Z-FR-R110. This non-fluorescent substrate enters the lysosomal compartment, gets cleaved by active cathepsin B & L and the cleavage products emit a green fluorescent signal. Cortical neurons were incubated with 10 µM Z-FR-R110 for 90 min at 37 °C and 5% CO_2. Neurons were rinsed in PBS and imaged in neurobasal medium using a Zeiss confocal laser scanning microscope (excitation at 488 nm, 63X objective). Emission (522 nm) was recorded and the mean pixel intensity of neuronal cell body was calculated using Fiji software.

To assess the AgDD aggregation over time, HEK293 cells expressing AgDD-sfGFP were imaged prior to the addition of rDD. rDD was added to the cells to a concentration of 5 µM, titrating intracellular S1 out of the cells. Cells were imaged again at 20 min and 6 h after rDD application.

2.2.3.3. Cryo-light microscopy

Frozen grids were fixed into FIB Autogrid frames to increase mechanical stability. Samples were transferred to an FEI CorrSight shuttle and mounted on the CorrSight cryo-stage maintained at liquid nitrogen temperature for cryo-light microscopy. Grids were imaged in widefield mode at low magnifications and in spinning-disk confocal mode at high magnifications for identification of cells and/or aggregates. Image acquisition and further SEM correlation was performed by three-point correlation of the coordinate systems using FEI MAPS 2.1 software.

Grids designated for correlation of cryo-FLM data of lamellae with cryo-TEM lamella overviews were mounted on the CorrSight LM as stated above. Previously FIB-milled cells were imaged in spinning-disk confocal mode in z-stacks with 200 nm spacing over the whole cell height. Z-stack slice intensities were summed over the height of the lamella and correlated to cryo-TEM lamella overviews by three point correlation.

2.2.4. Cryo FIB SEM

Grids imaged by light microscopy were mounted on a transfer shuttle designed for a cryo-loading system (Rigort et al. 2010) and loaded into a dual-beam FIB/SEM. Grids were sputtered with platinum (10 mA, 30 s) in the Quorum loading system to reduce charging effects during electron imaging. Grids were loaded and coated with organometallic platinum as a protective layer for ion beam milling. Grids were imaged with the scanning electron beam operated at 5 kV / 12 pA and regions of interest (ROI) were identified via cryo-LM/SEM 3-point correlation using MAPS 2.1 software. ROI were thinned down at tilt angles of 18° - 20° with the focused ion beam operated at 30 kV. The beam currents where set to 1 nA at approximately 1 µm distance from the ROI, 500 pA at 750 nm, 300 pA at 400 nm, 100 pA at 250 nm, 50 pA at 100 nm and 30 pA at 75 nm for fine polishing. If grids were designated for VPP imaging, grids were sputtered once more with platinum (10 mA, 5 s) after milling to increase conductivity of the lamellae.

2.2.5. Cryo ET

Cryo-TEM was performed either with a Titan Krios cryo-TEM operated at 300 kV, equipped with a FEG, post-column energy filter and Volta phase plate (Danev et al. 2014) or a Polara F30 cryo-TEM operated at 300 kV, equipped with a FEG and post-column energy filter. Tomograms were acquired on a K2 Summit direct electron detector in dose fractionation mode (0.08 frames per second) using SerialEM (Mastronarde 2005). Lamella overview images were acquired at 3600x magnification (pixel size: 38.93

Å) on Titan Krios or at 3000x magnification (pixel size: 39.83 Å) on Polara and stitched using the automatic photo merge in Adobe Photoshop. For cryo-FLM – cryo-TEM correlation, stitched lamella TEM overview images were imported into MAPS and aligned with previously acquired post-FIB cryo-FLM data. Tomograms were taken at -0.5 µm defocus for VPP imaging at 33000x magnification (pixel size: 4.21 Å) on Titan Krios and at -6 µm or -9 µm defocus at 22500x magnification (pixel size: 5.22 Å) on Polara. The tomograms were acquired at an angular increment of 2° and typically ranged from -50° to 60°. The total dose was restricted to approximately 120 electrons / Å² per tomogram.

2.2.6. Tomogram reconstruction and data processing

Frames were aligned and combined using an in-house software based on previous work (Li et al. 2013). Tilt-series were aligned using patch tracking from the IMOD software package (Kremer, Mastronarde, and McIntosh 1996) and reconstructed with weighted back projection. The platinum layer for VPP imaging and large pieces of surface ice contamination were computationally removed to increase signal to noise ratio (Fernandez et al. 2016). The resulting tilt-series were realigned and reconstructed again. Tomograms were binned four times to a pixel size of 16.84 Å (Titan Krios) or 20.88 Å (Polara) to increase contrast.

Manual segmentation of tomograms was performed using Amira. Membranes and microtubules were automatically segmented using TomoSegMemTV (Martinez-Sanchez et al. 2014) and corrected using Amira. β-protein fibrils were traced on de-noised tomograms (non-local means filter) by removing membranes and macromolecules followed by density thresholding and subsequent skeletonization. Coordinates of macromolecules identified via template matching were imported into Amira and masked with the appropriate filtered molecular structure.

2.2.7. Template matching

For the identification of macromolecule positions, template matching was applied using the pyTOM toolbox in MATLAB (Mathworks) as previously reported (Hrabe et al. 2012). Template matching was performed by Qiang Guo (MPI for Biochemistry). A human 80S ribosome structure (PDB: 4UG0) (Khatter et al. 2015) was filtered to 40 Å and used as a template for ribosome template matching. For TRiC template matching, a structure from *Saccharomyces cerevisiae* (PDB: 4V94) (Leitner et al. 2012) was filtered to 40 Å and used as a template. For 26s proteasome template matching, a structure from *Rattus norvegicus* (PDB: 6EPF) (Guo, Lehmer, et al. 2018) was filtered to 40 Å and used as a template

2.2.8. Western Blotting

Western blot experiments were performed in the lab of Nuno Raimundo (University of Göttingen). Whole-cell extracts of cultured human cells were prepared in 1.5% n-Dodecyl β-D-maltoside in PBS as described (Raimundo et al. 2009). Gels were loaded with 50 µg of total protein per well, proteins were separated in 15% SDS-PAGE gels and transferred to PVDF membranes. The following antibodies were used for immunoblotting: ATG5 AB, BCN1 AB, HPRT AB, LAMP1 AB, LC3 AB (Table 2.1-1). Band density quantification was determined using ImageJ and normalized against loading controls.

2.2.9. Quantitative RT-PCR

qPCR experiments were performed in the lab of Nuno Raimundo (University of Göttingen). RNA isolation and purification was performed using the RNA isolation kit according to the manufacturer's instructions. RNA quantification and quality control were done using a Nanodrop. cDNA was synthesized using the cDNA synthesis kit according to the manufacturer's instructions. cDNA was diluted 1:50, each 8 µl reaction contained 4 µl diluted cDNA, 0.2 µl dilutions of each primer (25 µM stock), and 3.6 µl qPCR Master Mix. The primers were described in (Fernandez-Mosquera et al. 2017).

2.2.10. Statistical analysis

Statistical analyses was performed using Origin Pro 2015G. For analysis of lysosomal size and number, a two tailed Mann-Whitney test was used. For analysis of lysosomal pH, a one tailed directional Mann-Whitney test was used. For analysis of western blot and qPCR data, a two-tailed t-test was used. Statistical significance is shown as $*p < 0.05$, $**p < 0.01$, $***p < 0.001$.

3. Results

3.1. In situ structure of toxic β-protein aggregates

In order to study the structural effects of β-protein aggregation in cells *in situ* in a near native state, we applied cryo-ET on FIB-milled lamellae of β-protein expressing cells. To gain a first insight on the structure of β-protein aggregates, HeLa cells were chosen as a model cell line for the expression of β-proteins. HeLa cells are easily cultivated and transfected, making them ideal to gather preliminary information on β-protein aggregates. Cells were transfected with β23, as it was previously found to be the most toxic β-protein in HEK293 cells (Olzscha et al. 2011), However, since NDDs are neuronal diseases, β-protein-expressing neurons were subsequently studied. Additionally, it was determined that β4 aggregates are more toxic in neurons than β23 aggregates. Therefore, data on β-protein aggregates was also acquired on β4-expressing neurons. Neuronal culture and transfection was performed by Archana Mishra (MPI for Neurobiology).

3.1.1. β-protein aggregate structure

To gain a first insight on the morphology of β-protein aggregates, β-protein expressing cells were first imaged by FLM. β-protein aggregates in HeLa cells and neurons were detected as early as 4.5 h after transfection. Both β4 and β23 aggregates formed large (up to 20 µm along the longest axis), irregularly-shaped aggregates. However, as β23 is more aggregation prone, it formed spatially defined aggregates more frequently, as observed by light microscopy (**Figure 3.1-1 a-c**). β23 aggregates in HeLa cells tended to localize in a central region, while aggregates in neurons were more dispersed within the cells (**Figure 3.1-1 a-c**).

Cells designated for cryo-ET were first imaged by cryo-FLM in order to guide further cryo-FIB/SEM lamella preparation. Cells were subsequently imaged by cryo-ET. Initial tomography showed that β-protein aggregates provided an extremely low contrast, complicating their identification (data not shown). For this reason, VPP imaging at a defocus of -0.5 µm was utilized throughout these studies. VPP imaging induces a phase shift in the CTF of the generated signal, especially increasing low frequency information and therefore allowing a better visualization of both fibrils and aggregates. VPP cryo-ET revealed that β4 aggregates consist of a sponge-like network of thin fibrils and are closely associated with ER and endosomal membranes, mitochondria and ribosomes (**Figure 3.1-1 d, e**).

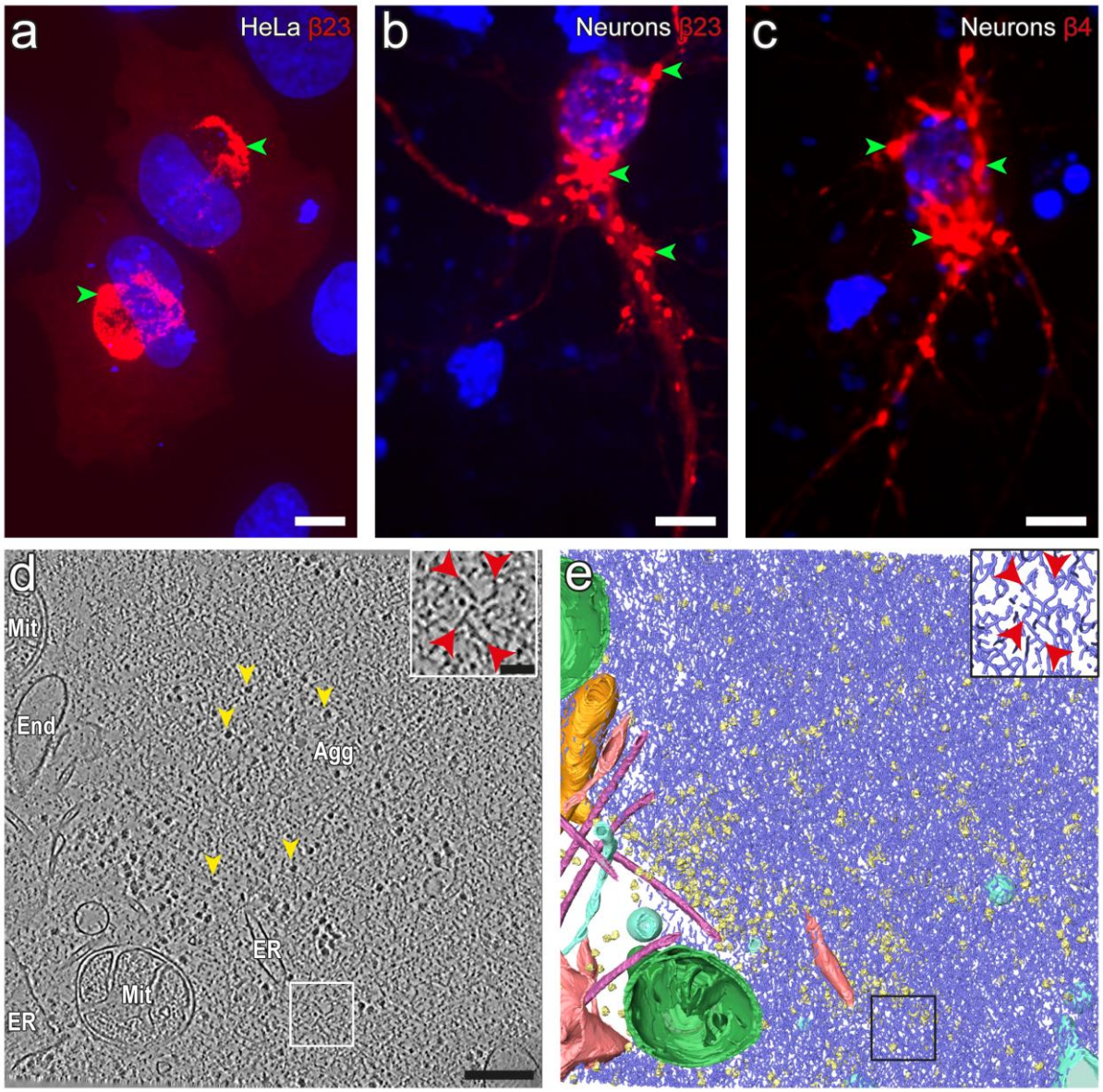

Figure 3.1-1: β-proteins form large and irregularly shaped aggregates. Aggregates are formed by a sponge-like fibril network. FLM images of Hela cells (a) and neurons (b, c) showing β23 (a, b) and β4 (c) aggregates (red) (green arrowheads). Cell nuclei were counterstained with DAPI (blue) (a, b). β23 aggregates (a, b) are often more spatially defined than β4 aggregates (c). Representative tomographic slice of neuron expressing β4 (d) and corresponding 3D rendering of respective tomogram (e). β4 aggregates contain and are surrounded by mitochondria, ER and endosomal membranes and ribosomes (yellow arrowheads). Insets: magnification of boxed region. Fibrils (red arrowheads) form a sponge-like network. Agg, β4 aggregate; End, endosome; ER, endoplasmic reticulum; Mit, mitochondrion. Color code in 3D rendering: purple: β4 fibrils, orange: endosome, red: ER, green: mitochondria, yellow: ribosomes, light blue: vesicles, pink: microtubules. Scale bars: (a - c) 10 µm, (d) 200 nm, inset 50 nm.

Both β4 and β23 aggregates in neurons and HeLa showed similar associations with ER and endolysosomal membranes, mitochondria and ribosomes (**Figure 3.1-2 a-c**). Aggregates formed by either β4 or β23 in neurons or HeLa consisted of a similar network formed by fibrils 3-5 nm in diameter. In neurons, the mean thickness of β4 and β23 fibrils was, respectively, 4.1 nm ± 1.15 nm (mean ± SD, 30 fibrils from 3 cells), and 3.57 nm ± 1.12 nm (mean ± SD, 30 fibrils from 2 cells). These fibrils created

only a very low contrast in cryo-ET, making them and therefore the aggregate very difficult to see using cryo-ET even by VPP imaging (**Figure 3.1-2 d, e**).

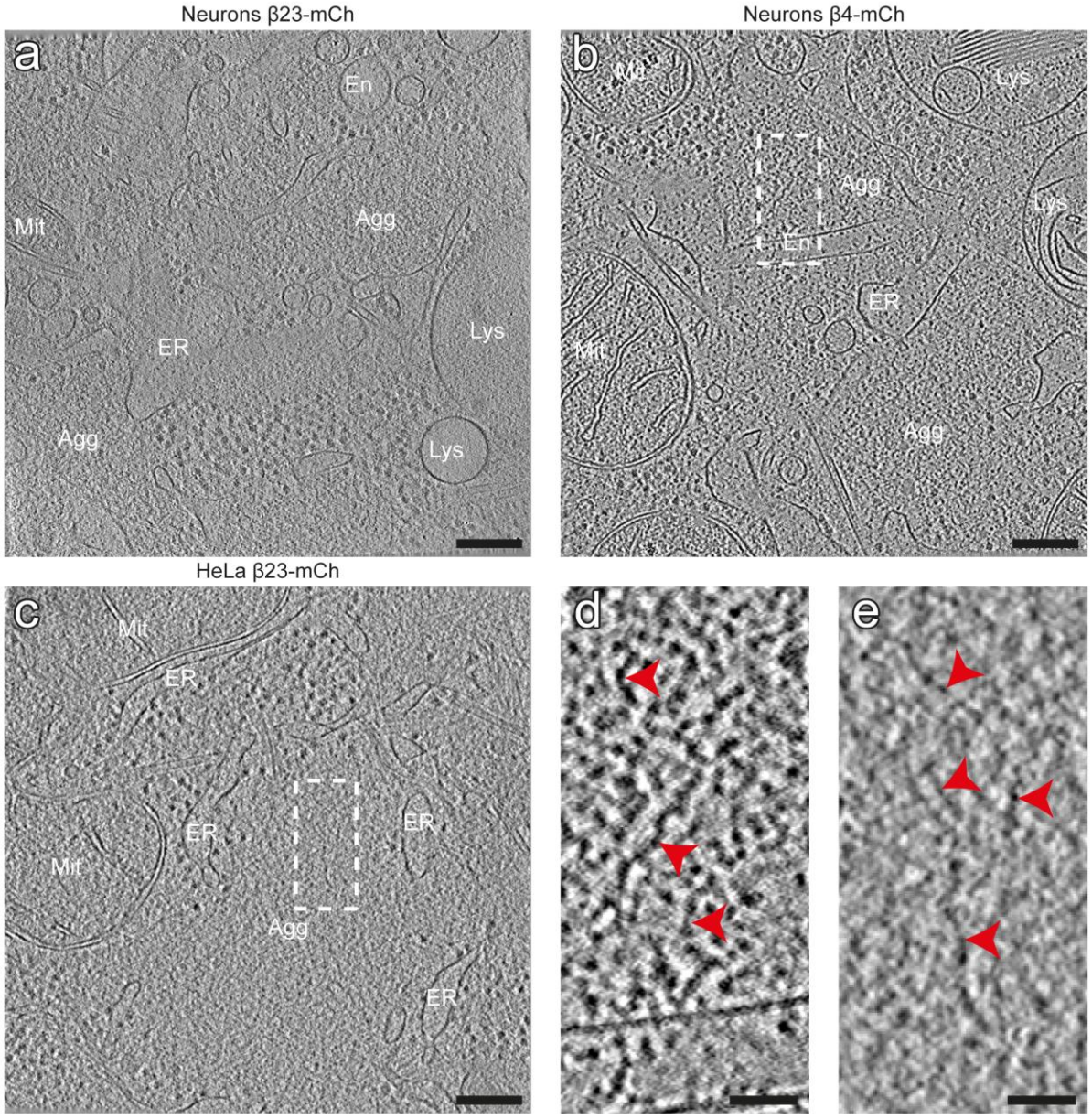

Figure 3.1-2: β23 and β4 aggregates in HeLa cells and neurons are morphologically similar and show similar surrounding organelles and macromolecules. Representative tomographic slices of neuronal cells (a, b) and HeLa (c) showing β23 (a, c) and β4 (b) aggregates. β4 and β23 aggregates in neurons and HeLa are formed by a similar network of thin fibrils. (d, e) Magnifications of areas indicated by dotted lines from (b, c) respectively. β-protein fibrils create only very low contrast in cryo-ET. Fibril morphology was similar for different β-proteins and cell types. Mitochondria, ER-membranes, ribosomes and components of the endo-lysosomal system can be found within and in direct proximity of the aggregates. Agg, β-protein aggregate; En, endosome; ER, endoplasmic reticulum; Lys, lysosome; Mit, mitochondrion. Scale bars: (a – c) 200 nm, (d, e) 50 nm.

Due to the low contrast of the aggregates and the small diameter of the fibrils and their irregular arrangement, reliably identifying the boundaries of the aggregate was not possible (**Figure 3.1-2**). In addition, information on the position of β-protein aggregates acquired by cryo-FLM has a low z-resolution, and the manual correlation of cryo-FLM data onto cryo-SEM images is never perfect. Therefore, it is difficult to correlate the position of an aggregate from cryo-FLM data acquired prior to

FIB–milling with cryo-EM data. To confirm that these structures were indeed β23 aggregates, FIB-milled samples were imaged by cryo-FLM to guide subsequent cryo-ET. The lamellae were imaged using spinning-disk confocal mode in order to achieve an increased z-resolution. By correlating the position of fluorescent puncta with the TEM lamella overview images, subsequent cryo-ET on these positions confirmed the structures as β23 aggregates (**Figure 3.1-3**).

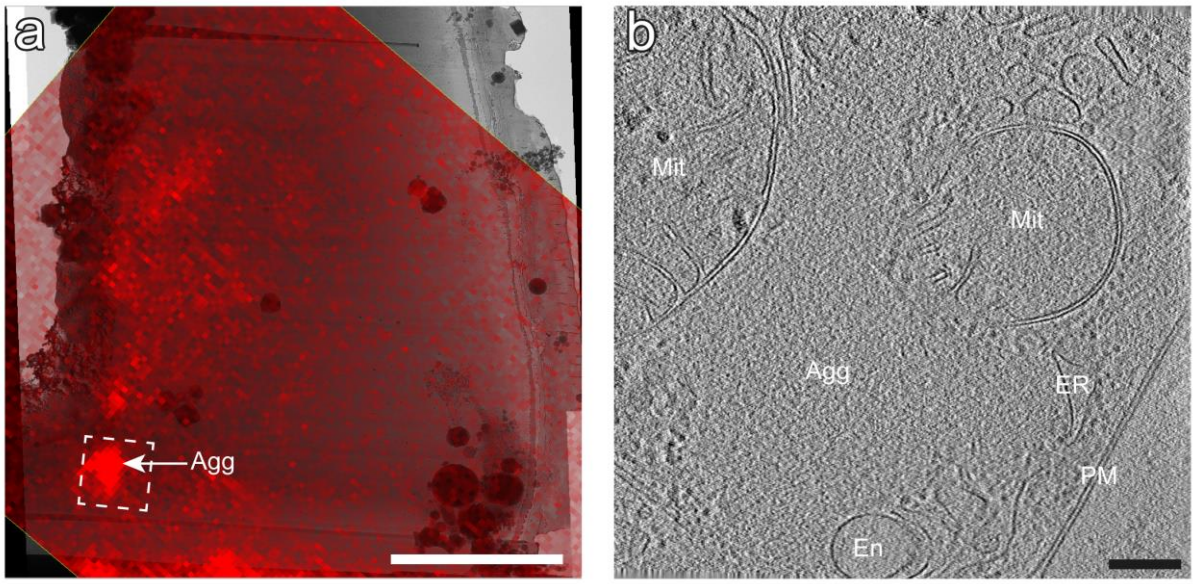

Figure 3.1-3: Cryo-FLM – cryo-TEM correlation indicates aggregates observed by cryo-ET to be fluorescent. (a) A lamella of a HeLa cell showing β23 aggregates (TEM image) superimposed with a summed intensity projection of the β23 fluorescence signal (red). The area indicated by the arrow shows the position of an aggregate as indicated by the increased fluorescence signal. (b) Tomographic slice of the region indicated in (a) showing the aggregate. Agg, β-protein aggregate; En, endosome; ER, endoplasmic reticulum; Mit, mitochondrion; PM, plasma membrane. Scale bars: (a) 5 µm, (b) 200 nm.

3.1.2. Interactions of β-protein aggregates with cellular components

3.1.2.1. Interactions with ER

The overall architecture of both β4 and β23 aggregates was highly similar to each other and when comparing aggregates within neurons and HeLa cells (**Figure 3.1-2**). Both β-protein types showed similar interactions with organelles and macromolecules in both cell types. The most obvious were the close association of ER membranes and mitochondria with the aggregates (**Figure 3.1-2**). By cryo-ET, ER membranes can be identified, amongst other criteria, by the presence of ER-associated ribosomes. ER membranes were situated in direct proximity, often contacted by β-protein fibrils, and were sometimes also found enclosed within the aggregates (**Figure 3.1-2 b**). It was previously reported that fibrils forming polyQ aggregates often contact membranes as well, especially the ER (Bauerlein et al. 2017). While the polyQ fibril contacts often resulted in the deformation of membranes indicated by high curvatures, this was not the case for β-protein fibrils contacting the ER membranes (**Figure 3.1-4 b, c**). The membranes were only infrequently deformed at fibril contact sites (**Figure 3.1-4 a**).

Therefore, unlike polyQ huntingtin fibrils, β-protein fibrils do not appear to deform cellular membranes.

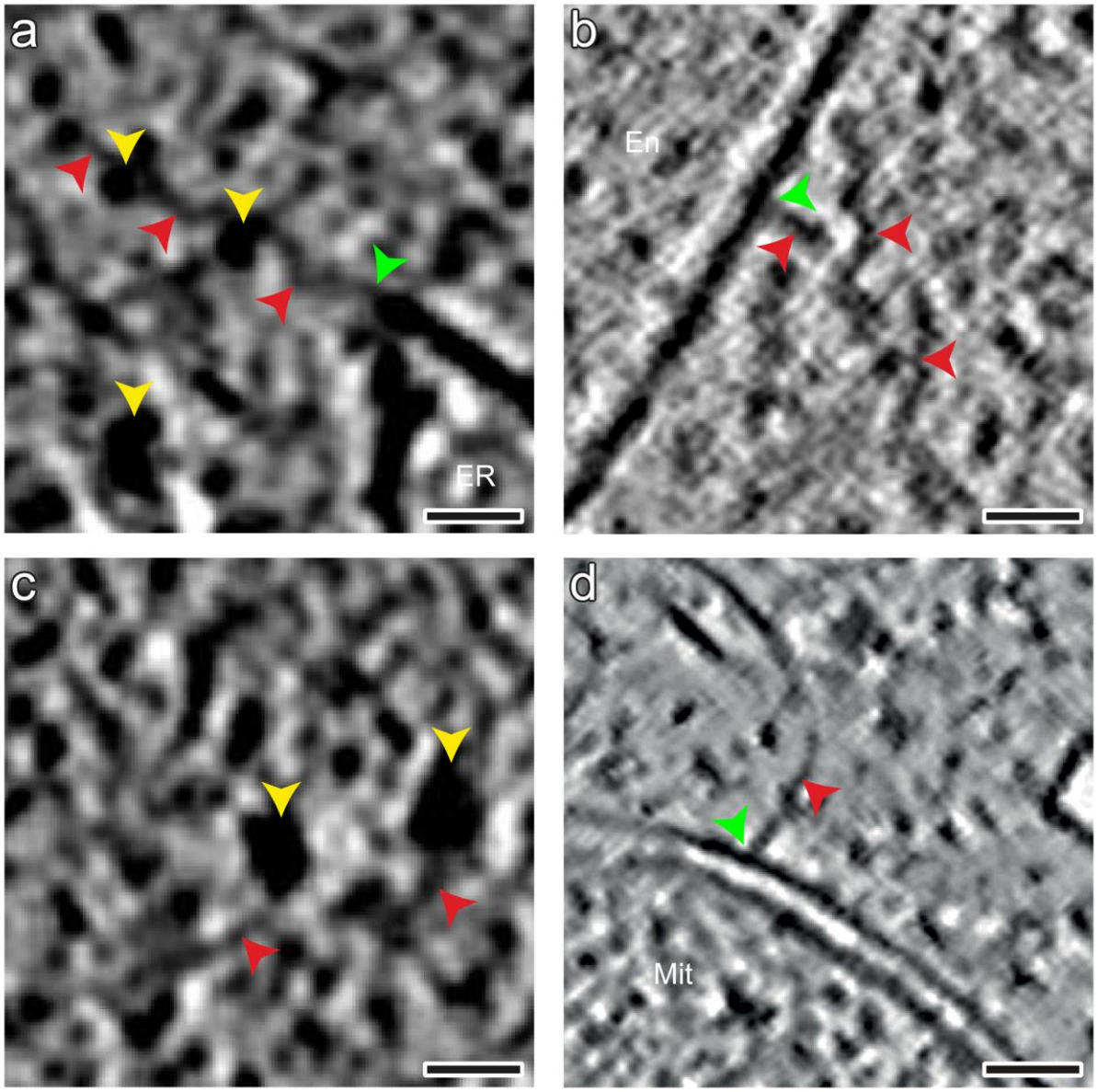

Figure 3.1-4: β-protein fibrils contact membranes and ribosomes. Gallery of β23 (a, c) and β4 (b, d) fibrils (red arrowheads) contacting ER, endosomal and mitochondrial membranes (a, b, d) and ribosomes (yellow arrowheads) (a, c). Fibril-membrane contacts (green arrowheads) typically do not deform the membrane (b, d) and only sporadically can fibrils be found in areas with high membrane curvature (a). En, endosome; ER, endoplasmic reticulum; Mit, mitochondrion. Scale bars: 25 nm.

Since the cryo-ET data indicated that β-protein aggregates were surrounded by ER membranes, we examined possible ER-aggregate interactions by FLM to gain a more general view. FLM analysis of the ER by co-expression of β23 and ER-GFP-KDEL (ER-GFP) in HeLa cells did not indicate an abnormally increased amount of ER in the vicinity of the aggregate, in comparison with other cytosolic areas of the cell (**Figure 3.1-5 a**), in contrast to what was observed for polyQ inclusions. However, β23 aggregates were very often found in areas with high ER concentrations. Additionally, only some of the ER-GFP signal overlapped with the mCherry-positive aggregates, indicating that the bulk of the ER was not

positioned inside the aggregates (**Figure 3.1-5 b, c**), but also verifying the close ER-aggregate association observed via cryo-ET.

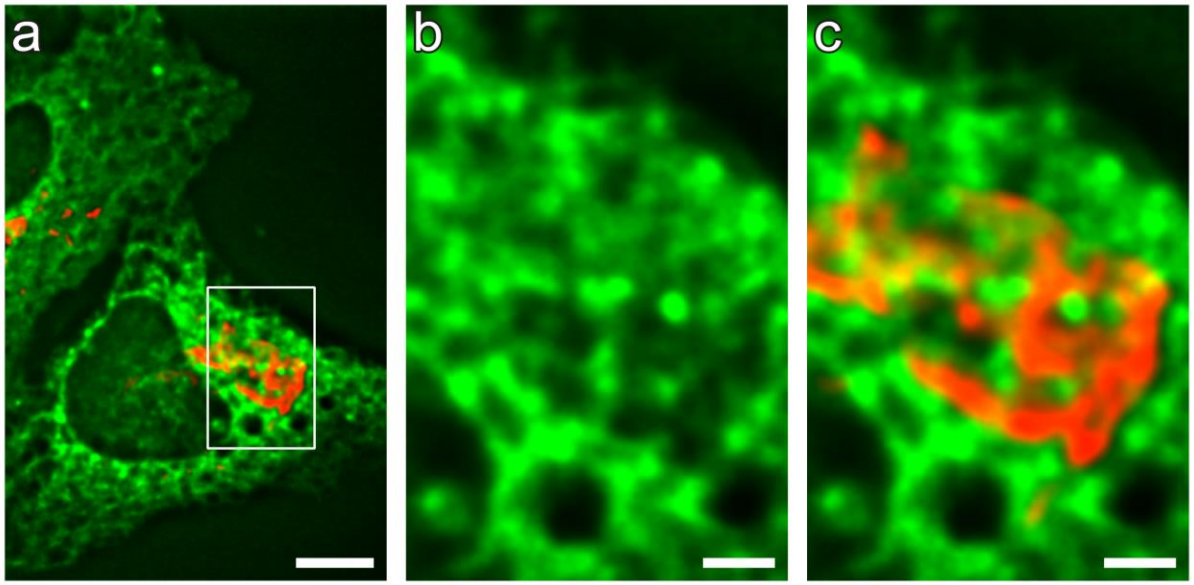

Figure 3.1-5: ER does not accumulate in direct proximity of β23 aggregates. HeLa cells expressing ER-GFP (green) and showing β23 aggregates (red). (a) The amount of ER surrounding the aggregate is similar to other regions of the cell. The aggregates are located in areas of the cell with overall high concentrations of ER. (b, c) Magnification of area indicated in (a). The space occupied by the β23 aggregate (c) is largely devoid of ER signal (b), but ER membranes are positioned in direct aggregate proximity. Scale bars: (a) 10 µm, (b, c) 2.5 µm.

3.1.2.2. Interactions with mitochondria

Similarly to the ER, in cryo-tomograms mitochondria were always found in very close proximity to the aggregates (**Figure 3.1-2**). In HeLa cells, they were often separated from aggregates by ER membranes (**Figure 3.1-2 c**), while in neurons they were more frequently situated in direct contact with the aggregates and occasionally even inside. As in the case of ER-fibril contacts, the outer mitochondrial membranes were not visibly deformed by fibrils. Additionally, tomograms showed that mitochondria in close proximity to the aggregates showed an apparently normal cristae structure, i.e. the cristae were not truncated or swollen (**Figure 3.1-2**, **Figure 3.1-3 b**).

To investigate the effects of the close association of mitochondria to the β-protein aggregates in the context of the whole cell, FLM on β23-expressing HeLa cells stained with the mitochondrial dye MitoTracker Green was performed. The overall amount of mitochondria located in the vicinity of the aggregates was not noticeably higher than in the rest of the cytosol (**Figure 3.1-6 a**). Also, regions occupied by aggregates showed less or no mitochondrial signal (**Figure 3.1-6 b**, dotted lines). These findings are in accordance with the cryo-ET observations that mitochondria are positioned around the aggregates and only rarely inside.

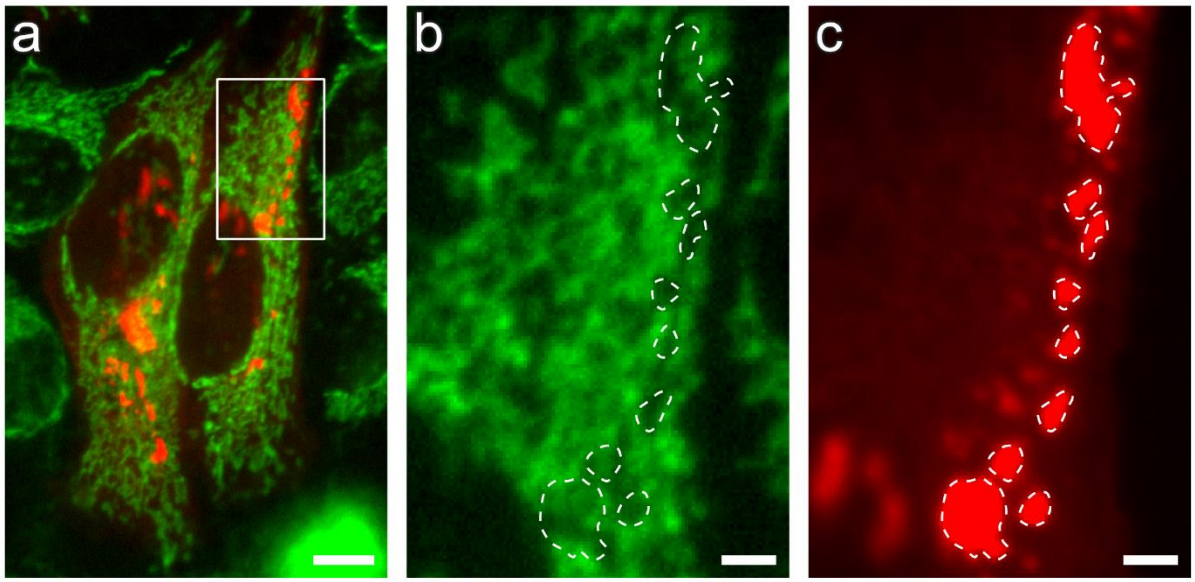

Figure 3.1-6: β23 aggregates do not alter the concentration of mitochondria in their vicinity. (a) The amount of mitochondria (green) surrounding the aggregate (red) is comparable to that of regions of the cell without aggregate. (b, c) magnification of area indicated in (a). Regions occupied by β23 aggregates (white dotted lines) are mostly devoid of mitochondria. Scale bars: (a) 10 µm, (b, c) 2.5 µm.

ER membranes and mitochondria found in the vicinity of aggregates were in close proximity to one another, very frequently forming mitochondria-ER membrane contact sites (MCS) (**Figure 3.1-2 c**, **Figure 3.1-8 a**). These are areas in which the outer mitochondrial membrane and ER membrane are opposed at a defined distance of ~ 10 nm at smooth ER and ~ 25 nm at rough ER (Csordás et al. 2006) and are important for multiple processes, e.g. phospholipid transfer, calcium signaling and modulation of mitochondrial membrane potential (MMP) (Naon and Scorrano 2014; Raturi and Simmen 2013). ER-mitochondria MCS have been found to be closely associated with NDDs (De Mario et al. 2017). In this light, further FLM analysis was performed by measuring the MMP of β-protein expressing cells.

In order to measure if mitochondrial function was affected by β-protein expression in neurons, an FLM experiment was performed to analyze the relative MMP (**Figure 3.1-7**). For this experiment neurons were transfected with either β23-mCherry (**Figure 3.1-7 c**), β4-mCherry or mCherry as a control. The cells were then stained with a mitochondrial dye, whose fluorescence intensity is independent from the MMP (I_i) (**Figure 3.1-7 b**), and a second dye whose fluorescence intensity is directly dependent on the MMP (I_d) (**Figure 3.1-7 a**). In order to compare these MMP values in between sample types, an MMP base-line was created by calculating the intensity ratio after depletion of the MMP with 1 µM Carbonyl cyanide-4-(trifluoromethoxy)phenylhydrazone (FCCP), a chemical compound that depolarizes the MMP. The relative MMP intensity ratio (I_r) was calculated as follows:

$$I_r = \frac{(I_d^u - I_i^d)}{(I_i^u + I_i^d)/2}$$

A small, non-significant decrease in the mean MMP of 6.9% ± 9.2% (mean ± SD) in β23 (43 cells) and of 3.8% ± 4.6% (mean ± SD) in β4-expressing neurons (58 cells) was observed when compared to the mCherry control (53 cells). This experiment suggests that β-protein aggregation leads to a slight

impairment in mitochondrial function. As it was shown that reduced mitochondrial function may in turn lead to protein aggregation (Lee et al. 2002), it is possible that the slightly increased mitochondrial impairment of β23 over β4 may contribute to the higher aggregation propensity and toxicity of β23.

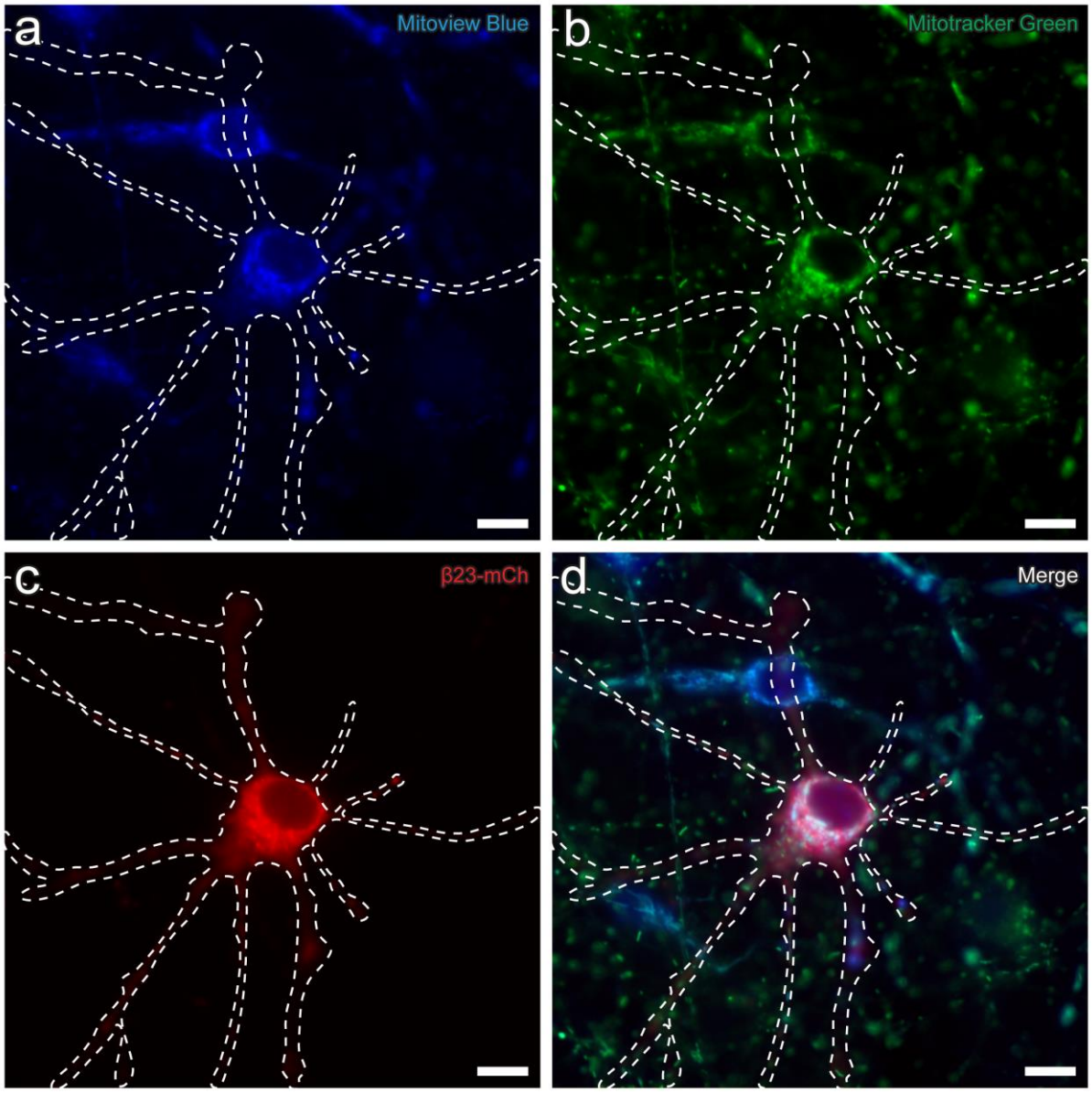

Figure 3.1-7: β-protein-expressing neurons show a reduced MMP. (a - d) Single slice of a z-stack of a neuron (dashed line) expressing β23 (c) (red) dyed with MitoTracker Green (b) (green) and MitoView Blue (a) (blue) and the corresponding merge (d) before depletion of the MMP. Using custom-made scripts, mitochondria were automatically localized in the MMP-independent MitoTracker channel in each slice of the stack and fluorescence intensities were measured in both green and blue channels. Scale bars: 10 µm

3.1.2.3. Interactions with macromolecules

Protein aggregates have been found to sequester cellular proteins and macromolecules (Klaips, Jayaraj, and Hartl 2018). Due to the high amounts of ribosomes found in close proximity to the

aggregates and the previously described sequestration of ribosome-related proteins in β-protein aggregates (Olzscha et al. 2011), we investigated both the structure and positioning of the ribosomes at the aggregates. Ribosomes are very electron dense, making them easily identifiable within tomograms (**Figure 3.1-8**). The position of macromolecules within cryo-tomograms was computationally determined by template matching performed by Qiang Guo (MPI of Biochemistry). Ribosomes were found embedded within β-protein aggregates as well in their outer perimeter, and were often contacted by fibrils (**Figure 3.1-4 a, c**). Visual comparison indicated high ribosome concentrations towards the outer aggregate perimeter and lower concentrations within the aggregate core. These findings are in contrast to the observations of (Bauerlein et al. 2017) on polyQ aggregates and of (Guo, Lehmer, et al. 2018) on C9orf72 poly-GA aggregates, where only minute amounts of ribosomes were found within the aggregates. However since, as previously mentioned, it was not possible to exactly identify the outer border of β-protein aggregates by cryo-ET, measurements and subsequent comparisons of the concentration of ribosomes within the aggregates were too inaccurate to withstand a critical analysis.

Especially in HeLa cells, ribosomes situated within the aggregates were sometimes organized in a polysome-like fashion, suggesting that they were translationally active (**Figure 3.1-8 f**). Additionally, it was previously shown that newly synthesized proteins which are sequestered to β-protein aggregates possess a high aggregation propensity in their pre-folded states (Olzscha et al. 2011). This supports the notion that ribosomes embedded within aggregates are translationally active, as proteins newly synthesized by them would be in direct contact with the aggregates and could therefore easily co-aggregate. As ribosomal proteins were previously reported to be sequestered by β-protein aggregates as well (Olzscha et al. 2011), subtomogram averaging was attempted in order to find out if interactions with fibrils affect the conformation of the ribosomes. However, preliminary results indicated no significant alterations in ribosome conformation and no distinct fibril contact point to the ribosomes could be observed.

Other than ribosomes, other large macromolecules were also identified within and around β-protein aggregates (**Figure 3.1-8 b**). Since (Guo, Lehmer, et al. 2018) had identified very high concentrations of proteasomes within C9orf72 poly-GA aggregates as well as TCP-1 Ring Complexes (TRiC) in their periphery, the amount and localization of both macromolecules was also analyzed for β-protein aggregates. Given that these two protein complexes are involved in proteostasis, seeking out their position and possible interactions with β-protein aggregates by template matching was of interest. Top views of both proteasomes and TRiC are easily identifiable by their ring-like structures (Guo, Lehmer, et al. 2018). Especially in the vicinity of the low contrast β-protein aggregates, these two molecules were often easily located. The molecules putatively identified as TriC were positioned in the outer rim and in proximity to the aggregates (**Figure 3.1-8 b** red molecules, **c**). Furthermore, proteasomes were sporadically embedded within the aggregate (**Figure 3.1-8 b** green molecules, **d**). The low concentration of these two molecules in the vicinity of the aggregates suggested that they do not play major roles in beta protein aggregation and hindered further structural and statistical analysis of their positions.

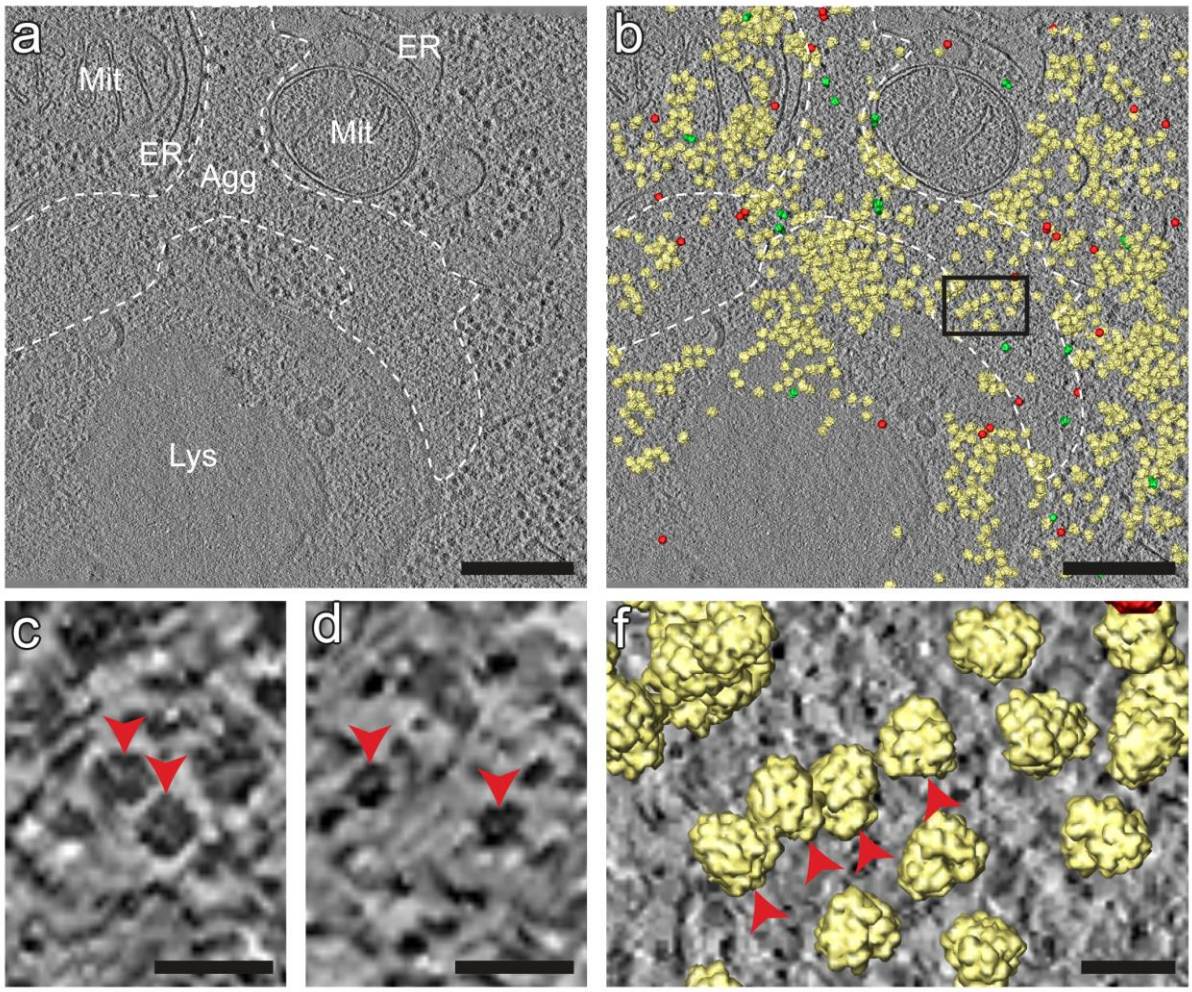

Figure 3.1-8: Macromolecules were situated within and in the direct surroundings of β-protein aggregates. (a, b) tomographic slice of a neuron expressing β4 superimposed with (b) and without (a) the 3D renderings of the ribosomes (yellow), proteasomes (green) and TriC molecules (red) in the tomographic volume. The 3D renderings of the molecules were generated by template matching and subsequent reintegration into the tomographic volume. The approximate position of the aggregate is indicated by the dotted line. High amounts of ribosomes surrounded the aggregate, while less were found within. Proteasomes and TRiC molecules were evenly distributed throughout the tomogram, regardless of the aggregate. (c) Magnification of ring-like particles putatively identified as TRiC (red arrowheads). (d) Magnification of ring-like particles putatively identified as proteasomes (red arrowheads) (f) Magnification of area indicated by black box in (b): polysome-like ribosome arrangement (red arrowheads). Agg, β-protein aggregate; ER, endoplasmic reticulum; Lys, lysosome; Mit, mitochondria. Scale bars: (a, b) 200 nm (c – f) 20 nm.

In tomograms of β23-expressing HeLa cells, bundles of intermediate filaments in contact with aggregates were occasionally observed (**Figure 3.1-9**). The diameter of these filaments measured approximately 12 nm, suggesting that they may consist of vimentin, which has a diameter of 10 - 12 nm (Sokolova et al. 2006) and is one of the most abundant intermediate filaments in HeLa cells (Bravo et al. 1982). In addition, vimentin had been previously described to be a β-protein interactor (Olzscha et al. 2011) and is involved in segregating inclusion bodies from daughter cells during mitosis in yeast (Ogrodnik et al. 2014). Therefore, FLM was used to analyze the distribution of vimentin in HeLa cells expressing β23 via immunofluorescence staining on a whole cell scale (**Figure 3.1-9**). Cells were transfected with β23-mCherry and vimentin filaments where stained using an anti-vimentin antibody. Analysis of the subsequent FLM indicated that 41% of HeLa cells with a β23-aggregate showed a

condensed or collapsed vimentin network (**Figure 3.1-9 b**, green arrowhead) while 39% showed an expanded network (**Figure 3.1-9 b**, yellow arrowhead) (20% classified for neither category). In comparison, only 17% of non-transfected neighboring cells showed a condensed network, while 57% had an expanded network (26% classified for neither category). Additionally, vimentin was often found in close association with the aggregates, especially in cells with a condensed network (**Figure 3.1-9 b**, green arrowhead). In these cases, the aggregates were often relatively small with a diameter of approximately 500 nm (**Figure 3.1-9 a**). These different morphologies could depend on multiple factors, including different stages of aggregation or the cells being in a different state of the cell cycle. However, since small aggregates were often very closely associated with vimentin, it is possible that they are transported within the cell along these bundles. Interestingly, intermediate filament bundles were not observed by cryo-ET in the vicinity of neuronal beta protein aggregates.

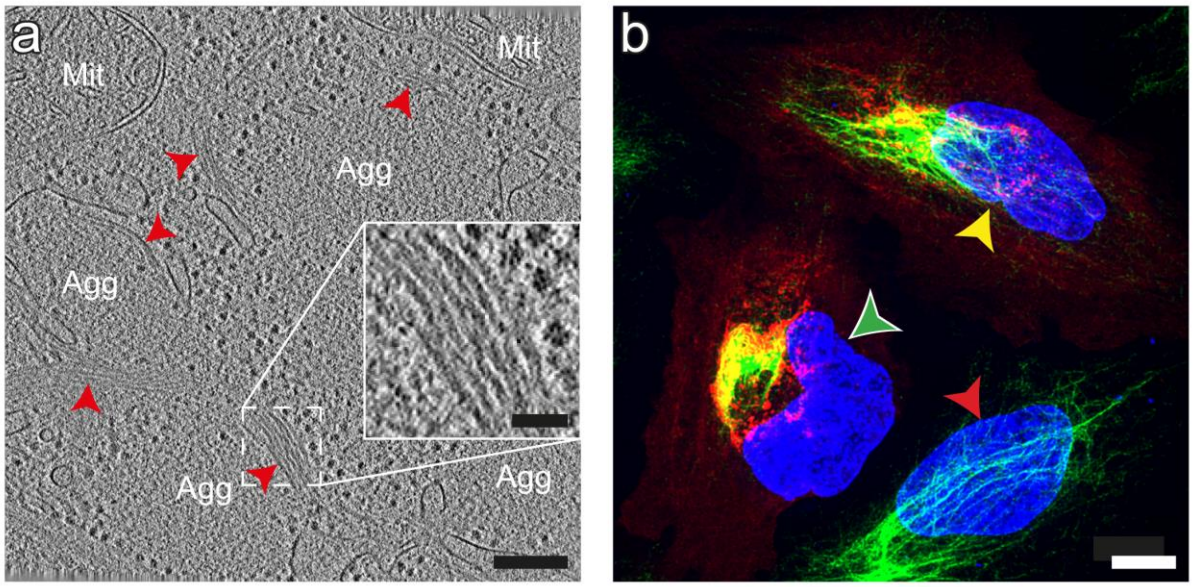

Figure 3.1-9: Vimentin intermediate filaments form condensed networks in β23-expressing HeLa cells in close association to the aggregates. (a) Tomographic slice of a β23-expressing HeLa cell. Small aggregate patches are in close contact with intermediate filament bundles. Inset: magnification of boxed region. (b) Immunofluorescence staining against vimentin intermediate filaments (green) in β23- (red) expressing HeLa cells. While the central left cell (green arrowhead) shows a very condensed vimentin network, the top (yellow arrowhead) and bottom right (red arrowhead) cells show expanded vimentin networks. Nuclei counterstained with DAPI (blue). Vimentin networks in β23-expressing cells are approximately twice as often condensed as in non-transfected cells. Agg, β-protein aggregate; Mit, mitochondrion. Scale bars: (a) 200 nm, inset 50nm, (b) 10 µm.

3.1.2.4. Accumulation of lysosomes

The most striking structural phenotype of β-protein expressing neurons were the morphological alterations of the endo-lysosomal system. Endosomal tubules were often found in direct contact with aggregates (**Figure 3.1-11 c**, **Figure 3.1-2 b**). The endosomal membranes could be discerned from other membrane structures such as the ER by multiple features, such as the lack of membrane-bound

ribosomes. Additionally, endo-lysosomal membrane structures have a light lumen, speckled with few electron dense proteins (**Figure 3.1-10 a**), whereas the ER lumen is substantially denser. Depending on the point in maturation within the endo-lysosomal pathway, the membrane of these organelles may also show protein decorations, either on the cytosolic and the luminal side (e.g. endosomes) or predominantly on the luminal side (e.g. lysosomes) (**Figure 3.1-10 b, c**).

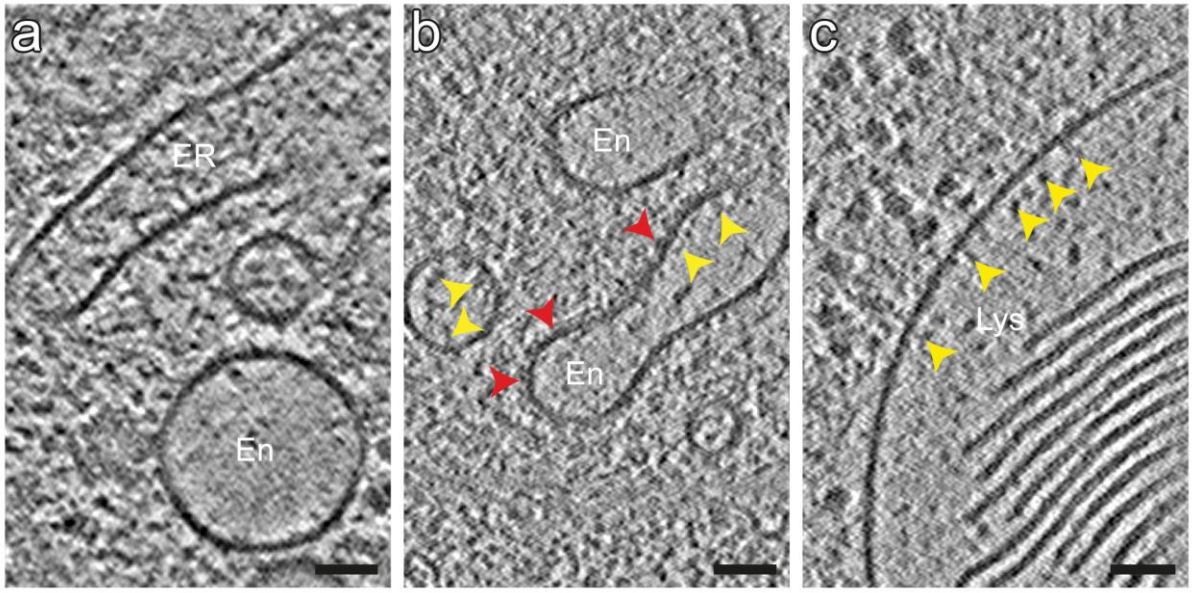

Figure 3.1-10: Endolysosomal organelles are morphologically distinguishable. (a - c) Tomographic slices of different endolysosomal structures. (a) While the ER lumen is filled with numerous electron-dense particles, endosomes show a light lumen with few densities. (b) Some endosomal structures show dense membrane coats on the cytosolic side (red arrowheads) and decoration on the luminal side (yellow arrowheads) of the membrane. (c) Autolysosomes predominantly show luminal membrane decorations (yellow arrowheads). En, endosome; ER, endoplasmic reticulum; Lys, lysosome. Scale bars: 50 nm.

Furthermore, β-protein-expressing neurons showed a remarkable accumulation of large, densely filled autolysosomes. These structures reached sizes of over 2.5 µm along the longest axis and often carried a large amount of membranes stacked upon each other in a multilamellar fashion (**Figure 3.1-11 d**). Additionally, these enlarged lysosomes possessed an electron dense lumen, indicating a high concentration of proteins. These organelles contained multiple small electron dense and light intraluminal vesicles (ILV), characteristic of late endosomes. Interestingly, β-protein aggregates were not found within the lysosomes. Such enlarged and densely filled lysosomes are indicative of an impairment of the lysosomal ability to degrade their cargo (Nixon et al. 2005; Demers-Lamarche et al. 2016). As the accumulation of enlarged lysosomes was particularly striking, and autophagy and lysosomal impairments have been described in many NDDs (Mathews et al. 2002; Mazzulli, Zunke, Isacson, et al. 2016; Wong and Holzbaur 2014), alterations of the lysosomal system in β-protein expressing cells were investigated further.

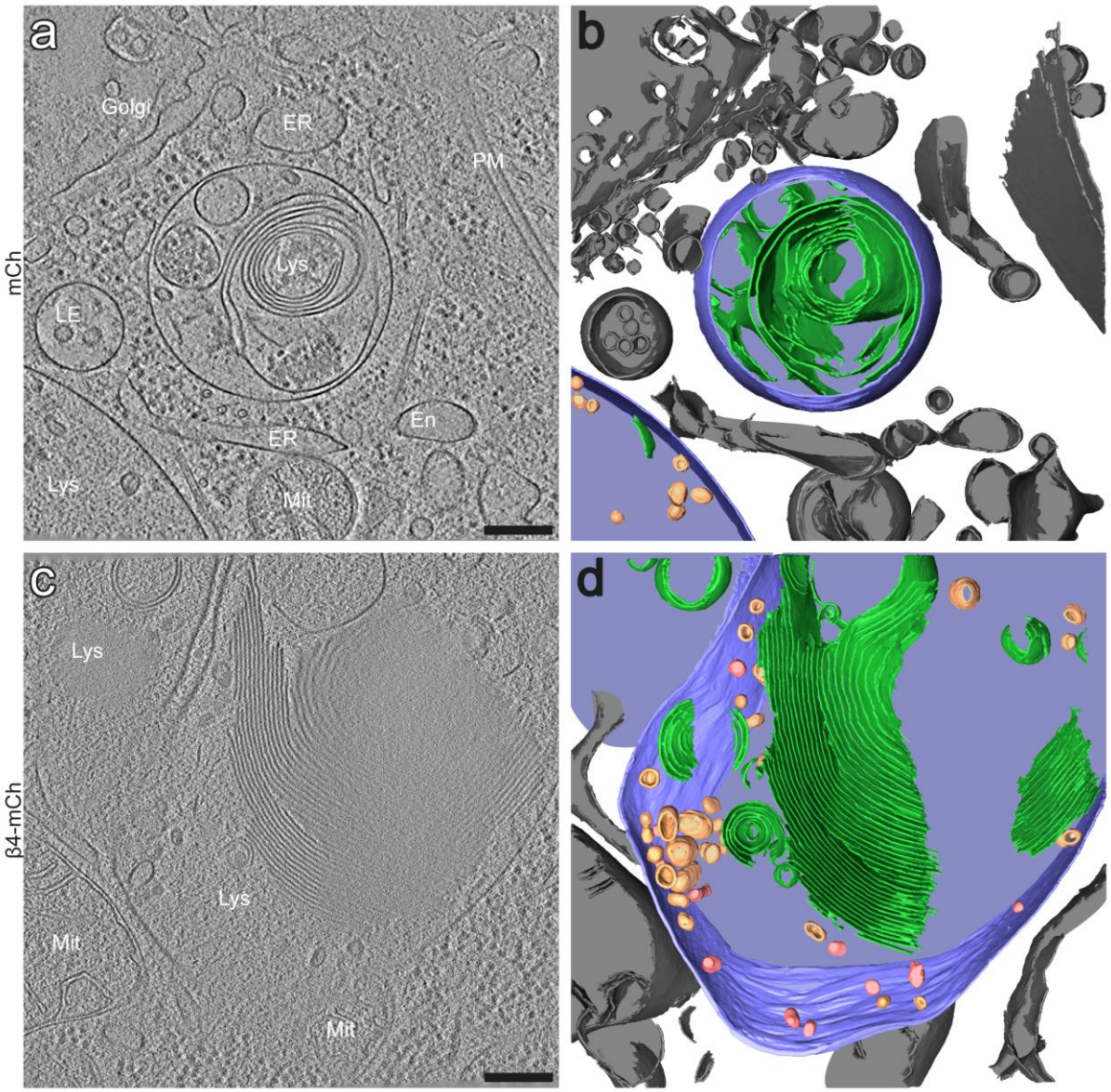

Figure 3.1-11: β-protein expressing neurons show enlarged, densely filled autolysosomes. (a, b) tomographic slice of an mCherry-expressing neuron and corresponding 3D rendering of respective tomogram. Control neurons expressing mCherry show autolysosomes occasionally containing small (5 to 10 membrane sheets) multilamellar membrane structures. (c, d) tomographic slice of a β4-expressing neuron and corresponding 3D rendering of respective tomogram. β-protein expressing cells show enlarged autolysosomes (over 2 µm in diameter) containing large (over 30 membrane sheets) multilamellar membrane structures. En, endosome; ER, endoplasmic reticulum; LE, late endosome; Lys, lysosome; Mit, mitochondrion; PM, plasma membrane. Color code in renderings: blue: limiting lysosomal membrane; green: lysosomal interior membranes; beige & light red: light and electron dense intraluminal vesicles; grey: other structures. Scale bars: 200 nm.

To address the alterations of the lysosomal system in a more global manner, we analyzed lysosome size and number in β-protein expressing neurons by FLM. For this experiment neurons were transfected with either β23-mCherry, β4-mCherry (**Figure 3.1-12 a**) or mCherry as a control. The cells were then stained with an endo-lysosomal dye (LysoTracker Green) which accumulates within acidic organelles (**Figure 3.1-12 b**). The cells were subsequently imaged by acquiring z-slices over the whole cell height. The imaged endo-lysosomes were then analyzed by marking the perimeter of each puncta in their corresponding in-focus plane (**Figure 3.1-12 b**, yellow lines). Evaluation of the marked

lysosomes indicated that lysosomes in β-protein expressing cells did not contain aggregates and had a significantly larger diameter than those of control cells (two tailed Mann-Whitney test; $p < 0.001$) (**Figure 3.1-12 d**). While the average diameter of lysosomes in neurons expressing β23 was 0.82 ± 0.29 µm (mean ± SD, N = 1838 lysosomes from 46 cells), and 0.85 ± 0.31 µm (mean ± SD, N = 1595 lysosomes from 44 cells) in β4-expressing cells, that of control neurons was 0.65 ± 0.26 µm (mean ± SD, N = 2148 lysosomes from 36 cells). The fraction of lysosomes larger than 1 µm in diameter was 18.2% in β4-expressing cells and 15.1% in β23-expressing cells, in comparison to 4.8% in mCherry-expressing control cells. On the other hand, β-sheet-expressing cells showed significantly reduced numbers of lysosomes when compared to controls. On average, β4- and β23-expressing cells possessed 40% and 25% fewer lysosomes than the control (two tailed Mann-Whitney test; $p < 0.001$) (**Figure 3.1-12 e**). These findings correlate with the cryo-ET observations that β-protein expressing cells show larger lysosomes than control neurons. Interestingly, these two effects seem to cancel each other out in respect to the total lysosomal mass, as lysosomal-associated membrane protein 1 (LAMP1) western blot indicated that the total lysosomal mass was comparable in β23-expressing HeLa cells and controls (**Figure 3.1-13 c, d**).

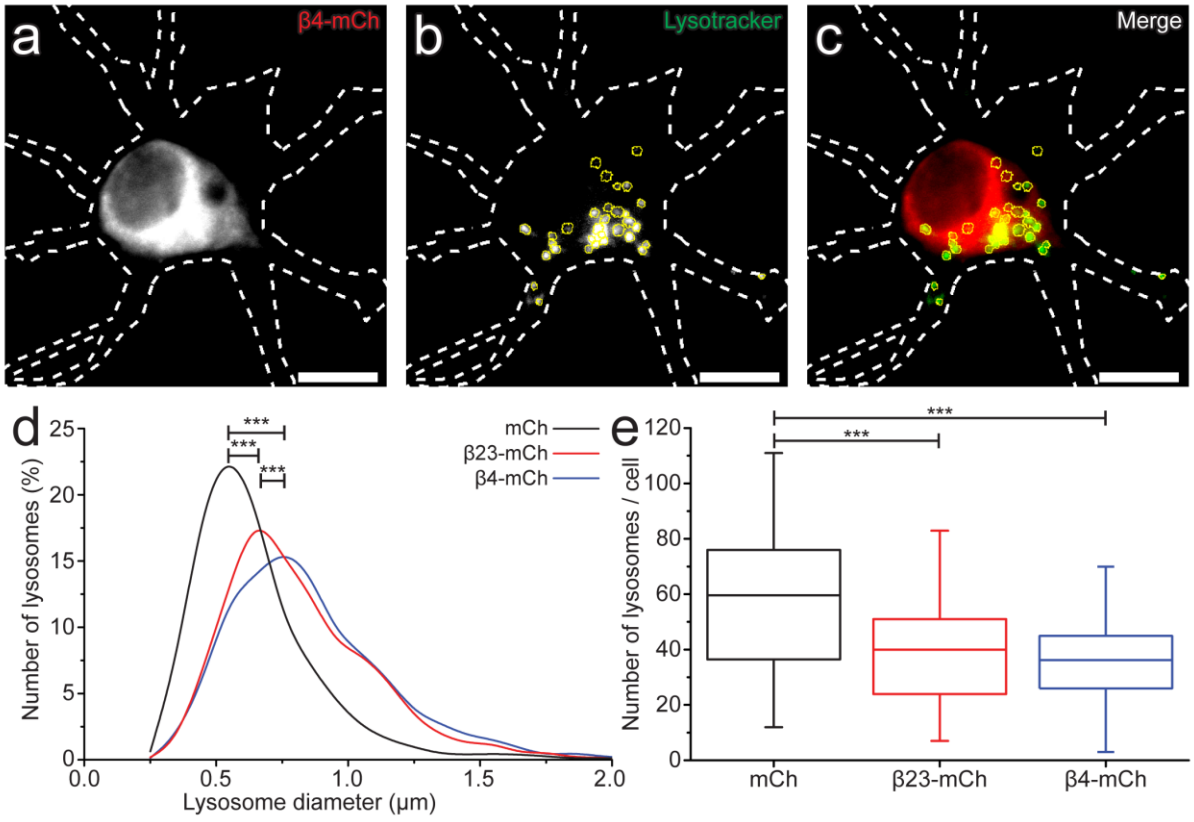

Figure 3.1-12: β-proteins increase the diameter of lysosomes in neurons while decreasing the number of lysosomes per cell. (a - c) Single slice of a z-stack of a neuron (dashed line) expressing β4 (a) dyed with LysoTracker Green (b) and the corresponding merge (c). Lysosomes within the cells were marked at the z-height at which they were in focus. Lysosomes from all planes from this cell are indicated in yellow (b, c). The size and number of lysosomes in β-protein expressing neurons were analyzed in each cell. (d) The diameter of lysosomes in β-protein expressing cells is shifted towards larger lysosomes when compared to the mCherry control. (e) The number of lysosomes per cell in β-protein expressing neurons is significantly reduced when compared to the mCherry control. Scale bars: 10 µm. Statistics: two tailed Mann-Whitney test; p: *** < 0.001.

3.1.3. Functional alterations of lysosomes by β-protein aggregates

We further investigated whether the abnormal endo-lysosomal morphology was linked to functional alterations in these organelles via western blot and qPCR analysis. As these biochemical methods rely on a preferably homogeneous sample, HeLa cells transfected with β23 were analyzed. HeLa cells showed a significantly increased transfection rate in comparison with neurons, and low β23-expression rates would have diluted the effects of β23 in these population based methods. Western blot and qPCR experiments were performed in the lab of Nuno Raimundo (University of Göttingen).

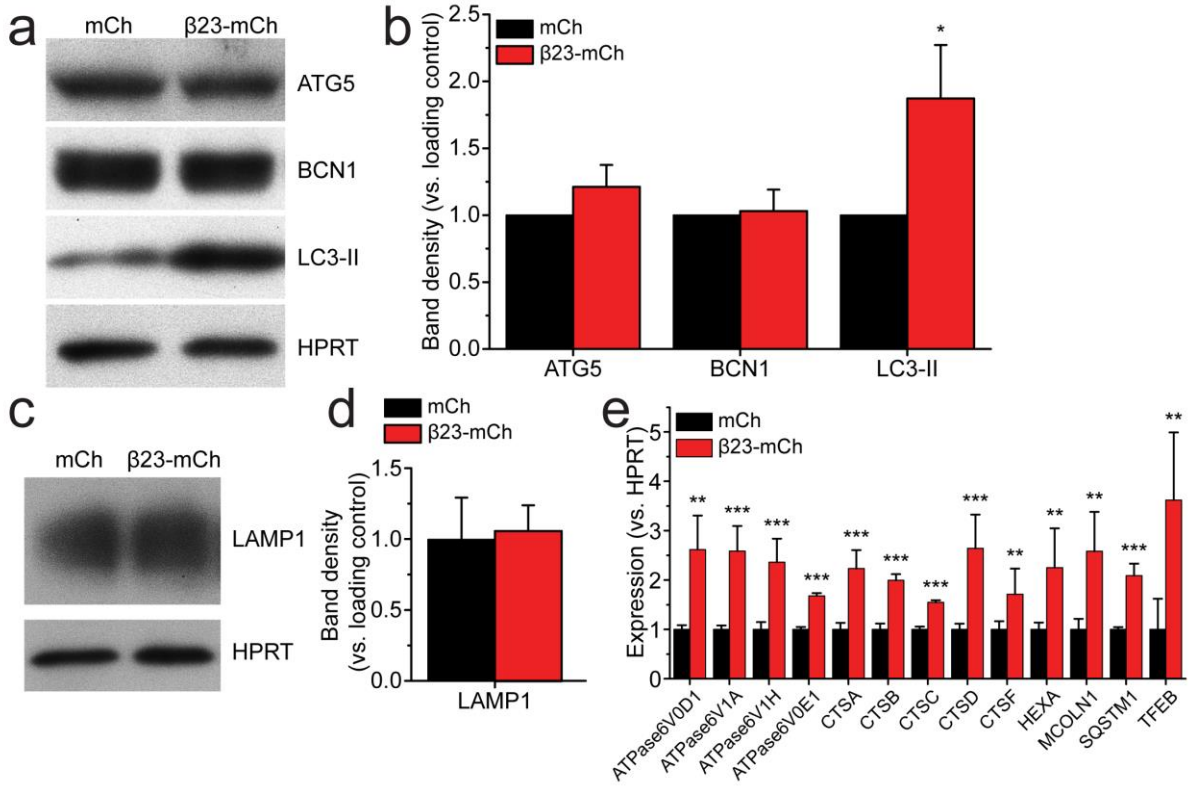

Figure 3.1-13: β23-expressing HeLa cells show increased LC3-II protein levels and lysosomal protein expression levels. (a, b) Western blots of three autophagosomal proteins in β23- and mCherry-expressing HeLa cells and their quantification. ATG5 and BCN1 levels in β23 cells are comparable to the control. LC3-II is significantly enriched in β23-expressing cells. HPRT: Hypoxanthine Guanine Phosphoribosyltransferase (c, d) Western blot of LAMP1 (c) and its quantification (d). LAMP1 levels are not affected by β23-expression. (e) Comparison of transcription levels of selected lysosomal genes. β23-expressing cells show a significant increase in transcription of ATPase6 subunits, cathepsins, hexosaminidase A, mucolipin-1, sequestosome-1 and transcription factor EB. Statistics: two tailed t-test; p: * < 0.05, ** < 0.01, *** < 0.001.

An upregulation of lysosomal gene transcription is indicative of impaired lysosomal degradation (Roczniak-Ferguson et al. 2012; Martina et al. 2014). Therefore, the levels of transcription of many lysosomal genes were measured via qPCR (**Figure 3.1-13 e**). Specifically the levels of V-type ATPase subunits (ATPaseV), which as a complex is responsible for the acidification of endo-lysosomal organelles, cathepsins (CTS) and hexosaminidase A (HEXA), responsible for the degradation of lysosomal cargo, mucolipin-1 (MCOLN1), a non-selective cation channel playing a role in Ca^{2+} transport, sequestosome-1 (SQSTM1), a selective macroautophagy receptor, and transcription factor EB (TFEB),

a transcription factor responsible for activating the expression of lysosomal and autophagy genes, were measured. The transcription levels of all of these proteins were significantly upregulated. On the other hand, western blot analysis showed that LAMP1 protein levels, indicating the total amount of lysosomes present within the cells, were comparable to those of control cells. This suggests that β-protein expressing cells tried to increase their lysosomal function by increasing the production of lysosomal proteins, but failed to do so.

The lysosomal degradation of cellular material is initiated via autophagy. At the same time, correct lysosomal function is necessary for the fusion of autophagosomes and the degradation of their cargo (Gutierrez et al. 2004; Jager et al. 2004). Therefore, the ratio of protein levels of autophagosomal proteins at different maturation stages can suggest an impairment in autophagy or lysosomal function. Western blot analysis was used to measure the levels of three autophagosomal proteins in β23-expressing HeLa cells. Cytosolic microtubule-associated protein 1A/1B-light chain 3 (LC3) is bound to the autophagosomal membrane during autophagosome assembly, forming LC3 phosphatidylethanolamine conjugate (LC3-II) (Kabeya et al. 2000). Once the autophagosome forms an autolysosome by fusing with a lysosome, intra-autophagosomal LC3-II is degraded (Mizushima and Yoshimori 2007). This makes LC3-II a good marker for overall autophagosome amounts within cells (Kabeya et al. 2000). On the other hand, autophagy protein 5 (ATG5) and beclin-1 (BCN1) are proteins involved only in the early stages of autophagosome assembly (Mizushima et al. 1998). ATG5, conjugated with ATG12, is required for the lipidation of LC3 (Tanida et al. 2002). BCN1 interacts with numerous autophagy related proteins and is important for the nucleation of pre-autophagic structure, which matures into the autophagosome (Kang et al. 2011).

Cells showed higher levels of LC3-II, but stable levels of both ATG5 and BCN1 when compared to the control (**Figure 3.1-13 a, b**). This indicates that autophagosome generation is not affected by β-protein expression, while degradation is impaired. Additionally, in contrast to lysosomes and autolysosomes, autophagosomes were not frequently observed in neurons by cryo-ET, consistent with the notion that autophagosomes quickly mature to autolysosomes, but are not efficiently degraded at this stage.

As a different marker for measuring this lysosomal impairment, the relative lysosomal acidity was also investigated (**Figure 3.1-14**). The function of many lysosomal proteins relies on an acidic environment (Journet et al. 2002). Therefore, a reduced lysosomal acidification results in a reduction in the lysosomal capability to degrade cargo (Williamson and Hiesinger 2010; Bright, Davis, and Luzio 2016) and reduced lysosomal acidity can be used as a marker for lysosomal impairment (Raben et al. 2009). For this experiment, β-protein and mCherry-expressing neurons were simultaneously dyed with two different 10000 MW dextrans conjugated to Oregon Green or Cascade Blue. While the fluorescence intensity of Cascade Blue (I_i) is independent of its surrounding pH, the fluorescence intensity of Oregon Green (I_d) is quenched at low pH. Cells were incubated for 60 min with both dextrans, the extracellular dextran was then washed away and the cells were imaged after further 24 h of incubation. At this point, the dextran taken up by the cells via endocytosis was primarily located within terminal lysosomes (Humphries IV, Szymanski, and Payne 2011). β-protein and mCherry-expressing cells were located via FLM and imaged in both green and blue channels over the whole cell height by acquiring z-

slices. Similarly to the analysis of lysosome size and number, the imaged lysosomes were then analyzed by marking the perimeter of each puncta in their corresponding in-focus plane. The intensity ratio of the pH dependent dye to the pH independent dye (I_r) was then calculated for each lysosome, allowing a comparison of relative pH levels between β-protein expressing neurons and mCherry control neurons:

$$I_r = \frac{I_d}{I_i}$$

These FLM experiments indicate that the average lysosomal acidity in β-protein expressing cells was significantly reduced compared to control (one tailed directional Mann-Whitney test; $p < 0.001$) (**Figure 3.1-12 d**). While the average acidity ratio of lysosomes in neurons expressing β23 was 2.42 ± 0.59 (mean ± SD, N = 408 lysosomes from 18 cells), and 2.39 ± 0.55 (mean ± SD, N = 389 lysosomes from 14 cells) in β4-expressing cells, that of control neurons was 2.22 ± 0.62 (mean ± SD, N = 681 lysosomes from 19 cells). As the fluorescence intensity measurements were not calibrated to absolute pH values, no absolute pH values could be calculated. Therefore, it is only possible to qualitatively say that lysosomal pH was higher in β-protein expressing neurons than in the mCherry control.

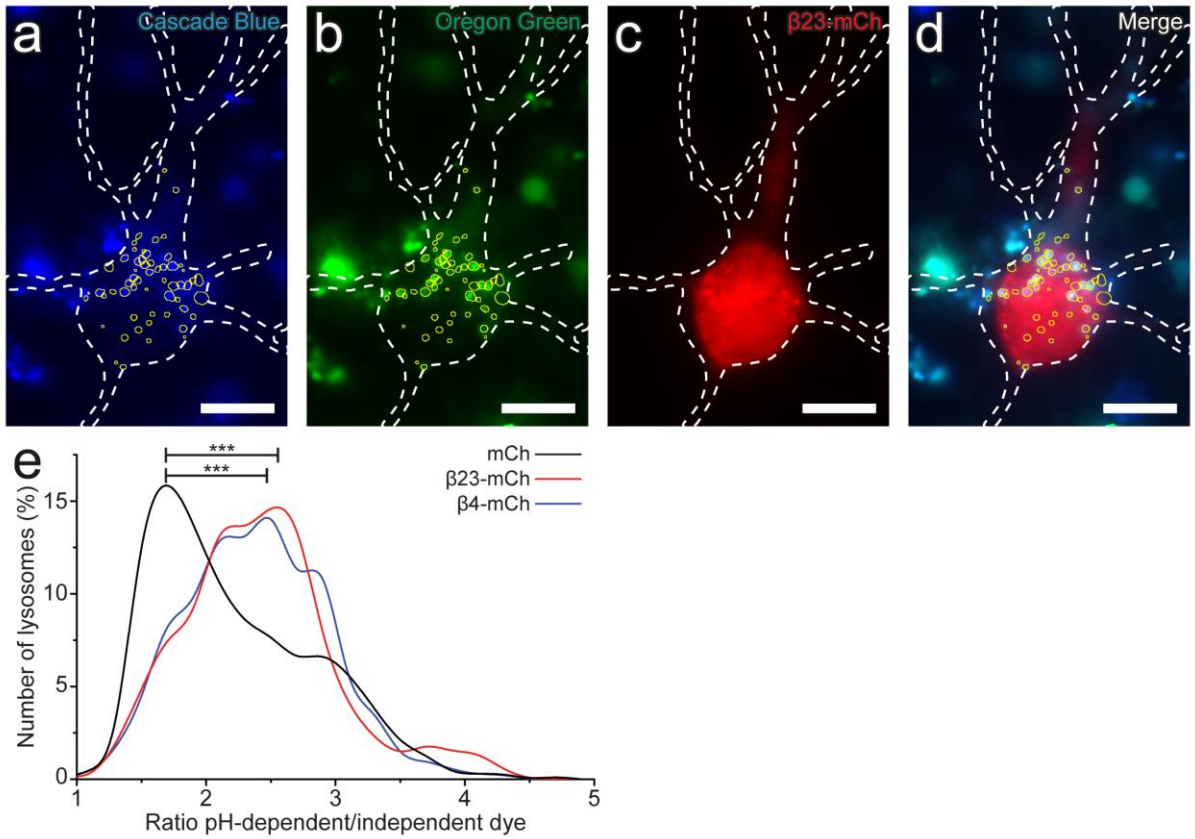

Figure 3.1-14: β-protein expressing neurons show a reduced lysosomal acidity. (a – d) Single slice of a z-stack of a neuron (dashed line) expressing β23 (c) (red) dyed with Dextran Oregon Green MW 10000 (b) (green) and Dextran Cascade Blue MW 10000 (a) (blue) and the corresponding merge (d). Lysosomes within the cells were marked at the z-height at which they were in focus. Lysosomes from all planes from this cell are indicated in yellow. The fluorescence intensity of Dextran Cascade Blue is pH independent, while the fluorescence intensity of Dextran Oregon Green is reduced with an increased acidity. (e) Quantification of the number of lysosomes from β-protein and mCherry control neurons showing specific intensity ratios of the pH-dependent dye and the pH-independent dye. Lysosomes of B-protein expressing neurons show significantly increased intensity ratios indicating higher luminal pH. N cells / lysosomes: β23-mCherry 18 / 408, β4-mCherry 14 / 389, mCherry 19 / 681. Scale bars: 10 µm. Statistics: one tailed directional Mann-Whitney test; p: *** < 0.001.

In previous studies on the effects of protein aggregates on the proteostasis network it was shown that protein aggregates aberrantly interact and sequester proteostasis components (Park et al. 2013; Olzscha et al. 2011; Yu et al. 2014). This may lead to an increased aggregate toxicity by a decline in the function of the proteostasis network (Hipp, Park, and Hartl 2014). In these studies, mass spectrometry was utilized to analyze which proteins are sequestered and to what extent they are thus removed from the pool of proteostasis components.

In order to further understand the mechanism behind this lysosomal impairment, mass spectrometry was performed on virally transduced neurons expressing β4, β17 or β23 by Irene Riera Tur and Daniel Hornburg (MPI for Neurobiology & MPI for Biochemistry, respectively). The identity and amount of proteins which are sequestered by the β-protein aggregates were measured. Interestingly, the protein that was most sequestered by all three types of β-protein aggregates was the µ3A subunit of the adaptor protein (AP) -3 (AP-3) complex. AP-3 is a protein complex involved in the transport of lysosomal membrane proteins from the early endosomal system to the lysosomes (Cowles et al. 1997). Therefore, the sequestration of AP-3 µ3A subunit could disrupt the transport of lysosomal membrane proteins, leading to impaired lysosomal function. This is indeed the case in mice carrying mutations in the AP-3 β3A subunit, where lysosomal membrane proteins are mislocalized to the plasma membrane (Dell'Angelica et al. 1999). Therefore, AP-3 sequestration could underlie the lysosomal defects observed here.

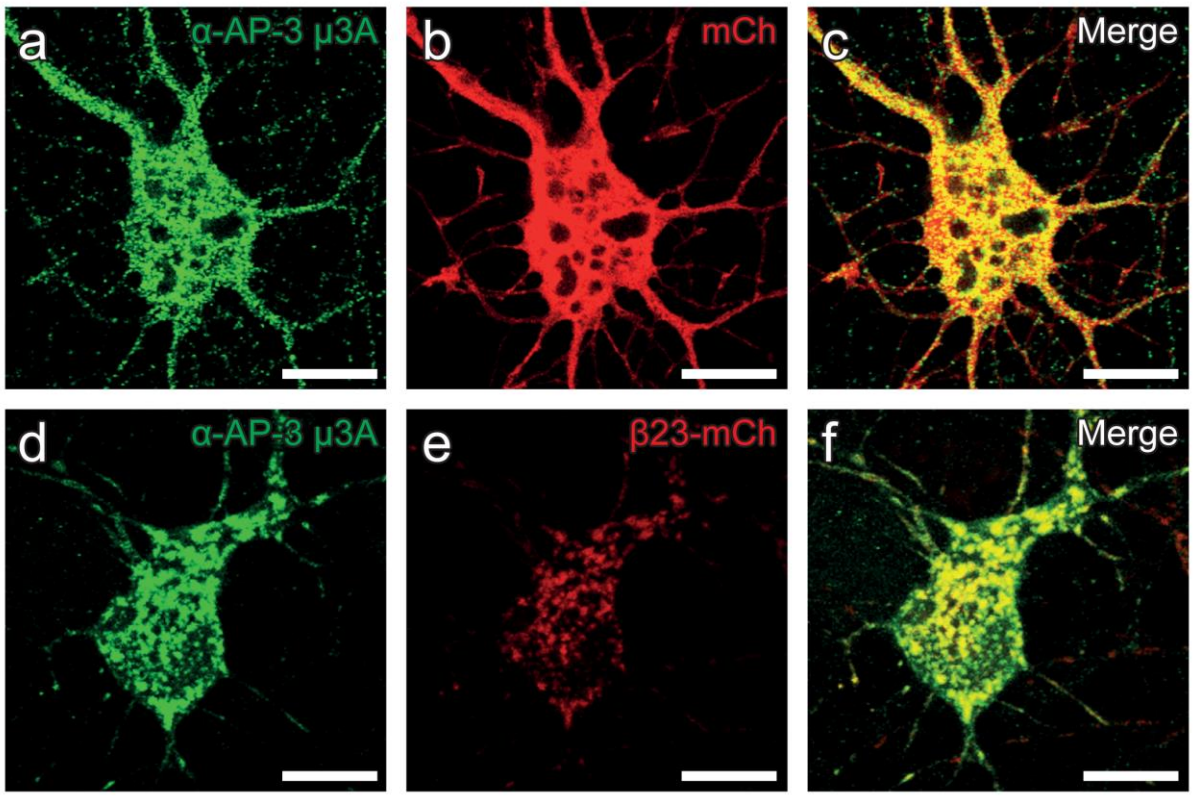

Figure 3.1-15: β-protein expressing neurons sequester AP-3 µ3A. mCherry- (a - c) and β23- (d - f) (red) expressing neurons co-expressing AP-3 µ3A stained with an anti-AP-3 µ3A antibody (green). mCherry control neurons show a diffuse AP-3 µ3A distribution, while β23-expressing neurons show a co-localization of β23 aggregates and AP-3 µ3A. Scale bars: 10 µm

To test this hypothesis we first performed FLM immunostaining experiments of β-protein and AP-3 µ3A co-expressing neurons, which confirmed the accumulation of AP-3 µ3A to β-protein aggregates (**Figure 3.1-15**). Next we analyzed whether AP-3 µ3A sequestration leads to neuronal toxicity. Thus, active caspase3 viability assays were performed on neurons co-expressing either β4 or β23 and AP-3 µ3A or EGFP as control (**Figure 3.1-16**). While EGFP-co-expressing control cells showed 26% ± 4% (mean ± SD) (β23) and 36% ± 10% (mean ± SD) (β4) caspase3 positive staining, only 6% ± 5% (mean ± SD) (β23) and 11% ± 1% (mean ± SD) (β4) of AP-3 µ3A overexpressing neurons showed caspase3 positive staining (**Figure 3.1-16 g**). Therefore, overexpression of AP-3 µ3A significantly reduced β-protein toxicity (two tailed t-test; p β23 < 0.001, p β4 < 0.01). Both experiments were performed by Archana Mishra (MPI for Neurobiology).

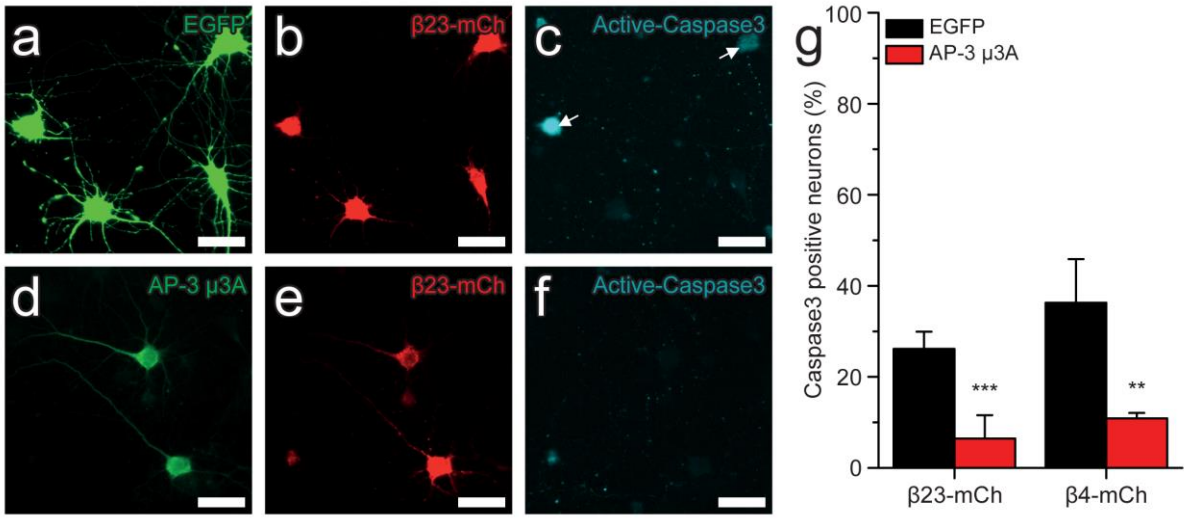

Figure 3.1-16: β-protein expressing neurons co-expressing AP-3 µ3A show reduced toxicity. (a - f) β23- (red) expressing neurons co-expressing EGFP (a) and AP-3 µ3A (d) (green) stained for active caspase-3. Active caspase-3 positive staining indicates apoptotic cell death (c, white arrows). (g) β-protein expressing neurons show apoptosis significantly less often when co-expressing AP-3 µ3A. Scale bars: 25 µm. Statistics: two tailed t-test; p: ** < 0.01, *** < 0.001.

Altogether, these experiments show that the formation of β-protein aggregates leads to lysosomal impairments similar to those observed in NDDs, which may result from the sequestration of a critical component of the lysosomal transport system (see Discussion).

3.2. Time-resolved aggregation in HEK293 cells

Protein aggregation in cells is a very heterogeneous process. For instance, β-protein aggregates in HeLa cells form in very different time scales and exert toxicity at different stages. This is due to a variety of factors, for example the cell being in different cell cycle stages or variations in transfection efficiencies or β-protein expression levels. In order to study the process of aggregation in a synchronized and time resolved manner, an artificial aggregating protein called aggregating destabilizing domain (AgDD) was created (Miyazaki et al. 2016).

The AgDD protein consists of a destabilizing domain (DD) derived from the human FK506-binding protein 12 protein tagged with GFP and fused to a nuclear export signal at its N-terminus (Miyazaki et al. 2016). Destabilizing domain proteins can be stabilized by an externally applied ligand in order to prevent misfolding of the DD (Banaszynski et al. 2006). The nuclear export signal is critical to elicit aggregation (Maynard-Smith et al. 2007). Miyazaki et al. showed that AgDD stably expressed in HEK293 cells is diffusely distributed throughout the cell in the presence of a stabilizing ligand Shield-1 (S1), but begins to form multiply aggregates immediately upon the removal of S1. These aggregates join together in the course of several hours, until few large aggregates are found within each cell. This study also reported that p62, a receptor and marker for selective macroautophagy, co-localizes with AgDD aggregates after several hours.

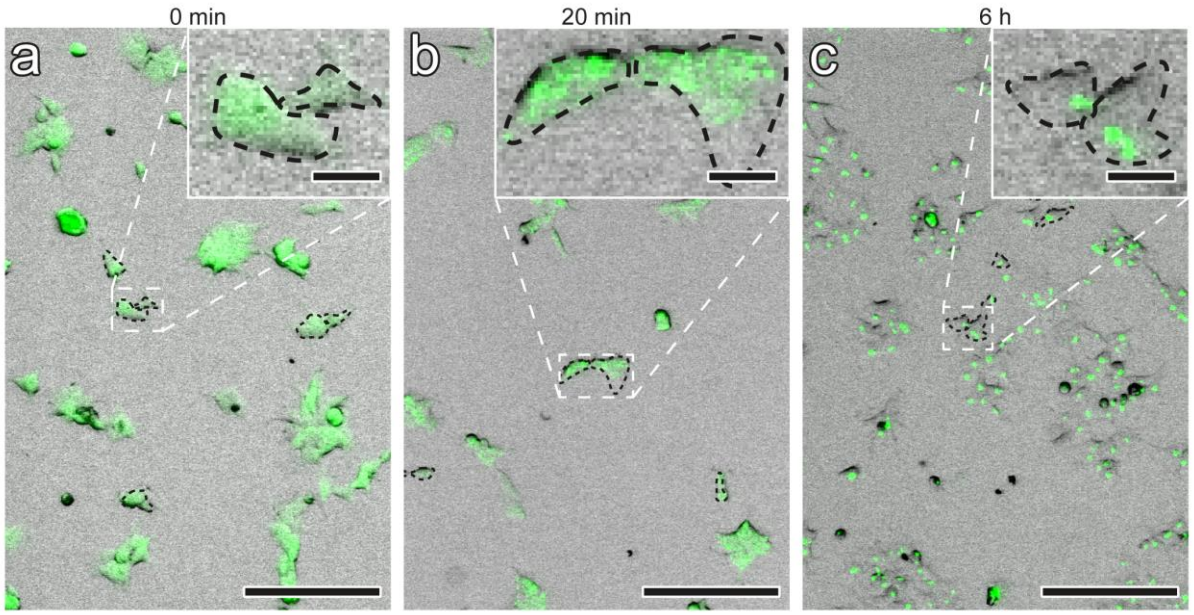

Figure 3.2-1: HEK 293 AgDD cells show aggregation of AgDD after removal of S1. (a, b, c) Merge of bright-field and fluorescence (green) images of HEK 293 AgDD cells 0 min (a) 20 min (b) and 6 h (c) after removal of S1 and magnifications (insets). Single example cells indicated by dotted black line. (a) AgDD is diffusely dispersed within the cells. (b) Numerous small aggregates are dispersed within the cells. (c) Each cell contains few large aggregates. Scale bars: 200 µm, insets 25µm.

The use of AgDD proteins provides an excellent model for synchronous and time-resolved study of protein aggregates. The goal of this project was to determine the structure of AgDD aggregates at

different time points and to elucidate their change in morphology and interaction with the cell over time. As all the cells from this cell line were supposed to form aggregates once S1 was removed from the cells, determining which cell had formed aggregates for later FIB milling as in the β-protein project via cryo-LM was not necessary. To verify this, HEK293 cells expressing AgDD-GFP were imaged using live cell LM (**Figure 3.2-1**). As previously reported by (Miyazaki et al. 2016), all cells had formed multiple small aggregates after 20 min and few large aggregates after 6 h.

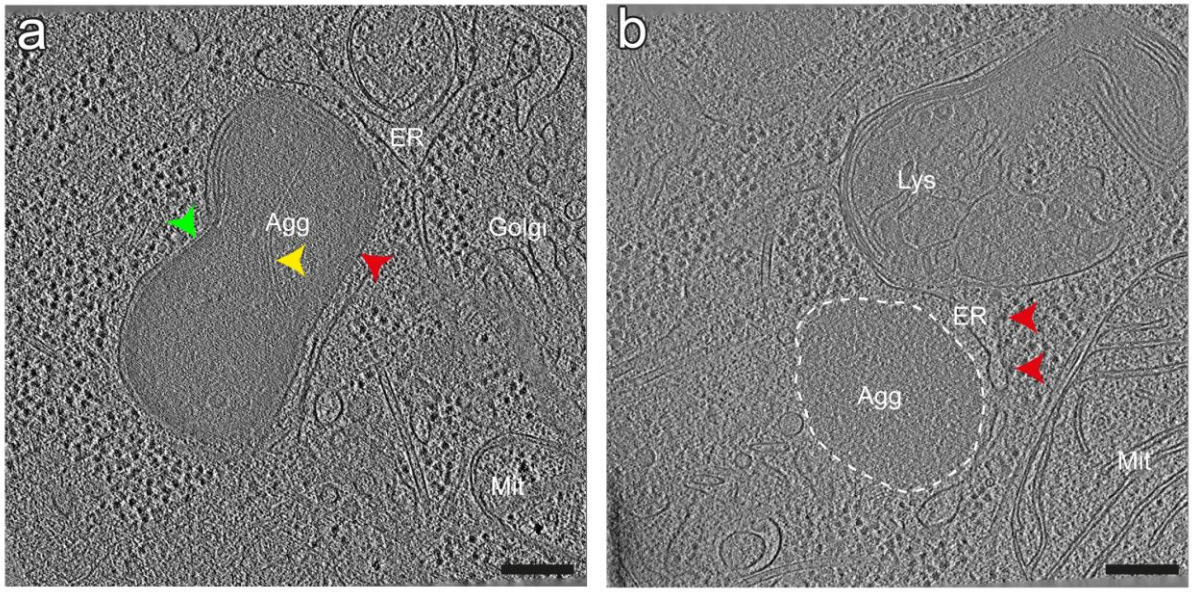

Figure 3.2-2: Cryo-ET reveals two distinct forms of AgDD aggregates after 10 min post S1 removal. (a, b) Tomographic slices of aggregates from AgDD expressing cells 10 min post S1 removal. (a) Medium sized aggregate encapsulated by a single membrane (red arrowhead). Parts of the aggregate are sub-compartmentalized by an additional membrane (green arrowhead). The aggregate consists of an electron dense amorphous mass composed of a grainy electron density. The mass is perturbed by membranes (yellow arrowhead). (b) Small, non-encapsulated aggregate (dashed line) consisting of a less electron dense amorphous mass composed of a grainy electron density. The aggregate is not surrounded by a membrane and is homogeneous in texture. ER membranes are closely associated to the aggregate and a lysosome positioned in close proximity to the aggregate. Red arrowheads: ER associated ribosomes. Agg, AgDD aggregate; ER, endoplasmic reticulum; Lys, lysosome; Mit, mitochondrion. Scale bars: 200 nm. Defocus -0.5 µm (phase plate).

To elucidate the structure of AgDD aggregates via cryo-ET, cells were cultured on EM grids and plunge-frozen after 10 min upon removal of S1. After FIB milling, grids were imaged in the TEM and tomograms acquired at the 10 min time point using the VPP at -0.5 µm defocus. Two distinct types of aggregates were found at this time point: electron dense aggregates encapsulated by a membrane and less electron dense aggregates without a surrounding membrane (**Figure 3.2-2 a, b** respectively). Dense aggregates tended to be larger than the lighter aggregates. The encapsulated aggregates consisted primarily of an amorphous mass with a homogeneous, grainy electron density indicative of high protein concentrations (**Figure 3.2-2 a**). They were interspersed by membranes and double membranes ranging through the aggregates. The overall surrounding membrane was a single membrane, excluding the possibility that these aggregates are engulfed within an autophagosome but rather hinting them to be within an autolysosome. However, parts of the aggregate were sub-compartmentalized with another surrounding membrane. This could indicate that the aggregates are

comprised of multiple smaller aggregates coalesced into single one, and fits with previous observations (Miyazaki et al. 2016).

Light aggregates were not encapsulated by a membrane (**Figure 3.2-2 a**). These aggregates were composed of a homogeneous granular amorphous mass unperturbed by any other structures. ER membranes were found in close proximity and in association with the aggregates. These findings suggest that some AgDD aggregates were not engulfed by an autophagic or lysosomal membrane immediately after their formation, and fits with the observations made by (Miyazaki et al. 2016) that the autophagy marker p62 only partially co-localizes with AgDD aggregates after some time.

To find out whether AgDD aggregates formed at a later time point differed in structure from those observed after 10 min after S1 removal, preliminary data on aggregates formed by cells frozen after 8 h after S1 removal was acquired. Correlation with cryo-FLM data confirmed the presence of few large aggregates. Tomograms were acquired using the objective aperture and -9 µm defocus. Up to 15 aggregates per lamella were identified via cryo-ET in cells incubated for 8 h without S1 (**Figure 3.2-3 a**). These aggregates were up to 2 µm in size across the longest axis. However, the lamellae were only approximately 200 nm thick, so these multiple aggregates might have been connected on a plane which had been removed by milling, and may therefore correspond to the large puncta observed per cell by FLM. Additionally, the aggregates were often positioned very close together, with only few tens of nanometers in between. These would be perceived as one aggregate by FLM, as these distances are below the resolution limit.

Aggregate morphologies similar to those at the 10 min time point were found at the 8 h time point (**Figure 3.2-3 b, c**). The non-encapsulated aggregates at the 8 h time points were comparable in structure to those from the 10 min time point (**Figure 3.2-3 c**), as they were also composed of an unperturbed homogeneous granular amorphous mass. However, the membrane encapsulated aggregates were often irregularly shaped, less homogeneous in texture and contained more membranes as well as small vesicles positioned within the mass (**Figure 3.2-3 b**). These vesicles showed either an electron dense or light lumen and looked similar to ILVs normally found in late endosomes and lysosomes. These findings suggest that aggregates are encapsulated by membranes and subjected to degradative processes, altering their structural appearance over time.

Interestingly, none of the aggregates were found to be filamentous as was previously reported (Miyazaki et al. 2016). However, these previously reported observations were based on negatively stained samples, and no detailed information on the EM sample preparation was given. Therefore, as membranes are often especially strongly stained by heavy metal staining, the filamentous structures might very well be the membranes found protruding into the membrane encapsulated aggregates.

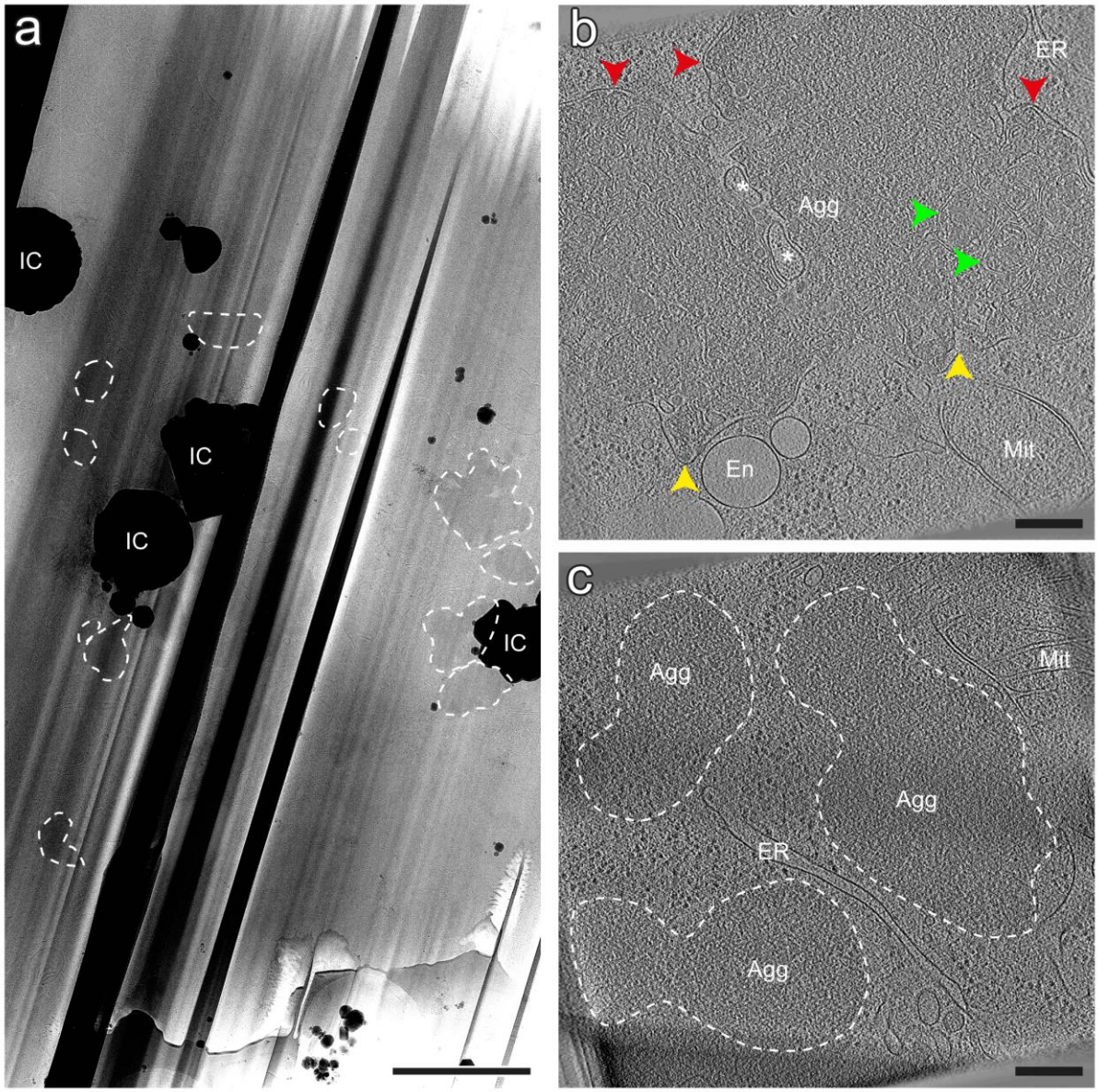

Figure 3.2-3: Aggregates at 8 h after S1 removal are similar to those after 10 min post S1 removal. (a) TEM overview image of a lamella from an AgDD expressing cell incubated for 8 h without the presence of S1. Multiple sites of aggregates were found (dashed lines). (b, c) Tomographic slices of aggregates from AgDD expressing cells 8 h post S1 removal. (b) Large aggregate encapsulated by a single membrane (yellow arrowheads). Parts of the aggregate are sub-compartmentalized by an additional membrane (red arrowheads). The aggregate consists of an electron dense, irregularly shaped amorphous mass composed of a grainy electron density. The mass is perturbed by single and double membranes (green arrowheads) and small vesicles (asterisks). (c) Small and medium, irregularly shaped and less electron dense non-encapsulated aggregates (dashed lines). The aggregates are not surrounded by a membrane and are homogeneous in texture. ER membranes are closely associated to the aggregates. IC, ice contamination; Agg, AgDD aggregate; En, endosome; ER, endoplasmic reticulum; Mit, mitochondrion. Scale bars: (a) 2.5 µm, (b, c) 200 nm. Defocus: (a) -100 µm, (b, c) -9 µm.

As expected, cells incubated for 10 min without S1 showed small (~ 0.2 – 1 µm along the longest axis) and medium (~ 1 – 2 µm along the longest axis) sized aggregates while cells incubated for 8 h predominantly showed medium to large (over 2 µm along the longest axis) aggregates. While the percentage of membrane encapsulated to non-encapsulated aggregates at the 10 min time point was at 40% (7 cells), at the 8 h time point it was at 64% (3 cells). Additionally aggregates at the 8 h time

point were morphologically more complex, indicating that more aggregates become membrane encapsulated over time.

The observation of two structurally different aggregates which are either small, non-encapsulated but closely associated with ER, or large, encapsulated by membranes which show characteristics of autolysosomes and sub-compartmentalized by additional membranes, suggest a transition of the former into the latter. This is further reinforced by the findings that at the 10 min time point the non-encapsulated than encapsulated aggregates were more abundant, but at the 8 h time point this relation is inverted. These findings fit very well with the observations by Miyazaki et al. that multiple small aggregates coalesce into few large ones over time.

The increased co-localization with p62 over time observed by Miyazaki et al. together with our findings on the possible autolysosomal nature of the encapsulating membranes suggests the following model: after the removal of S1, AgDD quickly forms small amorphous light aggregates. These aggregates are engulfed by autophagosomes which may be derived from ER membranes (Axe et al. 2008), and later fuse with lysosomes, creating a single-membrane encapsulated autolysosome. In this time, the lysosomal hydrolytic enzymes begin to degrade the aggregates. Partial degradation could consequentially be the reason for their altered appearance. The engulfed aggregates are then transported to a central region of the cell, where they coalesce into a single large aggregate, similarly to what has been described on the formation of aggresomes (Johnston, Ward, and Kopito 1998). Aggresomes have been postulated as regions in the cell in which its proteostasis and degradation machinery is concentrated (Garcia-Mata, Gao, and Sztul 2002), and this would allow the cells to more efficiently manage the sudden occurrence of a high number of aggregates.

In conclusion, further studying the aggregation of AgDD using cryo-ET could further elucidate the mechanisms behind aggresome and autophagosome formation. Especially studying time points very shortly after the removal of S1 could be used to further study the origin of the membranes encapsulating the aggregates. The origins of autophagosomal membranes are not fully known (Rubinsztein, Shpilka, and Elazar 2012). The close association of ER membranes to some non-encapsulated aggregates in an almost cup-like shape hint toward these membranes forming a pre-autophagic structure around the aggregate. Therefore, the continued study of AgDD aggregates is of great interest.

3.3. Intracellular labeling for cryo-ET

The capability of utilizing electron dense markers in living cells without altering cellular physiology is one of the most sought after methods for *in situ* cryo-ET. Information on the molecular identity of the structures observed in situ could be highly interesting. However, vitrified samples need to be kept below temperatures of -140 °C at all times, and chemical labeling processes used in conventional EM are not possible at these cryo-temperatures. Yet identifying β-protein aggregates early via a label, for instance, could have saved months of work for the β-protein project. In order to address this problem, we tested the use of a cell-penetrating peptide called dfTAT, which has the ability to introduce extracellular cargo into the cell via endocytic processes (Erazo-Oliveras et al. 2014).

Cell penetrating peptides, especially the HIV-derived TAT, have been subject to increased research within the past years (Bechara and Sagan 2013). While the promise of being able to transduce cargo into cells in a fashion similar to the transfection of DNA is of great interest for many scientific and medical fields, finding an agent that allows this in a simple, reliable, specific and non-toxic fashion has been difficult, as numerous preclinical evaluations have shown (Guidotti, Brambilla, and Rossi 2017). Erazo-Oliveras and colleagues recently described a dimerized, fluorescent form of TAT (dfTAT) which fulfills these criteria, while also being exceptionally versatile in the type of cargo molecules which are applicable (Erazo-Oliveras et al. 2014).

dfTAT was is taken up into cells by endocytosis and subsequently escapes into the cytosol after the maturation of the endosomes into late endosomes (Erazo-Oliveras et al. 2016). However, the exact mechanism behind this endosomal leakage is not known. By inducing endosomal leakage, dfTAT is able to deliver cell-impermeable small molecules, peptides, and functional proteins into cells while inducing almost no toxicity (Erazo-Oliveras et al. 2014). In addition, in order to utilize dfTAT as a delivery agent, cargo simply needs to be co-incubated for approximately one hour with dfTAT (Najjar, Erazo-Oliveras, and Pellois 2015). After this incubation time, the efficiency of endosomal escape by dfTAT can be observed by fluorescence microscopy, as dfTAT is fluorescently marked with tetramethylrhodamine. A diffuse signal of dfTAT within the cell lumen and nucleus indicates a successful endosomal escape, while punctate cytoplasmic signals originate from dfTAT that did not leak from endosomes. Additionally, as dfTAT does not have to be bound to a specific cargo prior to transduction, multiple different cargo molecules can be delivered simultaneously or successively.

Transporting electron dense markers into living cells is not limited to the use of cell penetrating peptides such as dfTAT. Alternatively, liposomes, bacterial toxins, transfection reagents of the use of transferrin are among some of the methods also being explored for gold transduction (Levy et al. 2010). However, most of these methods are limited in their ability to not only mediate endocytosis of the desired cargo, but also allow its endosomal escape (Chithrani et al. 2010; Yang et al. 2005; Nativo, Prior, and Brust 2008).

Using dfTAT to transport gold-labeled antibodies into living cells, which could bind to β-protein aggregates, would have been an easy and elegant way of solving the β-protein aggregate identification

problem. Additionally, it has the potential to be a quick and straightforward method for the identification of many different proteins in cryo-ET projects. Therefore, we tested if we could utilize dfTAT as a transduction agent of gold-conjugated antibodies into cells prior to vitrification, in order to clearly identify proteins of interest in cryo electron tomograms.

First, experiments from Erazo-Oliveras et al. were verified using dfTAT to deliver recombinant GFP to the cell lumen of HeLa cells (**Figure 3.3-1**). Although most dfTAT and GFP was located in the cytosol after delivery, few puncta remained, indicating an efficient but incomplete delivery process.

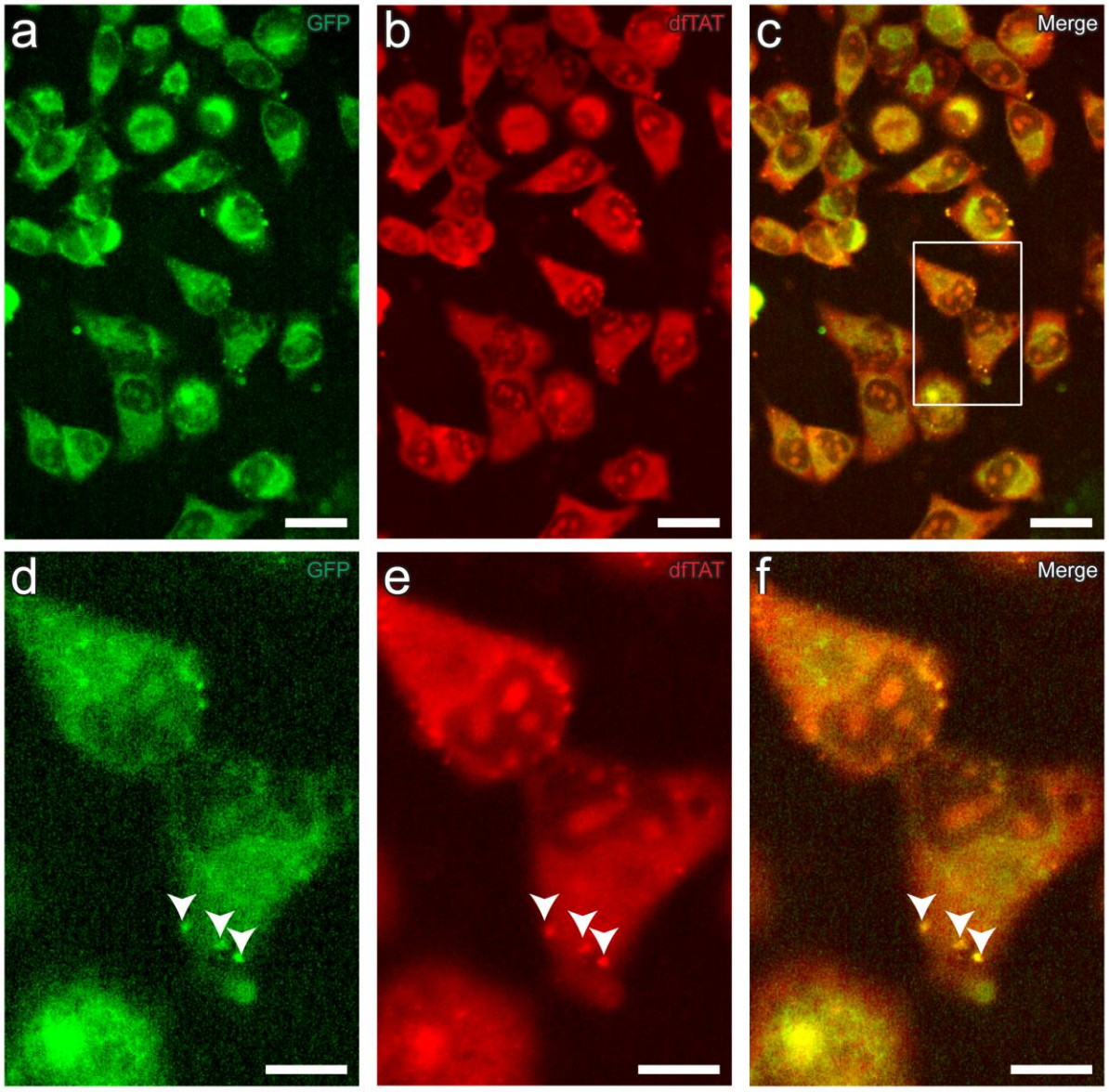

Figure 3.3-1: dfTAT mediates transport of recombinant GFP into HeLa cells. (a – c) HeLa cells co-incubated with GFP (green) (a) and dfTAT (red) (b) show that all dfTAT positive cells have incorporated GFP (merge) (c). (d – f) Magnification of area indicated in (c). Puncta (white arrowheads) fluorescent in both green (d) and red (e) indicate not all dfTAT and GFP has been released into the cytosol. Scale bars: (a – c) 25 µm, (d – f) 10 µm.

Then, we wanted to verify if dfTAT is capable of transporting antibodies into the cell by testing the transduction of FITC conjugated mitochondrial ATPase subunit α-ATP5A antibodies as reported (Erazo-Oliveras et al. 2014). However, no mitochondrial signal was observed, despite a diffuse dfTAT signal indicating correct endosomal escape (data not shown). As differences between antibody lots may affect the delivery efficiency (J.P. Pellois, personal communication), an anti-nuclear pore complex (NPC) antibody was tested instead. Using the NPC as an antibody target had the additional benefit that the NPC is easily identifiable in cryo-ET, making it a good target for later trials of gold-conjugated antibodies. Additionally, the gold labeled antibodies would have to be targeted towards a structure that is prominent enough to reproducibly target it with FIB-milling, and the nucleus of the cell fits this requirement very well. Therefore, anti-nuclear pore complex (anti-NPC) antibodies were delivered, the cells were fixed and stained with a secondary fluorescent antibody (**Figure 3.3-2 d-g**). Interestingly, dfTAT delivery of anti-NPC antibodies was highly efficient, as the staining was comparable to standard immunofluorescence (**Figure 3.3-2 a-c**), indicating not only that antibodies can be transported into cells, but that they also remain intact and functional through the process. However, the signal from unspecific antibody binding tended to be higher than in the standard immunofluorescence staining.

As a next step, the anti-NPC antibodies were conjugated to 10 nm gold particles and the experiment was repeated with these antibodies. Cells showed a diffuse cytosolic dfTAT signal, indicating the release of dfTAT molecules from the endosomes (**Figure 3.3-2 i**). However, only punctate antibody signal could be observed, indicating that gold-conjugated antibodies were indeed taken up by the cells, but not released from the endosomes (**Figure 3.3-2 h**).

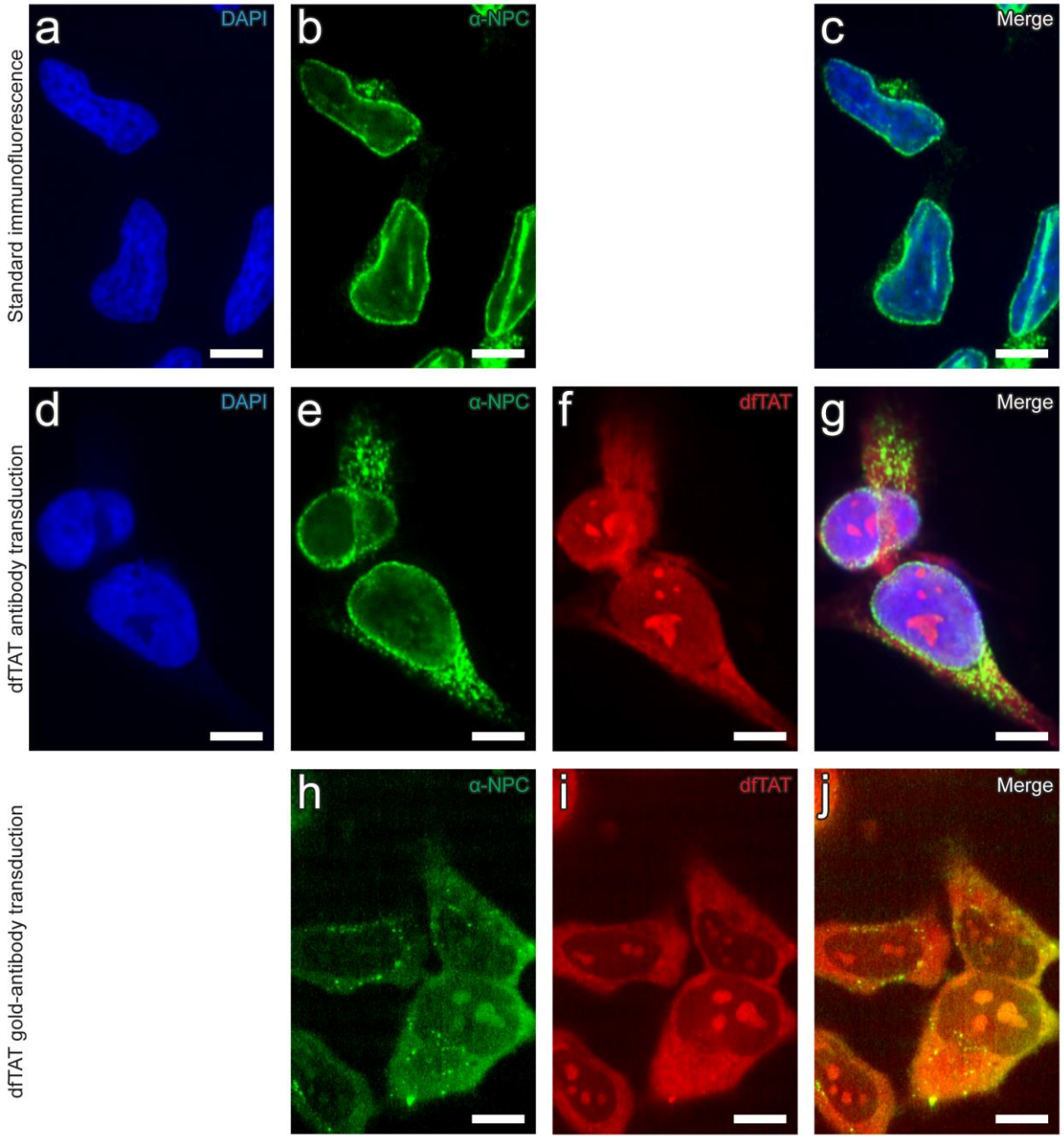

Figure 3.3-2: dfTAT mediates transport of anti-NPC antibodies into cells, but not of gold conjugated anti-NPC antibodies. (a – c) HeLa cells stained with an anti-NPC antibody (green) (b) using a standard immunofluorescence staining protocol. Nuclei counterstained with DAPI (blue) (a). (d – g) HeLa cells stained with an anti-NPC antibody (e) transported into the cells using dfTAT (red) (f). Cells were fixed after antibody transport and stained with a secondary fluorescent antibody and DAPI (d). Note the similar staining efficiency as in the standard IF protocol. (h – j) HeLa cells stained as above using a gold-conjugated anti-NPC antibody (h). DAPI staining was omitted. Although dfTAT is distributed diffusely throughout the cells, antibodies are concentrated in puncta. This indicates that although transport of dfTAT was successful, transport of gold-conjugated antibodies was stalled in the endosomes. Scale bars: 10 µm.

We then tested whether dfTAT was at all capable of transporting gold particles into the cytosol. In these experiments, cells were incubated with dfTAT together with different types of gold particles and GFP as a marker for the correct function of dfTAT. First, anti-NPC antibody conjugated gold was used for transport. Although a diffuse GFP and dfTAT signal indicated the correct function of dfTAT by cryo-

LM (data not shown), only gold situated within endo-lysosomal vesicles was observed in the resulting tomograms (**Figure 3.3-3**).

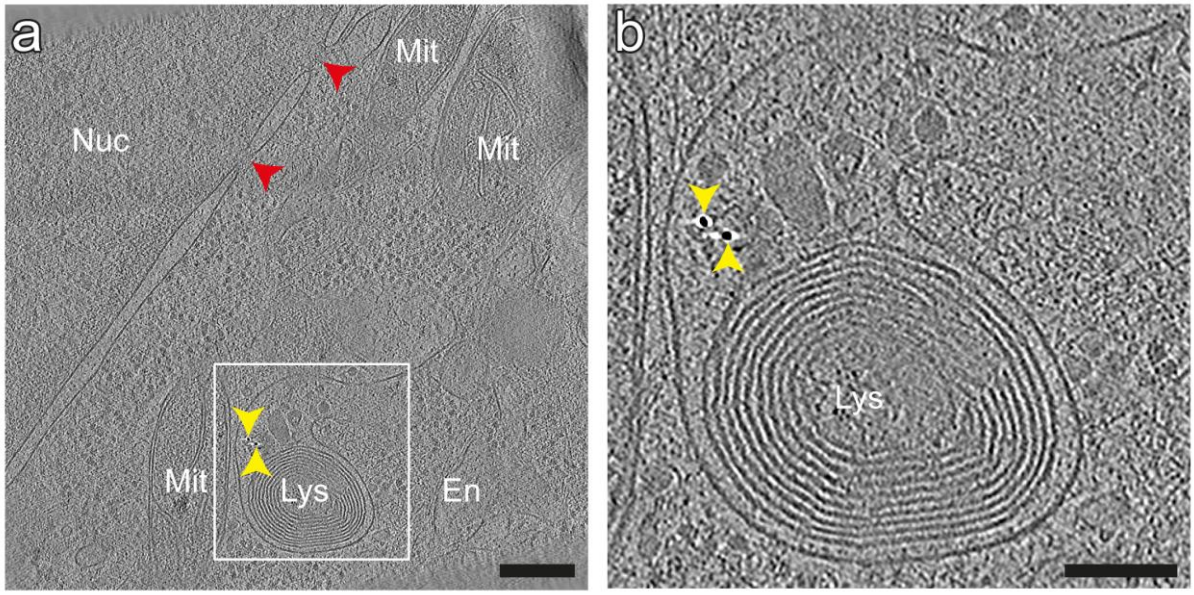

Figure 3.3-3: Gold conjugated antibodies transduced using dfTAT are retained within endolysosomal structures. (a) Tomographic slice of a HeLa cell transduced with gold conjugated anti-NPC antibodies using dfTAT. No gold particles were found in proximity to NPCs (red arrowheads) or within the cytosol. Individual gold particles are situated within lysosomes (yellow arrowheads). (b) Magnification of area indicated in (a). Two gold particles are situated within the lysosomal lumen (yellow arrowheads). En, endosome; Lys, Lysosome; Mit, mitochondrion; Nuc, Nucleus. Scale bars: (a) 200 nm, (b) 100 nm. Defocus -9 µm.

The inability of dfTATs to transport gold-conjugated antibodies could be due to multiple factors. It is possible that gold-antibody constructs are too large to cross into the cytosol during endosomal leakage. While gold particles have a diameter of 10 nm, IgG antibodies are approximately 12-14 nm in size, so the combined size of at least 22 nm might be too large for an endosomal escape. The fact that antibodies themselves are able to efficiently escape from endosomes although they are larger than 10 nm gold particles could derive from the antibodies higher flexibility. Lastly, it is likely that the surface properties of the gold particles affect their transport efficiency.

To test if the size of the gold-antibody constructs was the limiting factor for the mediation of efficient endosomal escape, unconjugated gold from an antibody conjugation kit was used for transport. Similarly to the antibody-conjugated gold, only intra-endosomal gold particles were found by cryo-ET, but no cytosolic gold particles (**Figure 3.3-4 a**). This indicated that the combined gold-antibody size was not the limiting factor in successful endosomal escape. As the surface properties of these particular gold particles might have prevented correct transport, 10 nm BSA-coated gold markers were tested next. However, as with the previous trials, no cytosolic gold particles could be found (**Figure 3.3-4 b**). Additionally, the particles found in endosomal structures were highly aggregated, forming clusters of several gold particles. As BSA-coated gold fiducial markers form aggregates when stored for long time periods, BSA coating was likely the reason for the formation of the aggregates.

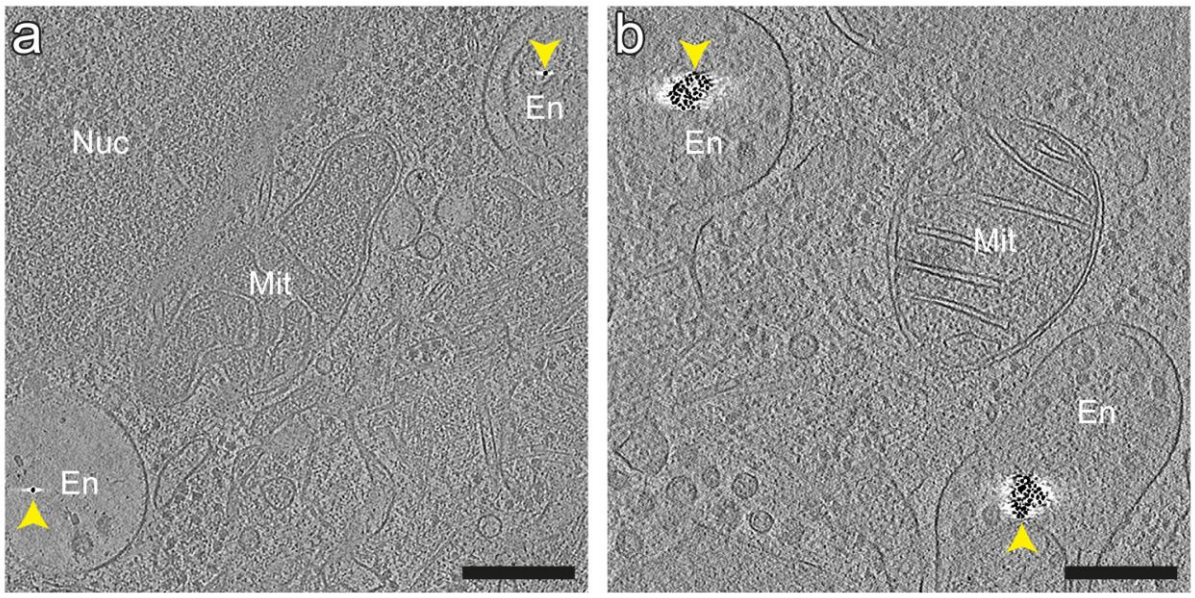

Figure 3.3-4: Unconjugated gold particles are not transduced by dfTAT. (a, b) Tomographic slices of HeLa cells transduced with innova-coat (a) and BSA coated (b) gold particles using dfTAT. Gold particles were only found within endosomes. BSA coated gold was often found in small gold particle aggregates. En, endosome; Mit, mitochondrion; Nuc, Nucleus. Scale bars: 200 nm. Defocus -9 µm.

Since similar works have shown that size in general is not necessarily the limiting factor for successful transport of cargo into cells (Li et al. 2009; Chithrani, Ghazani, and Chan 2006), testing gold particles with different surface properties would have been the most promising method to proceed. For instance, the transport of uncoated gold particles, polyethylene glycol coated gold particles or electron dense quantum dots could show higher transduction efficiencies (Liu et al. 2008; Chan and Nie 1998).

Since dfTAT has been found to not only promote the uptake of cargo by endocytosis, but efficiently allows its endosomal escape (Erazo-Oliveras et al. 2014), further research on the exact mechanism behind this endosomal escape may help to shed light on the required properties of cargo molecules. In a follow-up publication, Erazo-Oliveras and colleagues showed that dfTAT promotes the fusion of ILVs in endosomes by binding with bis(monoacylglycero)phosphate (Erazo-Oliveras et al. 2016). The subsequent release of the cargo into the cytosol might be achieved by two different mechanisms. Cargo might be translocated into the cytosol directly during these fusion events, or translocated into ILVs, followed by the fusion of the ILVs to the endosomal membrane and final release of the cargo (Erazo-Oliveras et al. 2016). In order to further understand this leakage mechanism, further cryo-ET studies could be of great use. For instance, if an electron dense marker capable of being transported by dfTAT were found, performing tomography on endosomes containing these markers would elucidate if they are indeed translocated into ILVs.

3.4. Sample vitrification via high pressure freezing

Sample freezing methods ensuring vitreous ice are vital for cryo-EM. Although plunge freezing allows the vitrification of small, monolayer cells on EM grids, larger samples such as large cells or tissues are too large to achieve optimal sample vitrification. By applying a cryoprotectant, large cells such as HeLa cells can be vitrified by plunge freezing as well. However, cryoprotectants are often toxic and can potentially alter the structure of a cell. Additionally, being able to image biological tissue samples in a near native state by cryo-EM would open up a whole new field of scientific inquiry. For instance, being able to image brain tissue from patients suffering from NDDs would enable research on these diseases directly, without the need of model systems. But even imaging tissues from animal models would be a great improvement over the use of cell systems or in vitro cultivated neurons. Since a mouse model system for β-protein aggregates is being generated, investigating tissues from these mice via cryo-ET would have been of great interest.

One vitrification method capable of achieving high enough freezing velocities for the vitrification of tissue is high-pressure freezing (HPF). In HPF, a sample is placed in a sandwich configuration within two carriers, and the space that is not occupied by the sample is filled with liquid cryoprotectant. These carriers are then placed into a holder within the high pressure freezer and are frozen with liquid nitrogen applied at very high pressures (Moor 1987). The combined low temperature and high pressure lead to high freezing velocities, allowing the vitrification of up to 600 µm thick samples (Moor 1987). HPF has been shown to successfully vitrify a wide variety of tissues (Zuber et al. 2005; Sosinsky et al. 2008; Studer, Humbel, and Chiquet 2008).

A recent publication proposed using 2-methylpentane (“pentane”) as a cryoprotectant that can be sublimated after HPF vitrification (Harapin et al. 2015). Therefore, we wanted to test if this method was applicable to our cryo-FIB/ET workflow. In short, (Harapin et al. 2015) demonstrated how *Caenorhabditis elegans* worms were vitrified on EM grids in pentane as a cryoprotectant via HPF and FIB-milled after sublimation of excess pentane under cryo conditions. By sublimating the excess pentane, the sample is covered only by a thin layer of ice comparable to a plunge-frozen sample. Therefore, standard FIB-milling protocols can be followed after sublimation.

Pentane is liquid at ambient pressure at -150 °C, and it was reported that it may be sublimated at -150 °C and high vacuum in a few minutes (Harapin et al. 2015). Since vitreous ice becomes crystalline at approximately -140 °C (Dubochet et al. 1988), these properties seemed ideal for using pentane as a cryoprotectant for HPF and easily removing excess pentane prior to further sample preparation. However, personal experience with FIB milling of plunge frozen samples has shown that samples which have been warmed to over -160 °C for long periods of time often show signs of devitrified ice. Therefore, during the separation of the carriers and our attempts to sublimate excess pentane off of HPF frozen grids, we maintained a stage temperature of -160 °C. Since the temperature is measured within the stage, and not directly on the sample, it is reasonable to assume that sample temperatures were a few degrees higher.

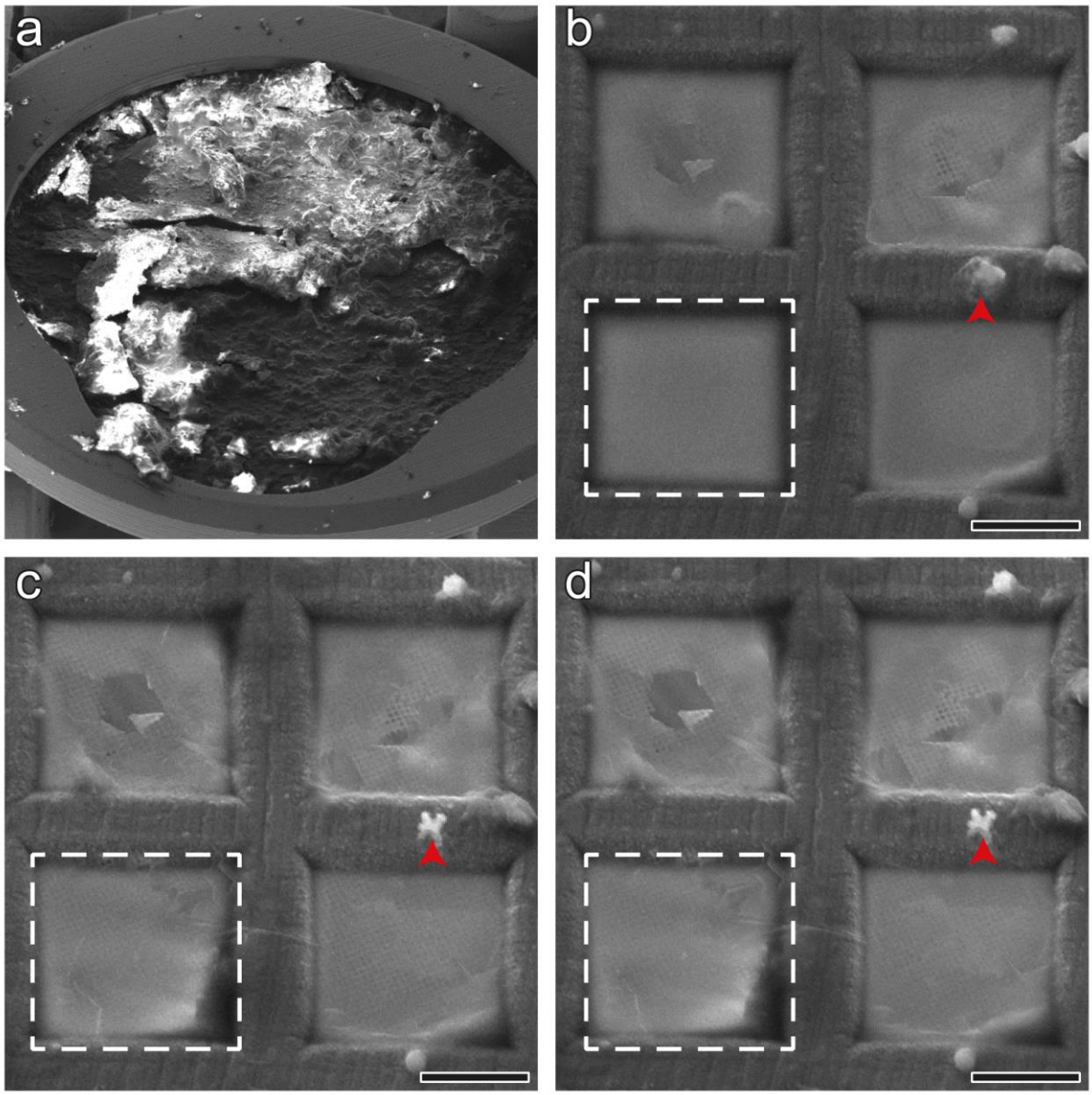

Figure 3.4-1: Pentane does not sufficiently sublimate from EM-grids at temperatures ensuring vitreous ice preservation. (a) Many grids were covered with thick frozen pentane impossible to sublimate. (b – d) Scanning electron micrographs of part of four grid squares of an HPF frozen grid covered with a layer of pentane imaged 5 (b), 15 (c) and 60 (d) min after warming to approximately -160 °C. Small amounts of pentane sublimate within the first 15 min (compare boxed region and red arrowheads in b and c). After 15 min, no significant reduction of the pentane covering the grid could be detected (compare c to d). Scale bars: 50 µm.

To be able to precisely set the temperature to -160 °C, the carriers were opened within a cryo-ultramicrotome. Opening the two HPF carrier halves while keeping the sample at approximately -160 °C proved difficult, as the pentane is almost solid at this temperature. Therefore, it was very likely that the grid was damaged by opening the carriers, and a few grids subsequently imaged in the SEM/FIB had been separated from the carbon film. Other grids were covered with a thick layer of pentane (**Figure 3.4-1 a**). To remove excess pentane, grids were blotted within the microtome using pre-cooled filter paper. Grids were then clipped in FIB Autogrid frames and transferred into the FIB Quanta SEM onto a stage cooled to -160 °C. Sample temperatures are typically a few degrees Celsius higher than the stage temperature, which should have been sufficiently warm for pentane sublimation under

vacuum. Samples were imaged at 5, 15 and 60 min after transfer onto the stage. 15 min after transfer, small amounts of pentane had sublimated (**Figure 3.4-1 a, b** red arrowheads). However, insufficient amounts of pentane were sublimated afterwards, as after 60 min the amount of pentane covering the grid was unchanged. Thus, the layer of pentane covering the sample hindered any further FIB milling.

In order to remove the excess pentane from the grids without needing to increase the sample temperature, carriers were opened in a 70% / 30% liquid ethane / propane mixture normally used for plunge freezing that had been cooled to -160 °C in the cryo-microtome chamber. After few minutes of keeping the sample in this mixture, the carriers were easily separated. Since ethane, propane and pentane are short chain alkanes, the semi-solid pentane can be dissolved within the ethane / propane mixture. Grids were washed in this mixture for approximately one minute, excess ethane / propane was blotted away and grids were then transferred to the FIB/SEM. The amount of pentane covering the sample had been significantly reduced (**Figure 3.4-2**). It was now also possible to mill the samples with standard cryo-FIB currents (**Figure 3.4-2 b**), although milling was slower than for normal plunge frozen cells. However, the samples displayed high amounts of large ice crystal contamination (**Figure 3.4-2 a** red arrowheads). As the cryo-microtome is operated at atmospheric pressure, and cooled only by nitrogen vapor, the handling of the grids within the cryo-microtome was the most likely origin of this contamination.

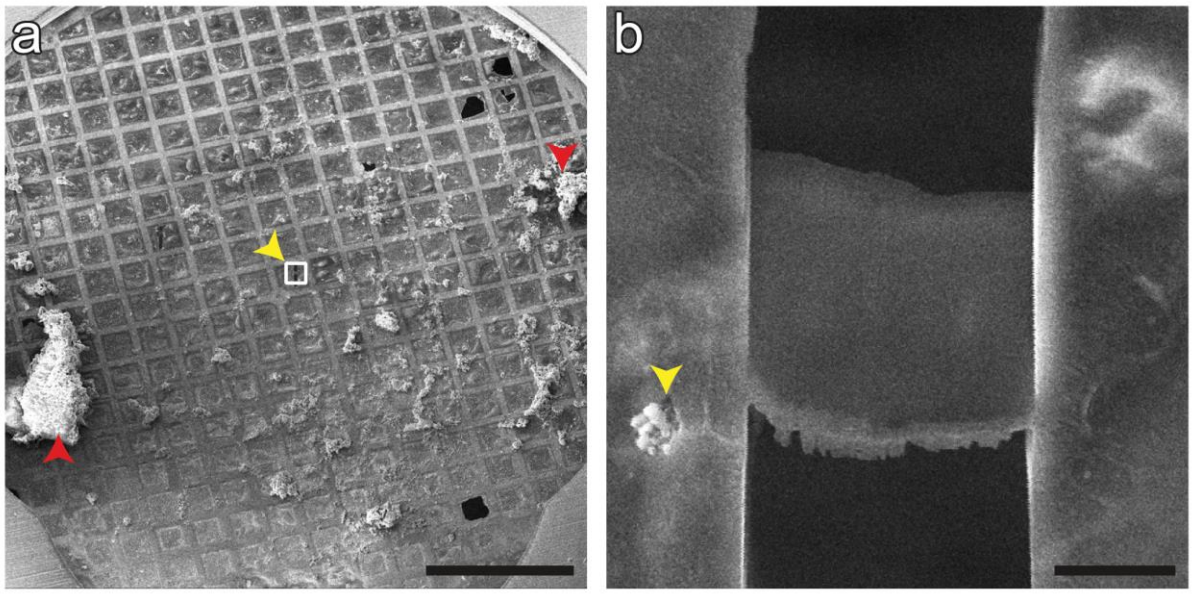

Figure 3.4-2: Grids washed in liquid ethane / propane at -160 °C show reduced pentane surface coverage. (a) Scanning electron micrograph of an HPF frozen grid washed in liquid ethane / propane. Note the high amounts of ice-crystal contamination (red arrowheads). (b) Magnification of area indicated by yellow arrowhead in (a). Amounts of residual pentane were low enough to enable FIB-milling of cells. The yellow arrowhead indicates a crevice formed by movement of the ice contamination, making the layer of residual pentane apparent. Scale bars: (a) 500 µm, (b) 5 µm.

Although the increased freezing velocity of high-pressure freezing should allow the vitrification of very thick samples, large portions of some lamellae showed signs of ice crystallization when observed by TEM, as judged by the occurrence of electron diffraction artifacts resulting from the ice crystal structure (**Figure 3.4-3**). Similarly to plunge frozen cells frozen without the addition of a

cryoprotectant, crystalline ice was often observed in the nuclei and their direct surroundings, suggesting insufficient cooling velocities.

The formation of this crystalline ice could be a consequence of multiple factors. On the one hand, handling errors during the freezing process could lead to an insufficient cooling velocity. If the carriers containing the grids are not completely filled with non-gaseous material, the cooling velocity will be significantly reduced (Moor 1987). Since pentane is very volatile, the occurrence of gas pockets within the carrier is likely. On the other hand, carriers were placed in liquid ethane / propane in the microtome set to -160 °C for a few minutes to dissolve the pentane. Since this temperature is not measured within the liquid, it may have been high enough to partially devitrify the sample or the sample may have been subjected to too high temperatures for too long. With caution, it is possible to distinguish both modes of crystalline ice formation by their localization: crystalline ice localized in the center of the cell hints towards an insufficient cooling velocity, while homogeneously distributed ice crystals suggest devitrification. As ice crystals were primarily centrally localized, it is likely they were formed during freezing.

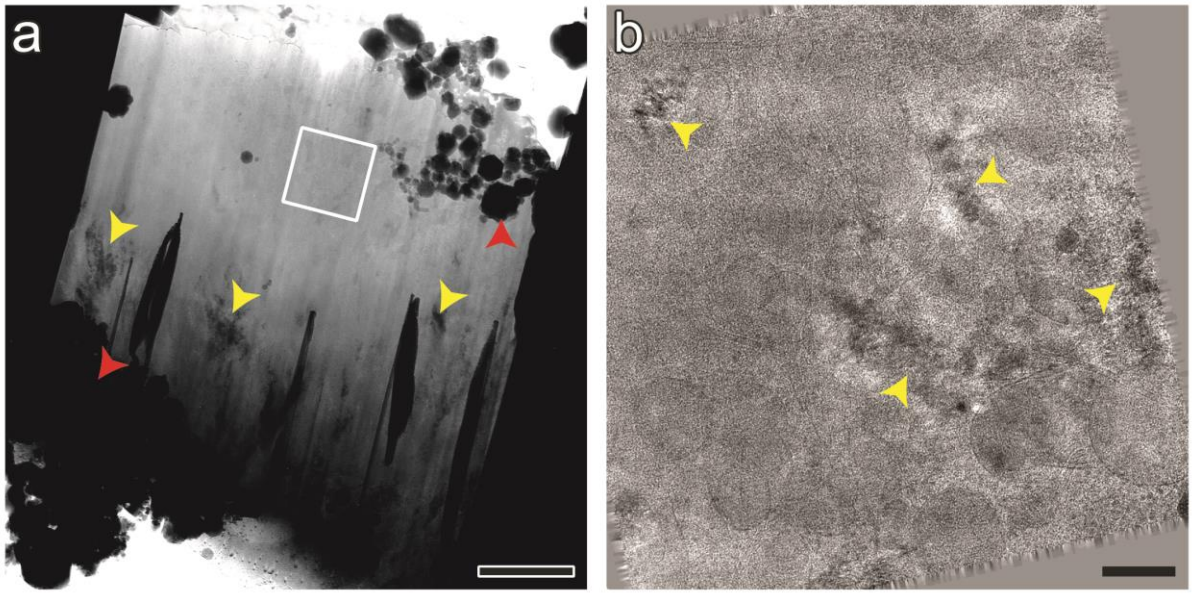

Figure 3.4-3: HeLa cells frozen via HPF show signs of crystalline ice. (a) TEM overview image of a lamella from a HeLa cell. Crystalline ice within the lamella can be detected by the occurrence of image artifacts (yellow arrowheads). Note the large amounts of ice contamination (red arrowheads). (b) Single tilt from a tilt-series acquired in the region indicated in (a). High amounts of image artifacts (yellow arrowheads) throughout the tilt-series indicate crystalline ice. Scale bars: (a) 2.5 µm, (b) 200 nm. Defocus: (a) -100 µm, (b) -9 µm.

In addition to the crystalline ice, many grids showed signs of mechanical stress (**Figure 3.4-4**). The surface of some grids was very flat with shallow indentations in the form of ring-shaped lines resembling the surface of the carrier lid (**Figure 3.4-4 a**, dashed box). Cells on these grids were either squashed if located on top of grid bars, or pushed downwards together with the surrounding carbon support. These grids must have been pressed against the carrier lid during freezing. This could either be due to them being clamped between the carrier halves or possibly by electrostatic forces pushing them towards the lid before freezing.

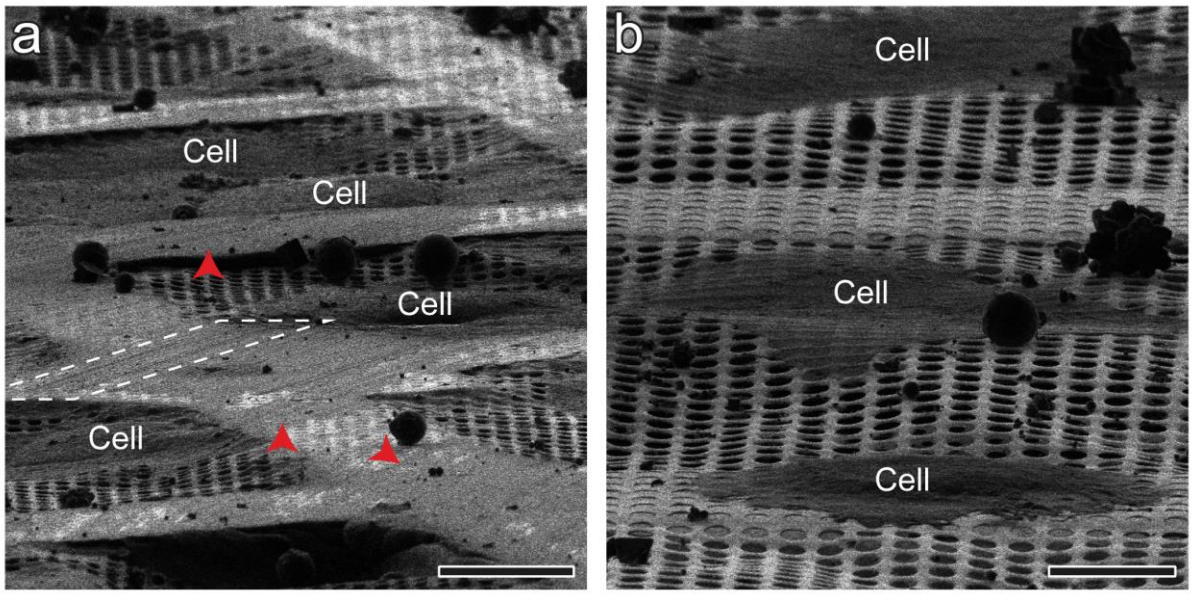

Figure 3.4-4: Cells on high pressure frozen grids may be squashed or devoid of cell internal material. (a, b) Focused ion beam micrographs of HPF frozen grids acquired at 18° inclination. (a) Some grids were forced against the HPF carrier lid, squashing cells attached to the grid bars (red arrowheads) and depressing the carbon support together with the cells within grid squares. Notice the relief imprinted on to the squashed cells, in part indicated by the dashed box. (b) Cells on some HPF frozen grids were devoid of interior cellular material, leaving thin membrane husks. Scale bars: (a) 20 µm, (b) 10 µm

Other grids showed very flat remnants of cells attached to the carbon support (**Figure 3.4-4 b**). Although EGFP signal from these cells was observable by cryo-LM, only flat membrane husks could be found by FIB/SEM. As these cell remnants were too flat for FIB milling, no further investigation by TEM was possible. Coincidentally, the carbon support on these grids contained virtually no ice, indicating that the grids were blotted for too long.

Too long blotting might have removed the water within and around the cells. However, to achieve such dry grids via plunge-freezing the grids would need to be blotted significantly longer. Otherwise, this issue could be related to the application of pentane, or a combination of both. As pentane is extremely hydrophobic, it is possible that pentane displaces the water on the surface of the grid. The resulting osmotic pressure within the cells from the lack of water around them could then lead to their very quick dehydration, leaving only the membrane attached to the carbon. Additionally, pentane is toxic to cells and could lead to a form of “leakage” of cytoplasm from the cell. Potential toxicity effects could also be observed in some cells, as they showed a very high amount of vesicles within the lumen (**Figure 3.4-5 b**).

Lastly, many lamellae showed large cracks and bubbles (**Figure 3.4-5**). Tomograms taken in these regions revealed holes within the lamellae (**Figure 3.4-5 b**). The cracks could be most frequently observed along membranes. These kind of artifacts have been reported in the past to be effects of the high pressure that is applied before freezing (Craig and Staehelin 1988).

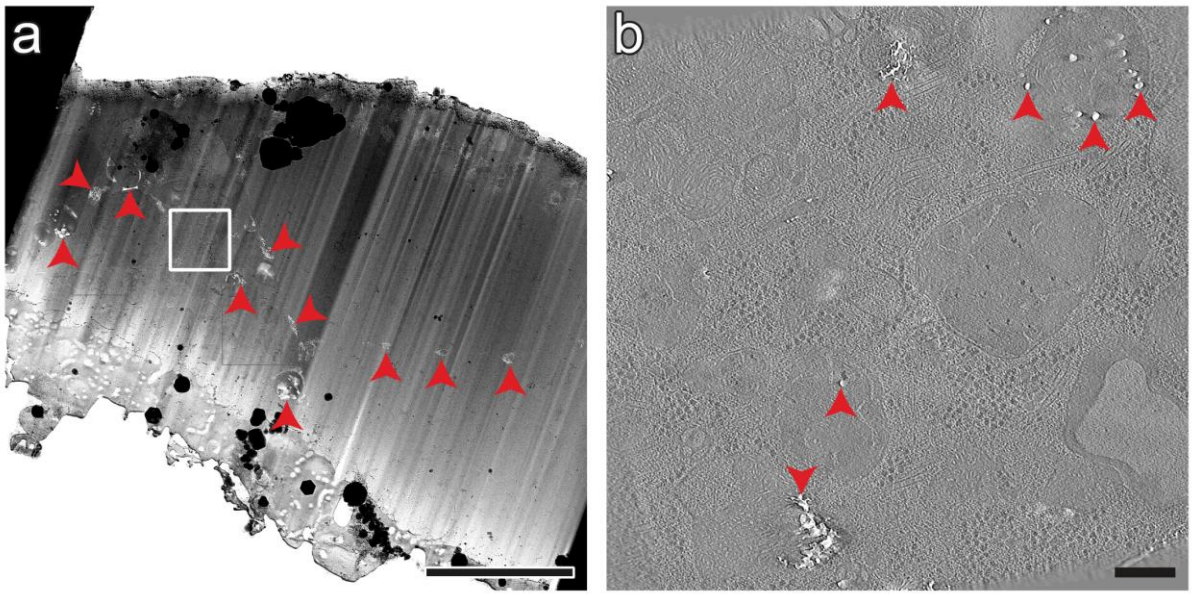

Figure 3.4-5: Cells frozen via HPF in pentane often show cracks and bubbles devoid of cellular material. (a) TEM overview image of a lamella from an HPF frozen cell. (b) Tomographic slice of area indicated in (a). (a and b) Multiple regions show cracks and bubbles (red arrowheads), especially along membranes and in vesicles. Scale bars: (a) 5 µm, (b) 200 nm. Defocus: (a) -100 µm, (b) -6 µm

The large cracks and bubbles observed in many lamellae could be due to the pentane's toxicity and volatility. Since pentane is hydrophobic and relatively neutral in charge, it is possible that large amounts of pentane are taken up by the cell, where it may then expand due to its low vapor pressure, forming gaseous bubbles. The localization of these cracks primarily along membranes could be due to the hydrophobic pentane being incorporated on these membranes (Craig and Staehelin 1988). This uptake of pentane may also lead to the flattened cells described above, if the expansion of the pentane ruptures the cell membrane before vitrification. This intracellular pentane might also be the reason for the increased time and ion currents needed to mill the lamellae. As previously described, pentane requires higher currents for an acceptable milling speed.

In conclusion, HPF of mammalian cells on EM grids using pentane as a cryoprotectant showed a lot of issues and requires more experience and optimization. It is quite likely that our limited access to the HPF machine and our very limited experience with HPF lead to increased issues with this technique. But freezing tissue samples with HPF using pentane could be a valid solution, as the toxic effects of pentane might be less pronounced in cells deeply embedded in tissues, as these cells would have less time to come into contact with this toxic chemical. Recently, the method of cryo-lift out of thin slices from large HPF frozen samples has however been significantly improved (Mahamid et al. 2015). As this method does not rely on a toxic cryoprotectant, lift out and later preparation of lamellae from HPF frozen tissue could be a more practical solution for cryo-ET imaging of large vitreous specimen.

4. Discussion

This section only discusses the results of the main project on β-protein aggregates. The results of the side projects are discussed within their respective sub-sections.

4.1. β-protein aggregation

Protein aggregation is a hallmark of NDDs and studying the causes and effects of these aggregates is of great interest in order to find treatments for these diseases. Yet the effects of protein aggregation on the cell are extremely heterogeneous and complex. In order to better understand protein aggregation in disease, it is useful to simplify the question of how protein aggregation affects cells by breaking it down into gain and loss of function toxicity. Therefore, in this work the structural and functional effects of protein aggregation by toxic gain of function of model β-sheet proteins were studied.

Similar to the findings of (Olzscha et al. 2011) reporting that β-proteins form cytoplasmic aggregates in HEK293 cells, β-protein aggregates formed in HeLa cells and neurons quickly after the beginning of β-protein expression. Multiple aggregate puncta combined with the very irregular shape suggests that β-protein aggregates formed in multiple areas of the cell simultaneously and were subsequently moved to a central aggregation area, where they were combined into larger and irregularly formed aggregate. This central aggregation, often located in the perinuclear region and, in the case of aggregation in HeLa cells, often surrounded by a network of vimentin collapsed onto the aggregate, are properties of aggresomes (Garcia-Mata et al. 1999). In this regard β-protein aggregates share similarities with previously described cystic fibrosis transmembrane conductance regulator (CFTR) aggregates forming aggresomes (Johnston, Ward, and Kopito 1998) and contrast with α-synuclein aggregates which form aggresome-like inclusions but do not rearrange the vimentin network (Lee et al. 2002). Interestingly, similarly to CFTR and cytosolic protein chimera (GFP-250) aggregates (Garcia-Mata et al. 1999), β-protein aggregates also seem to be sub-composed of small aggregate units, but dissimilarly they do not converge into a near spherical shape. As CFTR aggregates have been reported to be translocated to the microtubule organizing center via microtubules, but no increased microtubule amounts or the presence of the microtubule organizing center were detected in the vicinity of β-protein aggregates by cryo-ET, it is possible that the mechanism for microtubule mediated aggregate transport applies less for β-protein aggregates. This might lead to the overall irregular β-protein aggregate structure. As vimentin filament bundles were found in conjunction with small aggregates, it is possible that aggregates are transported along these filaments towards the aggresome. Similar findings have been reported as high temperature requirement A1 (HtrA1), a

protein implicated to be involved in age-related macular degeneration, is transported along vimentin bundles towards the aggresome (Gerhardt et al. 2017).

In contrast, the lack of association of β-protein aggregates to intermediate filaments in neurons and therefore the reduction of transport could explain why neuronal β-protein aggregates are often more dispersed within the cell body. The higher dispersal of β-protein aggregates could further result in the different relative toxicity of β4 and β23 observed in neurons. β23 may be inherently more toxic than β4, as seen in non-neuronal cells (Olzscha et al. 2011). However, as β4 is less aggregation prone, the reduced concentration of these aggregates in an aggresome by the cell itself could lead to higher surface areas of β4 aggregates than β23 aggregates. This increased surface area would provide greater areas of interaction with cellular components, therefore increasing toxic effects such as protein sequestration.

The irregularly shaped β-protein aggregates were different from neurodegeneration-related aggregates that have been imaged *in situ* in unstained fully hydrated cells, such as polyQ-expanded huntingtin exon I aggregates (Bauerlein et al. 2017). Here one central aggregate forms and grows over time, indicated by the single spherical aggregate visible via FLM and the radial alignment of polyQ fibrils (Bauerlein et al. 2017). β-protein aggregates were additionally different in their structure from previously described neurodegenerative aggregates as they were comprised of a random sponge-like network of 3-4 nm thin fibrils. These fibrils differ substantially from the polyQ case, where the fibrils are roughly twice in thickness with approximately 7-8 nm diameter (Bauerlein et al. 2017), as well as from C9orf72 poly-GA aggregates, which are composed of 13-15 nm thick ribbons (Guo, Lehmer, et al. 2018).

While polyQ aggregates show very low numbers of internal large macromolecules, poly-GA aggregates contain a high concentration of 26s proteasomes. β-protein aggregates, on the other hand, fall in an intermediate category, as ribosomes were found within their core with concentrations rising towards the outer aggregate boundaries. The positioning of intra-aggregate ribosomes in a polysome-like fashion suggests that ribosomes embedded within aggregates might still be translationally active. As previously mentioned, the presence of translationally active ribosomes embedded within the aggregates would explain why newly synthesized proteins interact with aggregates (Olzscha et al. 2011). It was shown that while proteins sequestered by β23 aggregates which were synthesized prior to β23-transfection are enriched in intrinsically unstructured regions, newly synthesized co-aggregating proteins are lower in disorder and hydrophobicity but larger in size (Olzscha et al. 2011). In addition, active aggregate embedded ribosomes might indicate that β-protein aggregates, in contrast to polyQ inclusions, do not only grow at the outer boundary, but also from within the aggregate. Interestingly, it was shown that β-protein expression leads to the inhibition of the cytosolic stress response, and by externally inducing components of this cytosolic stress response, β-protein toxicity could be partially mediated (Olzscha et al. 2011). This inhibition could in part explain the lack of proteasomal recruitment to the aggregates, and is in contrast to the dense accumulation of proteasomes in the vicinity of poly-GA aggregates which likely disrupt the UPS through proteasome sequestration and therefore depletion within the cell (Guo, Lehmer, et al. 2018).

Although β-protein aggregates were closely associated with both ER membranes and mitochondria, and fibrils interacted with their membranes similarly to polyQ filaments, β-protein fibrils did not seem to disrupt membrane integrity as polyQ fibrils do (Bauerlein et al. 2017). This could be due to possible higher membrane interaction forces induced by polyQ fibrils and their much higher stiffness than that of β-protein fibrils. As β-protein fibrils are arranged in a tightly interwoven network, they are likely to be very flexible. Thus, β-protein fibrils may not be stiff enough to produce force on the membranes. The lower strength in interaction of β-protein fibrils compared to polyQ fibrils would explain how, although β-protein aggregates are similarly closely associated to the ER, the membranes are not anchored to the aggregate and therefore no abnormally high amounts of ER in the direct aggregate proximity are accumulated. The close association of the ER to the aggregates, especially in light of the aggregate localization in an aggresome-like fashion, could suggest the involvement of the ER associated protein degradation in the attempts to concentrate proteostasis efforts, as has previously been reported (Kaganovich, Kopito, and Frydman 2008).

In turn, ER and mitochondria very frequently formed MCS in direct proximity to the aggregates, as observed by cryo-ET. It has previously been shown that increased ER-stress in the context of the unfolded protein response is linked to the stability of ER-mitochondria MCS (Verfaillie et al. 2012) and alterations in ER-mitochondria MCS have frequently been observed in numerous NDDs such as AD, PD and ALS (Cali et al. 2012; Area-Gomez et al. 2012; Stoica et al. 2014). Additionally, the MMP was reduced in cells expressing β-proteins. As Ca^{2+} uptake and therefore Ca^{2+} signaling is directly dependent on the MMP (Rottenberg and Scarpa 1974), this MMP decrease suggests a disruption in MCS Ca^{2+} transfer. Functional Ca^{2+} signaling, especially at MCS, is a crucial prerequisite for the synthesis of ATP (Duchen 1992) and decreased cellular ATP levels may contribute to progress protein aggregation (Pathak, Berthet, and Nakamura 2013). In addition, the dysfunction of mitochondria has been shown to initiate the formation of α-synuclein aggregates in the context of PD (Lee et al. 2002). In this light, it is possible that β-protein aggregates impair mitochondrial function, which in turn decreases the cell's ability to clear aggregates and hinder further aggregation.

Interestingly, MCS between mitochondria and ER have also been suggested as regions of autophagosome formation (Hamasaki et al. 2013). Additionally, it has been shown that autophagy initiating proteins are recruited to sites of aggregation in PD and HD models (Iwata et al. 2005). Autophagy is another process often disturbed in NDDs (Menzies et al. 2017), and lysosomal function is often impaired in these diseases (Nixon 2013; Wang et al. 2018). Although increased numbers of pre-autophagic structures and autophagosomes in β-protein expressing cells were not observed by cryo-ET, mature lysosomal structures were significantly enlarged and filled with cargo. Additionally, early autophagosomal markers were stable, but autolysosomal markers and lysosomal gene transcription were increased. These effects imply an impairment in the lysosome's ability to degrade their cargo, not in the initiation of autophagy itself. The upregulation of lysosomal ATPase subunits and cathepsins fits well with the observation that lysosomes in β-protein expressing neurons show a decreased acidity. Thus, to try to maintain the integrity of lysosomal function, the cells may upregulate proteins which, under normal circumstances, should increase lysosomal function. As cells show this effort in increasing

lysosomal function, but in turn were demonstrating lysosomal impairment, the cause of this impairment most likely roots to an intermediate step in the lysosomal system.

Similar forms of lysosomal dysfunction are common not only in NDDs, but also a group of diseases termed lysosomal storage diseases (LSDs) (Aflaki, Westbroek, and Sidransky 2017). These are diseases characterized by a form of functional impairment of the lysosomes leading to an accumulation of lysosomes, which in turn accumulate undegraded substrates very similarly to cells expressing β-proteins (Platt 2014). For instance, in diseases such as mucolipidosis, Niemann-Pick disease or Fabry disease, multilamellar endolysosomal structures with striking similarity to those found in β-protein expressing cells are observed (Skikne, Prinsloo, and Webster 1972; Kohn et al. 1977; Alroy, Sabnis, and Kopp 2002). These multilamellar endolysosomal structures have also been identified in brain tissue from AD patients (Nixon et al. 2005). Furthermore, LSDs possess many similarities to NDDs in their cellular effects and underlying causes. For example, the LSD Gaucher disease derives from mutations in the glucocerebrosidase gene, which have also been found to be common risk factors for PD (Robak et al. 2017). Additionally, approximately two thirds of LSDs result in neurological deficiencies (Boustany 2013). These similarities between NDDs and LSDs in the context of our observations of lysosomal dysfunction by β-protein aggregates reinforce the idea that lysosomal dysfunction is a common feature in many human diseases.

Toxicity generated through protein sequestration has been observed in many NDD models (Kim et al. 2016; May et al. 2014; Olzscha et al. 2011; Park et al. 2013; Woerner et al. 2016). Especially the sequestration of proteins responsible for protein homeostasis simultaneously increases the toxicity load on the cell while reducing its capability of coping with further protein aggregation (Olzscha et al. 2011; Park et al. 2013). In a sense, this dysfunction is due to similar effects as in LSDs (Aflaki, Westbroek, and Sidransky 2017): if crucial proteins of the lysosomal system are essentially removed from the cytosol by sequestration, proteins downstream may not be able to perform their function.

The lysosomal dysfunction in β-protein expressing cells may be directly caused by the sequestration of AP-3 µ3A. Five AP complexes (AP-1 - 5) are currently known. They are heterotetrameric complexes consisting of four different subunits called adaptins: two large adaptins (one γ, α, δ, ε or ζ and one β1-5), one medium adaptin (µ1-5) and one small adaptin (σ1-5) (Boehm and Bonifacino 2001). Some adaptins possess two isoforms. For instance AP-3 µ3A is expressed ubiquitously while AP-3 µ3B is only expressed in neurons and neuroendocrine cells (Boehm and Bonifacino 2001). AP complexes are involved in the formation of coated vesicles and the selection of cargo within the secretory, endocytic and lysosomal pathways (Boehm and Bonifacino 2001). AP-3 is responsible for the transport of lysosomal membrane proteins such as CD63, LAMP-1, and LAMP-2 from the Golgi and early endosomal system to the lysosomes (Peden et al. 2004), and AP-3 deficiency results in lysosomal membrane protein mislocalization to the plasma membrane (Yang et al. 2000; Dell'Angelica et al. 1999). Interestingly, specifically AP-3 µ3A has been found to interact with protein sequences characteristic of lysosomal targeting signals (Ohno et al. 1998), reinforcing the notion that AP-3 µ3A sequestration may lead to lysosomal dysfunction. Dysfunctional AP-3 has been previously identified to induce Hermansky-Pudlak syndrome (HPS) type 2 (Clark et al. 2003), an LSD leading to pigmentation and bleeding

disorders (Huizing, Anikster, and Gahl 2000), but also neurological symptoms such as epilepsy and hyperactivity (Kantheti et al. 1998; Nakatsu et al. 2004). Interestingly, in cells from Pearl mice, an HPS mouse model lacking the AP-3 β3A subunit, lysosomes are filled with multilamellar membrane sheets reminiscent to those observed in β-protein-expressing neurons (Zhen et al. 1999; Nakatani et al. 2000). AP-3 subunits, especially AP-3 μ3A, are also sequestered in AD and HD model systems (Kim et al. 2016; Hosp et al. 2017). These findings suggest that lysosomal impairment in NDDs may be due, at least in part, to the sequestration of critical components of the pathway within protein aggregates, and thus to the toxic gain-of-function of the aggregated proteins.

One reason for the specific sequestration of AP-3 μ3A could be the occurrence of an immunoglobulin-like β-sandwich fold at its C-terminal domain (Mardones et al. 2013). This β-sandwich consists of 16 strands of β-sheets and contains a tyrosine-based YXXØ recognition site (Mardones et al. 2013). YXXØ sorting signals have been found among other functions, to mediate endosomal and lysosomal targeting (Guarnieri et al. 1993; Collawn et al. 1990). As this YXXØ recognition site is hydrophobic (Mardones et al. 2013), it may induce an interaction with β-proteins (Olzscha et al. 2011). The β-sandwich could then be bound by the amyloidogenic β-sheets of the β-protein aggregates and therefore sequester the AP-3 μ3A subunit.

In addition to AP-3 subunits, aggregates in NDD models for HD and AD have also been reported to sequester subunits of other AP complexes such as AP-1, AP-2 (Hosp et al. 2017; Kim et al. 2016; Olzscha et al. 2011). Similarly to AP-3 μ3A sequestration, the sequestration of other adaptins may have a profound effect on the functionality of the secretory, endosomal or lysosomal system. For instance, AP-2 has been found to play an essential role in the retrograde transport of brain-derived neurotrophic factor activated TrkB receptors, and knock out of the AP-2 μ subunit leads to neuronal loss and neurodegeneration in mice (Kononenko et al. 2017). Furthermore, mutations in the AP-4 σ and AP-5 ζ subunits have been found to cause hereditary spastic paraplegia, a progressive gait disorder resulting from the impairment of axons in the spinal cord (Słabicki et al. 2010; Hardies et al. 2015).

As the aggregation of artificial β-proteins excludes the possibility of lysosomal impairment to be derived from a loss of function toxicity effect, our findings imply that lysosomal dysfunction in NDDs is in part a toxic gain of function effect generated by protein aggregation. In the light of impaired autophagy being closely associated with the progression of NDDs, boosting lysosomal degradation might be a promising mechanism for therapeutic treatment of NDDs (Wang et al. 2018). While the underlying reasons for protein aggregation may not be ameliorated through the increase of autophagy and lysosomal degradation, the ability of cells to cope with protein aggregation could be increased enough to reduce the devastating effects of NDDs. As autophagy is a highly complex process, restoring the functionality specifically of those proteins impaired or sequestered in each particular disease could suffice to reduce the effects of NDDs (Aflaki et al. 2016; Xiao et al. 2015; Mazzulli, Zunke, Tsunemi, et al. 2016).

5. References

Aflaki, E., D. K. Borger, N. Moaven, B. K. Stubblefield, S. A. Rogers, S. Patnaik, F. J. Schoenen, W. Westbroek, W. Zheng, P. Sullivan, H. Fujiwara, R. Sidhu, Z. M. Khaliq, G. J. Lopez, D. S. Goldstein, D. S. Ory, J. Marugan, and E. Sidransky. 2016. 'A New Glucocerebrosidase Chaperone Reduces alpha-Synuclein and Glycolipid Levels in iPSC-Derived Dopaminergic Neurons from Patients with Gaucher Disease and Parkinsonism', *J Neurosci*, 36: 7441-52.

Aflaki, E., W. Westbroek, and E. Sidransky. 2017. 'The Complicated Relationship between Gaucher Disease and Parkinsonism: Insights from a Rare Disease', *Neuron*, 93: 737-46.

Al-Amoudi, A., J. J. Chang, A. Leforestier, A. McDowall, L. M. Salamin, L. P. Norlen, K. Richter, N. S. Blanc, D. Studer, and J. Dubochet. 2004. 'Cryo-electron microscopy of vitreous sections', *Embo j*, 23: 3583-8.

Alroy, J., S. Sabnis, and J. B. Kopp. 2002. 'Renal pathology in Fabry disease', *J Am Soc Nephrol*, 13 Suppl 2: S134-8.

Area-Gomez, E., M. Del Carmen Lara Castillo, M. D. Tambini, C. Guardia-Laguarta, A. J. de Groof, M. Madra, J. Ikenouchi, M. Umeda, T. D. Bird, S. L. Sturley, and E. A. Schon. 2012. 'Upregulated function of mitochondria-associated ER membranes in Alzheimer disease', *Embo j*, 31: 4106-23.

Arnold, J., J. Mahamid, V. Lucic, A. de Marco, J. J. Fernandez, T. Laugks, T. Mayer, A. A. Hyman, W. Baumeister, and J. M. Plitzko. 2016. 'Site-Specific Cryo-focused Ion Beam Sample Preparation Guided by 3D Correlative Microscopy', *Biophys J*, 110: 860-9.

Axe, E. L., S. A. Walker, M. Manifava, P. Chandra, H. L. Roderick, A. Habermann, G. Griffiths, and N. T. Ktistakis. 2008. 'Autophagosome formation from membrane compartments enriched in phosphatidylinositol 3-phosphate and dynamically connected to the endoplasmic reticulum', *J Cell Biol*, 182: 685-701.

Baker, Lindsay A., and John L. Rubinstein. 2010. 'Chapter Fifteen - Radiation Damage in Electron Cryomicroscopy.' in Grant J. Jensen (ed.), *Methods Enzymol* (Academic Press).

Banaszynski, L. A., L. C. Chen, L. A. Maynard-Smith, A. G. Ooi, and T. J. Wandless. 2006. 'A rapid, reversible, and tunable method to regulate protein function in living cells using synthetic small molecules', *Cell*, 126: 995-1004.

Bauerlein, F. J. B., I. Saha, A. Mishra, M. Kalemanov, A. Martinez-Sanchez, R. Klein, I. Dudanova, M. S. Hipp, F. U. Hartl, W. Baumeister, and R. Fernandez-Busnadiego. 2017. 'In Situ Architecture and Cellular Interactions of PolyQ Inclusions', *Cell*, 171: 179-87 e10.

Beart, P., M. Robinson, M. Rattray, and N.J. Maragakis. 2017. *Neurodegenerative Diseases: Pathology, Mechanisms, and Potential Therapeutic Targets* (Springer International Publishing).

Bechara, C., and S. Sagan. 2013. 'Cell-penetrating peptides: 20 years later, where do we stand?', *FEBS Lett*, 587: 1693-702.

Belanger, M., and P. J. Magistretti. 2009. 'The role of astroglia in neuroprotection', *Dialogues Clin Neurosci*, 11: 281-95.

Bence, N. F., R. M. Sampat, and R. R. Kopito. 2001. 'Impairment of the ubiquitin-proteasome system by protein aggregation', *Science*, 292: 1552-5.

Blokhuis, A. M., E. J. Groen, M. Koppers, L. H. van den Berg, and R. J. Pasterkamp. 2013. 'Protein aggregation in amyotrophic lateral sclerosis', *Acta Neuropathol*, 125: 777-94.

Boehm, M., and J. S. Bonifacino. 2001. 'Adaptins: the final recount', *Mol Biol Cell*, 12: 2907-20.

Booth, Christopher, and Paul Mooney. 2013. 'Applications of electron-counting direct-detection cameras in high-resolution cryo-electron microscopy', *Microsc. Anal*, 27: 13-21.

Boustany, R. M. 2013. 'Lysosomal storage diseases--the horizon expands', *Nat Rev Neurol*, 9: 583-98.

Bravo, R., J. V. Small, S. J. Fey, P. M. Larsen, and J. E. Celis. 1982. 'Architecture and polypeptide composition of HeLa cytoskeletons. Modification of cytoarchitectural polypeptides during mitosis', *J Mol Biol*, 154: 121-43.

Bright, N. A., L. J. Davis, and J. P. Luzio. 2016. 'Endolysosomes Are the Principal Intracellular Sites of Acid Hydrolase Activity', *Curr Biol*, 26: 2233-45.

Cali, T., D. Ottolini, A. Negro, and M. Brini. 2012. 'alpha-Synuclein controls mitochondrial calcium homeostasis by enhancing endoplasmic reticulum-mitochondria interactions', *J Biol Chem*, 287: 17914-29.

Chan, Warren C. W., and Shuming Nie. 1998. 'Quantum Dot Bioconjugates for Ultrasensitive Nonisotopic Detection', *Science*, 281: 2016-18.

Chithrani, B Devika, Arezou A Ghazani, and Warren CW Chan. 2006. 'Determining the size and shape dependence of gold nanoparticle uptake into mammalian cells', *Nano letters*, 6: 662-68.

Chithrani, D. B., M. Dunne, J. Stewart, C. Allen, and D. A. Jaffray. 2010. 'Cellular uptake and transport of gold nanoparticles incorporated in a liposomal carrier', *Nanomedicine*, 6: 161-9.

Chiti, F., and C. M. Dobson. 2017. 'Protein Misfolding, Amyloid Formation, and Human Disease: A Summary of Progress Over the Last Decade', *Annu Rev Biochem*, 86: 27-68.

Chitnis, T., and H. L. Weiner. 2017. 'CNS inflammation and neurodegeneration', *J Clin Invest*, 127: 3577-87.

Clark, R. H., J. C. Stinchcombe, A. Day, E. Blott, S. Booth, G. Bossi, T. Hamblin, E. G. Davies, and G. M. Griffiths. 2003. 'Adaptor protein 3-dependent microtubule-mediated movement of lytic granules to the immunological synapse', *Nat Immunol*, 4: 1111-20.

Collawn, J. F., M. Stangel, L. A. Kuhn, V. Esekogwu, S. Q. Jing, I. S. Trowbridge, and J. A. Tainer. 1990. 'Transferrin Receptor Internalization Sequence Yxrf Implicates a Tight Turn as the Structural Recognition Motif for Endocytosis', *Cell*, 63: 1061-72.

Cowles, C. R., G. Odorizzi, G. S. Payne, and S. D. Emr. 1997. 'The AP-3 adaptor complex is essential for cargo-selective transport to the yeast vacuole', *Cell*, 91: 109-18.

Craig, S., and L. A. Staehelin. 1988. 'High pressure freezing of intact plant tissues. Evaluation and characterization of novel features of the endoplasmic reticulum and associated membrane systems', *European journal of cell biology*, 46: 81-93.

Csordás, György, Christian Renken, Péter Várnai, Ludivine Walter, David Weaver, Karolyn F. Buttle, Tamás Balla, Carmen A. Mannella, and György Hajnóczky. 2006. 'Structural and functional features and significance of the physical linkage between ER and mitochondria', *J Cell Biol*, 174: 915-21.

Cuervo, A. M., and E. Wong. 2014. 'Chaperone-mediated autophagy: roles in disease and aging', *Cell Res*, 24: 92-104.

Danev, R., B. Buijsse, M. Khoshouei, J. M. Plitzko, and W. Baumeister. 2014. 'Volta potential phase plate for in-focus phase contrast transmission electron microscopy', *Proc Natl Acad Sci U S A*, 111: 15635-40.

Danev, R., R. M. Glaeser, and K. Nagayama. 2009. 'Practical factors affecting the performance of a thin-film phase plate for transmission electron microscopy', *Ultramicroscopy*, 109: 312-25.

de Boer, P., J. P. Hoogenboom, and B. N. Giepmans. 2015. 'Correlated light and electron microscopy: ultrastructure lights up!', *Nat Methods*, 12: 503-13.

De Mario, A., R. Quintana-Cabrera, D. Martinvalet, and M. Giacomello. 2017. '(Neuro)degenerated Mitochondria-ER contacts', *Biochem Biophys Res Commun*, 483: 1096-109.

Dell'Angelica, E. C., V. Shotelersuk, R. C. Aguilar, W. A. Gahl, and J. S. Bonifacino. 1999. 'Altered trafficking of lysosomal proteins in Hermansky-Pudlak syndrome due to mutations in the beta 3A subunit of the AP-3 adaptor', *Mol Cell*, 3: 11-21.

Demers-Lamarche, J., G. Guillebaud, M. Tlili, K. Todkar, N. Belanger, M. Grondin, A. P. Nguyen, J. Michel, and M. Germain. 2016. 'Loss of Mitochondrial Function Impairs Lysosomes', *J Biol Chem*, 291: 10263-76.

Dubochet, J., M. Adrian, J. J. Chang, J. C. Homo, J. Lepault, A. W. McDowall, and P. Schultz. 1988. 'Cryo-electron microscopy of vitrified specimens', *Q Rev Biophys*, 21: 129-228.

Dubos, A., A. Castells-Nobau, H. Meziane, M. A. Oortveld, X. Houbaert, G. Iacono, C. Martin, C. Mittelhaeuser, V. Lalanne, J. M. Kramer, A. Bhukel, C. Quentin, J. Slabbert, P. Verstreken, S. J. Sigrist, N. Messaddeq, M. C. Birling, M. Selloum, H. G. Stunnenberg, Y. Humeau, A. Schenck, and Y. Herault. 2015. 'Conditional depletion of intellectual disability and Parkinsonism candidate gene ATP6AP2 in fly and mouse induces cognitive impairment and neurodegeneration', *Hum Mol Genet*, 24: 6736-55.

Duchen, M. R. 1992. 'Ca2+-dependent changes in the mitochondrial energetics in single dissociated mouse sensory neurons', *Biochemical Journal*, 283: 41-50.

Egerton, R.F. 2016. *Physical Principles of Electron Microscopy: An Introduction to TEM, SEM, and AEM* (Springer International Publishing).

Emamzadeh, F. N. 2016. 'Alpha-synuclein structure, functions, and interactions', *J Res Med Sci*, 21: 29.

Erazo-Oliveras, A., K. Najjar, L. La Dayani, T. Y. Wang, G. A. Johnson, and J. P. Pellois. 2014. 'Protein delivery into live cells by incubation with an endosomolytic agent', *Nat Methods*, 11: 861-67.

Erazo-Oliveras, A., K. Najjar, D. Truong, T. Y. Wang, D. J. Brock, A. R. Prater, and J. P. Pellois. 2016. 'The Late Endosome and Its Lipid BMP Act as Gateways for Efficient Cytosolic Access of the Delivery Agent dfTAT and Its Macromolecular Cargos', *Cell Chem Biol*, 23: 598-607.

Fernandez-Mosquera, L., C. V. Diogo, K. F. Yambire, G. L. Santos, M. Luna Sanchez, P. Benit, P. Rustin, L. C. Lopez, I. Milosevic, and N. Raimundo. 2017. 'Acute and chronic mitochondrial respiratory chain deficiency differentially regulate lysosomal biogenesis', *Sci Rep*, 7: 45076.

Fernandez, J. J., U. Laugks, M. Schaffer, F. J. Bauerlein, M. Khoshouei, W. Baumeister, and V. Lucic. 2016. 'Removing Contamination-Induced Reconstruction Artifacts from Cryo-electron Tomograms', *Biophys J*, 110: 850-9.

Ferreira, Carlos, and William Gahl. 2016. *Lysosomal storage diseases*.

Förster, F., E. Villa, D. Thomas, A. Korinek, and W. Baumeister. 2012. '1.14 Structure Determination of Macromolecular Complexes by Cryo-Electron Microscopy in vitro and in situ.' in Edward H. Egelman (ed.), *Comprehensive Biophysics* (Elsevier: Amsterdam).

Frank, J. 2006a. *Electron Tomography: Methods for Three-Dimensional Visualization of Structures in the Cell* (Springer New York).

Frank, Joachim. 2006b. *Three-dimensional electron microscopy of macromolecular assemblies: visualization of biological molecules in their native state* (Oxford University Press).

Garcia-Mata, R., Z. Bebok, E. J. Sorscher, and E. S. Sztul. 1999. 'Characterization and dynamics of aggresome formation by a cytosolic GFP-chimera', *J Cell Biol*, 146: 1239-54.

Garcia-Mata, Rafael, Ya-Sheng Gao, and Elizabeth Sztul. 2002. 'Hassles with Taking Out the Garbage: Aggravating Aggresomes', *Traffic*, 3: 388-96.

Gerhardt, M. J., J. A. Marsh, M. Morrison, A. Kazlauskas, A. Khadka, S. Rosenkranz, M. M. DeAngelis, M. Saint-Geniez, and S. M. P. Jacobo. 2017. 'ER stress-induced aggresome trafficking of HtrA1 protects against proteotoxicity', *J Mol Cell Biol*, 9: 516-32.

Glabe, C. G. 2008. 'Structural classification of toxic amyloid oligomers', *J Biol Chem*, 283: 29639-43.

Grünewald, Kay, Ohad Medalia, Ariane Gross, Alasdair C. Steven, and Wolfgang Baumeister. 2002. 'Prospects of electron cryotomography to visualize macromolecular complexes inside cellular compartments: implications of crowding', *Biophysical Chemistry*, 100: 577-91.

Guarnieri, F. G., L. M. Arterburn, M. B. Penno, Y. Cha, and J. T. August. 1993. 'The motif Tyr-X-X-hydrophobic residue mediates lysosomal membrane targeting of lysosome-associated membrane protein 1', *J Biol Chem*, 268: 1941-6.

Guidotti, G., L. Brambilla, and D. Rossi. 2017. 'Cell-Penetrating Peptides: From Basic Research to Clinics', *Trends Pharmacol Sci*, 38: 406-24.

Guo, Q., Huang Bin, J. Cheng, M. Seefelder, T. Engler, G. Pfeifer, P. Oeckl, M. Otto, F. Moser, M. Maurer, A. Pautsch, W. Baumeister, R. Fernandez-Busnadiego, and S. Kochanek. 2018. 'The cryo-electron microscopy structure of huntingtin', *Nature*, 555: 117-20.

Guo, Q., C. Lehmer, A. Martinez-Sanchez, T. Rudack, F. Beck, H. Hartmann, M. Perez-Berlanga, F. Frottin, M. S. Hipp, F. U. Hartl, D. Edbauer, W. Baumeister, and R. Fernandez-Busnadiego. 2018. 'In Situ Structure of Neuronal C9orf72 Poly-GA Aggregates Reveals Proteasome Recruitment', *Cell*, 172: 696-705 e12.

Gutierrez, M. G., D. B. Munafo, W. Beron, and M. I. Colombo. 2004. 'Rab7 is required for the normal progression of the autophagic pathway in mammalian cells', *J Cell Sci*, 117: 2687-97.

Hamasaki, M., N. Furuta, A. Matsuda, A. Nezu, A. Yamamoto, N. Fujita, H. Oomori, T. Noda, T. Haraguchi, Y. Hiraoka, A. Amano, and T. Yoshimori. 2013. 'Autophagosomes form at ER-mitochondria contact sites', *Nature*, 495: 389-93.

Harapin, J., M. Bormel, K. T. Sapra, D. Brunner, A. Kaech, and O. Medalia. 2015. 'Structural analysis of multicellular organisms with cryo-electron tomography', *Nat Methods*, 12: 634-6.

Hardies, K., P. May, T. Djemie, O. Tarta-Arsene, T. Deconinck, D. Craiu, A. R. working group of the EuroEPINOMICS RES Consortium, I. Helbig, A. Suls, R. Balling, S. Weckhuysen, P. De Jonghe, and J. Hirst. 2015. 'Recessive loss-of-function mutations in AP4S1 cause mild fever-sensitive seizures, developmental delay and spastic paraplegia through loss of AP-4 complex assembly', *Hum Mol Genet*, 24: 2218-27.

Hardiman, O., C.P. Doherty, M. Elamin, and P. Bede. 2016. *Neurodegenerative Disorders: A Clinical Guide* (Springer International Publishing).

Hartl, F. U., A. Bracher, and M. Hayer-Hartl. 2011. 'Molecular chaperones in protein folding and proteostasis', *Nature*, 475: 324-32.

Hiltunen, M., T. van Groen, and J. Jolkkonen. 2009. 'Functional roles of amyloid-beta protein precursor and amyloid-beta peptides: evidence from experimental studies', *J Alzheimers Dis*, 18: 401-12.

Hipp, M. S., S. H. Park, and F. U. Hartl. 2014. 'Proteostasis impairment in protein-misfolding and -aggregation diseases', *Trends Cell Biol*, 24: 506-14.

Hooke, R. 1665. *Micrographia* (Science Heritage).

Hosp, F., S. Gutierrez-Angel, M. H. Schaefer, J. Cox, F. Meissner, M. S. Hipp, F. U. Hartl, R. Klein, I. Dudanova, and M. Mann. 2017. 'Spatiotemporal Proteomic Profiling of Huntington's Disease Inclusions Reveals Widespread Loss of Protein Function', *Cell Rep*, 21: 2291-303.

Hrabe, Thomas, Yuxiang Chen, Stefan Pfeffer, Luis Kuhn Cuellar, Ann-Victoria Mangold, and Friedrich Förster. 2012. 'PyTom: A python-based toolbox for localization of macromolecules in cryo-electron tomograms and subtomogram analysis', *J Struct Biol*, 178: 177-88.

Hubbard, V. M., R. Valdor, F. Macian, and A. M. Cuervo. 2012. 'Selective autophagy in the maintenance of cellular homeostasis in aging organisms', *Biogerontology*, 13: 21-35.

Huizing, Marjan, Yair Anikster, and William A. Gahl. 2000. 'Hermansky-Pudlak Syndrome and Related Disorders of Organelle Formation', *Traffic*, 1: 823-35.

Humphries IV, William H, Craig J Szymanski, and Christine K Payne. 2011. 'Endo-lysosomal vesicles positive for Rab7 and LAMP1 are terminal vesicles for the transport of dextran', *PLoS One*, 6: e26626.

Iwata, A., J. C. Christianson, M. Bucci, L. M. Ellerby, N. Nukina, L. S. Forno, and R. R. Kopito. 2005. 'Increased susceptibility of cytoplasmic over nuclear polyglutamine aggregates to autophagic degradation', *Proc Natl Acad Sci U S A*, 102: 13135-40.

Jager, S., C. Bucci, I. Tanida, T. Ueno, E. Kominami, P. Saftig, and E. L. Eskelinen. 2004. 'Role for Rab7 in maturation of late autophagic vacuoles', *J Cell Sci*, 117: 4837-48.

Johnston, J. A., C. L. Ward, and R. R. Kopito. 1998. 'Aggresomes: a cellular response to misfolded proteins', *J Cell Biol*, 143: 1883-98.

Journet, A., A. Chapel, S. Kieffer, F. Roux, and J. Garin. 2002. 'Proteomic analysis of human lysosomes: application to monocytic and breast cancer cells', *Proteomics*, 2: 1026-40.

Kabeya, Y., N. Mizushima, T. Ueno, A. Yamamoto, T. Kirisako, T. Noda, E. Kominami, Y. Ohsumi, and T. Yoshimori. 2000. 'LC3, a mammalian homologue of yeast Apg8p, is localized in autophagosome membranes after processing', *Embo j*, 19: 5720-8.

Kaganovich, D., R. Kopito, and J. Frydman. 2008. 'Misfolded proteins partition between two distinct quality control compartments', *Nature*, 454: 1088-95.

Kang, R., H. J. Zeh, M. T. Lotze, and D. Tang. 2011. 'The Beclin 1 network regulates autophagy and apoptosis', *Cell Death Differ*, 18: 571-80.

Kantheti, P., X. Qiao, M. E. Diaz, A. A. Peden, G. E. Meyer, S. L. Carskadon, D. Kapfhamer, D. Sufalko, M. S. Robinson, J. L. Noebels, and M. Burmeister. 1998. 'Mutation in AP-3 delta in the mocha mouse links endosomal transport to storage deficiency in platelets, melanosomes, and synaptic vesicles', *Neuron*, 21: 111-22.

Karch, C. M., and A. M. Goate. 2015. 'Alzheimer's disease risk genes and mechanisms of disease pathogenesis', *Biol Psychiatry*, 77: 43-51.

Kaushik, S., and A. M. Cuervo. 2012. 'Chaperone-mediated autophagy: a unique way to enter the lysosome world', *Trends Cell Biol*, 22: 407-17.

Khatter, H., A. G. Myasnikov, S. K. Natchiar, and B. P. Klaholz. 2015. 'Structure of the human 80S ribosome', *Nature*, 520: 640-5.

Khoshouei, Maryam, Mazdak Radjainia, Wolfgang Baumeister, and Radostin Danev. 2017. 'Cryo-EM structure of haemoglobin at 3.2 Å determined with the Volta phase plate', *Nat Commun*, 8: 16099.

Kim, Y. E., F. Hosp, F. Frottin, H. Ge, M. Mann, M. Hayer-Hartl, and F. U. Hartl. 2016. 'Soluble Oligomers of PolyQ-Expanded Huntingtin Target a Multiplicity of Key Cellular Factors', *Mol Cell*, 63: 951-64.

Klaips, C. L., G. G. Jayaraj, and F. U. Hartl. 2018. 'Pathways of cellular proteostasis in aging and disease', *J Cell Biol*, 217: 51-63.

Kohn, G., N. Livni, A. Ornoy, E. Sekeles, Y. Beyth, C. Legum, G. Bach, and M. M. Cohen. 1977. 'Prenatal diagnosis of mucolipidosis IV by electron microscopy', *J Pediatr*, 90: 62-6.

Komatsu, M., S. Waguri, T. Chiba, S. Murata, J. Iwata, I. Tanida, T. Ueno, M. Koike, Y. Uchiyama, E. Kominami, and K. Tanaka. 2006. 'Loss of autophagy in the central nervous system causes neurodegeneration in mice', *Nature*, 441: 880-4.

Kononenko, N. L., G. A. Classen, M. Kuijpers, D. Puchkov, T. Maritzen, A. Tempes, A. R. Malik, A. Skalecka, S. Bera, J. Jaworski, and V. Haucke. 2017. 'Retrograde transport of TrkB-containing autophagosomes via the adaptor AP-2 mediates neuronal complexity and prevents neurodegeneration', *Nat Commun*, 8: 14819.

Kremer, J. R., D. N. Mastronarde, and J. R. McIntosh. 1996. 'Computer visualization of three-dimensional image data using IMOD', *J Struct Biol*, 116: 71-6.

Labbadia, J., and R. I. Morimoto. 2015. 'The biology of proteostasis in aging and disease', *Annu Rev Biochem*, 84: 435-64.

Lee, H. J., S. Y. Shin, C. Choi, Y. H. Lee, and S. J. Lee. 2002. 'Formation and removal of alpha-synuclein aggregates in cells exposed to mitochondrial inhibitors', *J Biol Chem*, 277: 5411-7.

Lee, J. H., W. H. Yu, A. Kumar, S. Lee, P. S. Mohan, C. M. Peterhoff, D. M. Wolfe, M. Martinez-Vicente, A. C. Massey, G. Sovak, Y. Uchiyama, D. Westaway, A. M. Cuervo, and R. A. Nixon. 2010. 'Lysosomal proteolysis and autophagy require presenilin 1 and are disrupted by Alzheimer-related PS1 mutations', *Cell*, 141: 1146-58.

Leitner, A., L. A. Joachimiak, A. Bracher, L. Monkemeyer, T. Walzthoeni, B. Chen, S. Pechmann, S. Holmes, Y. Cong, B. Ma, S. Ludtke, W. Chiu, F. U. Hartl, R. Aebersold, and J. Frydman. 2012. 'The molecular architecture of the eukaryotic chaperonin TRiC/CCT', *Structure*, 20: 814-25.

Levy, R., U. Shaheen, Y. Cesbron, and V. See. 2010. 'Gold nanoparticles delivery in mammalian live cells: a critical review', *Nano Rev*, 1: 10.3402/nano.v1i0.4889.

Li, J. L., L. Wang, X. Y. Liu, Z. P. Zhang, H. C. Guo, W. M. Liu, and S. H. Tang. 2009. 'In vitro cancer cell imaging and therapy using transferrin-conjugated gold nanoparticles', *Cancer Lett*, 274: 319-26.

Li, X., P. Mooney, S. Zheng, C. R. Booth, M. B. Braunfeld, S. Gubbens, D. A. Agard, and Y. Cheng. 2013. 'Electron counting and beam-induced motion correction enable near-atomic-resolution single-particle cryo-EM', *Nat Methods*, 10: 584-90.

Liu, C. J., C. H. Wang, C. C. Chien, T. Y. Yang, S. T. Chen, W. H. Leng, C. F. Lee, K. H. Lee, Y. Hwu, Y. C. Lee, C. L. Cheng, C. S. Yang, Y. J. Chen, J. H. Je, and G. Margaritondo. 2008. 'Enhanced x-ray irradiation-induced cancer cell damage by gold nanoparticles treated by a new synthesis method of polyethylene glycol modification', *Nanotechnology*, 19: 295104.

Lucic, V., F. Forster, and W. Baumeister. 2005. 'Structural studies by electron tomography: from cells to molecules', *Annu Rev Biochem*, 74: 833-65.

Mahamid, J., R. Schampers, H. Persoon, A. A. Hyman, W. Baumeister, and J. M. Plitzko. 2015. 'A focused ion beam milling and lift-out approach for site-specific preparation of frozen-hydrated lamellas from multicellular organisms', *J Struct Biol*, 192: 262-9.

Mardones, G. A., P. V. Burgos, Y. Lin, D. P. Kloer, J. G. Magadan, J. H. Hurley, and J. S. Bonifacino. 2013. 'Structural basis for the recognition of tyrosine-based sorting signals by the mu3A subunit of the AP-3 adaptor complex', *J Biol Chem*, 288: 9563-71.

Martina, J. A., H. I. Diab, L. Lishu, A. L. Jeong, S. Patange, N. Raben, and R. Puertollano. 2014. 'The nutrient-responsive transcription factor TFE3 promotes autophagy, lysosomal biogenesis, and clearance of cellular debris', *Sci Signal*, 7: ra9.

Martinez-Sanchez, A., I. Garcia, S. Asano, V. Lucic, and J. J. Fernandez. 2014. 'Robust membrane detection based on tensor voting for electron tomography', *J Struct Biol*, 186: 49-61.

Mastronarde, D. N. 2005. 'Automated electron microscope tomography using robust prediction of specimen movements', *J Struct Biol*, 152: 36-51.

Mathews, P. M., C. B. Guerra, Y. Jiang, O. M. Grbovic, B. H. Kao, S. D. Schmidt, R. Dinakar, M. Mercken, A. Hille-Rehfeld, J. Rohrer, P. Mehta, A. M. Cataldo, and R. A. Nixon. 2002. 'Alzheimer's disease-related overexpression of the cation-dependent mannose 6-phosphate receptor increases Abeta secretion: role for altered lysosomal hydrolase distribution in beta-amyloidogenesis', *J Biol Chem*, 277: 5299-307.

May, S., D. Hornburg, M. H. Schludi, T. Arzberger, K. Rentzsch, B. M. Schwenk, F. A. Grasser, K. Mori, E. Kremmer, J. Banzhaf-Strathmann, M. Mann, F. Meissner, and D. Edbauer. 2014. 'C9orf72 FTLD/ALS-associated Gly-Ala dipeptide repeat proteins cause neuronal toxicity and Unc119 sequestration', *Acta Neuropathol*, 128: 485-503.

Maynard-Smith, L. A., L. C. Chen, L. A. Banaszynski, A. G. L. Ooi, and T. J. Wandless. 2007. 'A directed approach for engineering conditional protein stability using biologically silent small molecules', *Journal of Biological Chemistry*, 282: 24866-72.

Mazzulli, J. R., F. Zunke, O. Isacson, L. Studer, and D. Krainc. 2016. 'alpha-Synuclein-induced lysosomal dysfunction occurs through disruptions in protein trafficking in human midbrain synucleinopathy models', *Proc Natl Acad Sci U S A*, 113: 1931-6.

Mazzulli, J. R., F. Zunke, T. Tsunemi, N. J. Toker, S. Jeon, L. F. Burbulla, S. Patnaik, E. Sidransky, J. J. Marugan, C. M. Sue, and D. Krainc. 2016. 'Activation of beta-Glucocerebrosidase Reduces Pathological alpha-Synuclein and Restores Lysosomal Function in Parkinson's Patient Midbrain Neurons', *J Neurosci*, 36: 7693-706.

Menzies, F. M., A. Fleming, A. Caricasole, C. F. Bento, S. P. Andrews, A. Ashkenazi, J. Fullgrabe, A. Jackson, M. Jimenez Sanchez, C. Karabiyik, F. Licitra, A. Lopez Ramirez, M. Pavel, C. Puri, M. Renna, T. Ricketts, L. Schlotawa, M. Vicinanza, H. Won, Y. Zhu, J. Skidmore, and D. C. Rubinsztein. 2017. 'Autophagy and Neurodegeneration: Pathogenic Mechanisms and Therapeutic Opportunities', *Neuron*, 93: 1015-34.

Menzies, F. M., A. Fleming, and D. C. Rubinsztein. 2015. 'Compromised autophagy and neurodegenerative diseases', *Nat Rev Neurosci*, 16: 345-57.

Merk, Alan, Alberto Bartesaghi, Soojay Banerjee, Veronica Falconieri, Prashant Rao, Mindy I. Davis, Rajan Pragani, Matthew B. Boxer, Lesley A. Earl, Jacqueline L. S. Milne, and Sriram Subramaniam. 2016. 'Breaking Cryo-EM Resolution Barriers to Facilitate Drug Discovery', *Cell*, 165: 1698-707.

Metaxakis, A., C. Ploumi, and N. Tavernarakis. 2018. 'Autophagy in Age-Associated Neurodegeneration', *Cells*, 7.

Milanesi, L., T. Sheynis, W. F. Xue, E. V. Orlova, A. L. Hellewell, R. Jelinek, E. W. Hewitt, S. E. Radford, and H. R. Saibil. 2012. 'Direct three-dimensional visualization of membrane disruption by amyloid fibrils', *Proc Natl Acad Sci U S A*, 109: 20455-60.

Miyazaki, Y., K. Mizumoto, G. Dey, T. Kudo, J. Perrino, L. C. Chen, T. Meyer, and T. J. Wandless. 2016. 'A method to rapidly create protein aggregates in living cells', *Nat Commun*, 7: 11689.

Mizushima, N., T. Noda, T. Yoshimori, Y. Tanaka, T. Ishii, M. D. George, D. J. Klionsky, M. Ohsumi, and Y. Ohsumi. 1998. 'A protein conjugation system essential for autophagy', *Nature*, 395: 395-8.

Mizushima, N., and T. Yoshimori. 2007. 'How to interpret LC3 immunoblotting', *Autophagy*, 3: 542-5.

Moor, Hans. 1987. 'Theory and Practice of High Pressure Freezing.' in Rudolf Alexander Steinbrecht and Karl Zierold (eds.), *Cryotechniques in Biological Electron Microscopy* (Springer Berlin Heidelberg: Berlin, Heidelberg).

Munroe, P. R. 2009. 'The application of focused ion beam microscopy in the material sciences', *Materials Characterization*, 60: 2-13.

Najjar, K., A. Erazo-Oliveras, and J. P. Pellois. 2015. 'Delivery of Proteins, Peptides or Cell-impermeable Small Molecules into Live Cells by Incubation with the Endosomolytic Reagent dfTAT', *J Vis Exp*.

Nakatani, Y., N. Nakamura, J. Sano, Y. Inayama, N. Kawano, S. Yamanaka, Y. Miyagi, Y. Nagashima, C. Ohbayashi, M. Mizushima, T. Manabe, M. Kuroda, T. Yokoi, and O. Matsubara. 2000. 'Interstitial pneumonia in Hermansky-Pudlak syndrome: significance of florid foamy swelling/degeneration (giant lamellar body degeneration) of type-2 pneumocytes', *Virchows Arch*, 437: 304-13.

Nakatsu, F., M. Okada, F. Mori, N. Kumazawa, H. Iwasa, G. Zhu, Y. Kasagi, H. Kamiya, A. Harada, K. Nishimura, A. Takeuchi, T. Miyazaki, M. Watanabe, S. Yuasa, T. Manabe, K. Wakabayashi, S. Kaneko, T. Saito, and H. Ohno. 2004. 'Defective function of GABA-containing synaptic vesicles in mice lacking the AP-3B clathrin adaptor', *J Cell Biol*, 167: 293-302.

Naon, Deborah, and Luca Scorrano. 2014. 'At the right distance: ER-mitochondria juxtaposition in cell life and death', *Biochimica et Biophysica Acta (BBA) - Molecular Cell Research*, 1843: 2184-94.

Nativo, P., I. A. Prior, and M. Brust. 2008. 'Uptake and intracellular fate of surface-modified gold nanoparticles', *ACS nano*, 2: 1639-44.

Nixon, R. A. 2007. 'Autophagy, amyloidogenesis and Alzheimer disease', *J Cell Sci*, 120: 4081-91.

———. 2013. 'The role of autophagy in neurodegenerative disease', *Nat Med*, 19: 983-97.

———. 2017. 'Amyloid precursor protein and endosomal-lysosomal dysfunction in Alzheimer's disease: inseparable partners in a multifactorial disease', *FASEB J*, 31: 2729-43.

Nixon, R. A., J. Wegiel, A. Kumar, W. H. Yu, C. Peterhoff, A. Cataldo, and A. M. Cuervo. 2005. 'Extensive involvement of autophagy in Alzheimer disease: an immuno-electron microscopy study', *J Neuropathol Exp Neurol*, 64: 113-22.

Nopoulos, P. C. 2016. 'Huntington disease: a single-gene degenerative disorder of the striatum', *Dialogues Clin Neurosci*, 18: 91-8.

Ochaba, J., T. Lukacsovich, G. Csikos, S. Zheng, J. Margulis, L. Salazar, K. Mao, A. L. Lau, S. Y. Yeung, S. Humbert, F. Saudou, D. J. Klionsky, S. Finkbeiner, S. O. Zeitlin, J. L. Marsh, D. E. Housman, L. M. Thompson, and J. S. Steffan. 2014. 'Potential function for the Huntingtin protein as a scaffold for selective autophagy', *Proc Natl Acad Sci U S A*, 111: 16889-94.

Ogrodnik, M., H. Salmonowicz, R. Brown, J. Turkowska, W. Sredniawa, S. Pattabiraman, T. Amen, A. C. Abraham, N. Eichler, R. Lyakhovetsky, and D. Kaganovich. 2014. 'Dynamic JUNQ inclusion bodies are asymmetrically inherited in mammalian cell lines through the asymmetric partitioning of vimentin', *Proc Natl Acad Sci U S A*, 111: 8049-54.

Ohno, H., R. C. Aguilar, D. Yeh, D. Taura, T. Saito, and J. S. Bonifacino. 1998. 'The medium subunits of adaptor complexes recognize distinct but overlapping sets of tyrosine-based sorting signals', *J Biol Chem*, 273: 25915-21.

Olzscha, H., S. M. Schermann, A. C. Woerner, S. Pinkert, M. H. Hecht, G. G. Tartaglia, M. Vendruscolo, M. Hayer-Hartl, F. U. Hartl, and R. M. Vabulas. 2011. 'Amyloid-like aggregates sequester numerous metastable proteins with essential cellular functions', *Cell*, 144: 67-78.

Park, S. H., Y. Kukushkin, R. Gupta, T. Chen, A. Konagai, M. S. Hipp, M. Hayer-Hartl, and F. U. Hartl. 2013. 'PolyQ proteins interfere with nuclear degradation of cytosolic proteins by sequestering the Sis1p chaperone', *Cell*, 154: 134-45.

Pathak, D., A. Berthet, and K. Nakamura. 2013. 'Energy failure: does it contribute to neurodegeneration?', *Ann Neurol*, 74: 506-16.

Peden, A. A., V. Oorschot, B. A. Hesser, C. D. Austin, R. H. Scheller, and J. Klumperman. 2004. 'Localization of the AP-3 adaptor complex defines a novel endosomal exit site for lysosomal membrane proteins', *J Cell Biol*, 164: 1065-76.

Platt, F. M. 2014. 'Sphingolipid lysosomal storage disorders', *Nature*, 510: 68-75.

Raben, Nina, Lauren Shea, Victoria Hill, and Paul Plotz. 2009. 'Chapter 21 Monitoring Autophagy in Lysosomal Storage Disorders', *Methods Enzymol*, 453: 417-49.

Raimundo, N., S. Vanharanta, L. A. Aaltonen, I. Hovatta, and A. Suomalainen. 2009. 'Downregulation of SRF-FOS-JUNB pathway in fumarate hydratase deficiency and in uterine leiomyomas', *Oncogene*, 28: 1261-73.

Raturi, A., and T. Simmen. 2013. 'Where the endoplasmic reticulum and the mitochondrion tie the knot: the mitochondria-associated membrane (MAM)', *Biochim Biophys Acta*, 1833: 213-24.

Reimer, L., and H. Kohl. 2008. *Transmission Electron Microscopy: Physics of Image Formation* (Springer New York).

Rigort, A., F. J. Bauerlein, A. Leis, M. Gruska, C. Hoffmann, T. Laugks, U. Bohm, M. Eibauer, H. Gnaegi, W. Baumeister, and J. M. Plitzko. 2010. 'Micromachining tools and correlative approaches for cellular cryo-electron tomography', *J Struct Biol*, 172: 169-79.

Rigort, A., F. J. Bauerlein, E. Villa, M. Eibauer, T. Laugks, W. Baumeister, and J. M. Plitzko. 2012. 'Focused ion beam micromachining of eukaryotic cells for cryoelectron tomography', *Proc Natl Acad Sci U S A*, 109: 4449-54.

Robak, L. A., I. E. Jansen, J. van Rooij, A. G. Uitterlinden, R. Kraaij, J. Jankovic, Consortium International Parkinson's Disease Genomics, P. Heutink, and J. M. Shulman. 2017. 'Excessive burden of lysosomal storage disorder gene variants in Parkinson's disease', *Brain*, 140: 3191-203.

Roczniak-Ferguson, A., C. S. Petit, F. Froehlich, S. Qian, J. Ky, B. Angarola, T. C. Walther, and S. M. Ferguson. 2012. 'The transcription factor TFEB links mTORC1 signaling to transcriptional control of lysosome homeostasis', *Sci Signal*, 5: ra42.

Rottenberg, H., and A. Scarpa. 1974. 'Calcium uptake and membrane potential in mitochondria', *Biochemistry*, 13: 4811-7.

Rubinsztein, D. C., T. Shpilka, and Z. Elazar. 2012. 'Mechanisms of autophagosome biogenesis', *Curr Biol*, 22: R29-34.

Ruskin, R. S., Z. Yu, and N. Grigorieff. 2013. 'Quantitative characterization of electron detectors for transmission electron microscopy', *J Struct Biol*, 184: 385-93.

Saftig, P., and J. Klumperman. 2009. 'Lysosome biogenesis and lysosomal membrane proteins: trafficking meets function', *Nat Rev Mol Cell Biol*, 10: 623-35.

Sartori, Anna, Rudolf Gatz, Florian Beck, Alexander Rigort, Wolfgang Baumeister, and Juergen M. Plitzko. 2007. 'Correlative microscopy: Bridging the gap between fluorescence light microscopy and cryo-electron tomography', *J Struct Biol*, 160: 135-45.

Saudou, F., and S. Humbert. 2016. 'The Biology of Huntingtin', *Neuron*, 89: 910-26.

Sawyer, L., D. Grubb, and G.F. Meyers. 2008. *Polymer Microscopy* (Springer New York).

Schindelin, J., I. Arganda-Carreras, E. Frise, V. Kaynig, M. Longair, T. Pietzsch, S. Preibisch, C. Rueden, S. Saalfeld, B. Schmid, J. Y. Tinevez, D. J. White, V. Hartenstein, K. Eliceiri, P. Tomancak, and A. Cardona. 2012. 'Fiji: an open-source platform for biological-image analysis', *Nat Methods*, 9: 676-82.

Sendtner, M. 2014. 'Motoneuron disease', *Handb Exp Pharmacol*, 220: 411-41.

Singh, S. K., S. Srivastav, A. K. Yadav, S. Srikrishna, and G. Perry. 2016. 'Overview of Alzheimer's Disease and Some Therapeutic Approaches Targeting Abeta by Using Several Synthetic and Herbal Compounds', *Oxid Med Cell Longev*, 2016: 7361613.

Skikne, M. I., I. Prinsloo, and I. Webster. 1972. 'Electron microscopy of lung in Niemann-Pick disease', *J Pathol*, 106: 119-22.

Słabicki, Mikołaj, Mirko Theis, Dragomir B Krastev, Sergey Samsonov, Emeline Mundwiller, Magno Junqueira, Maciej Paszkowski-Rogacz, Joan Teyra, Anne-Kristin Heninger, and Ina Poser. 2010. 'A genome-scale DNA repair RNAi screen identifies SPG48 as a novel gene associated with hereditary spastic paraplegia', *PLoS Biol*, 8: e1000408.

Sokolova, A. V., L. Kreplak, T. Wedig, N. Mucke, D. I. Svergun, H. Herrmann, U. Aebi, and S. V. Strelkov. 2006. 'Monitoring intermediate filament assembly by small-angle x-ray scattering reveals the molecular architecture of assembly intermediates', *Proc Natl Acad Sci U S A*, 103: 16206-11.

Sosinsky, Gina E., John Crum, Ying Z. Jones, Jason Lanman, Benjamin Smarr, Masako Terada, Maryann E. Martone, Thomas J. Deerinck, John E. Johnson, and Mark H. Ellisman. 2008. 'The Combination of Chemical Fixation Procedures with High Pressure Freezing and Freeze Substitution Preserves Highly Labile Tissue Ultrastructure for Electron Tomography Applications', *J Struct Biol*, 161: 359-71.

Stoica, Radu, Kurt J De Vos, Sébastien Paillusson, Sarah Mueller, Rosa M Sancho, Kwok-Fai Lau, Gema Vizcay-Barrena, Wen-Lang Lin, Ya-Fei Xu, and Jada Lewis. 2014. 'ER–mitochondria associations are regulated by the VAPB–PTPIP51 interaction and are disrupted by ALS/FTD-associated TDP-43', *Nat Commun*, 5: 3996.

Studer, Daniel, Bruno M. Humbel, and Matthias Chiquet. 2008. 'Electron microscopy of high pressure frozen samples: bridging the gap between cellular ultrastructure and atomic resolution', *Histochem Cell Biol*, 130: 877-89.

Tanida, Isei, Tomohito Nishitani, Takahiro Nemoto, Takashi Ueno, and Eiki Kominami. 2002. 'Mammalian Apg12p, but not the Apg12p·Apg5p conjugate, facilitates LC3 processing', *Biochem Biophys Res Commun*, 296: 1164-70.

Taylor, J. P., J. Hardy, and K. H. Fischbeck. 2002. 'Toxic proteins in neurodegenerative disease', *Science*, 296: 1991-5.

Toyoshima, C., and N. Unwin. 1988. 'Contrast transfer for frozen-hydrated specimens: determination from pairs of defocused images', *Ultramicroscopy*, 25: 279-91.

Verfaillie, T., N. Rubio, A. D. Garg, G. Bultynck, R. Rizzuto, J. P. Decuypere, J. Piette, C. Linehan, S. Gupta, A. Samali, and P. Agostinis. 2012. 'PERK is required at the ER-mitochondrial contact sites to convey apoptosis after ROS-based ER stress', *Cell Death And Differentiation*, 19: 1880-91.

Wagner, J., M. Schaffer, and R. Fernandez-Busnadiego. 2017. 'Cryo-electron tomography-the cell biology that came in from the cold', *FEBS Lett*, 591: 2520-33.

Wang, C., M. A. Telpoukhovskaia, B. A. Bahr, X. Chen, and L. Gan. 2018. 'Endo-lysosomal dysfunction: a converging mechanism in neurodegenerative diseases', *Curr Opin Neurobiol*, 48: 52-58.

Wang, Y., and E. Mandelkow. 2016. 'Tau in physiology and pathology', *Nat Rev Neurosci*, 17: 5-21.

West, M. W., W. Wang, J. Patterson, J. D. Mancias, J. R. Beasley, and M. H. Hecht. 1999. 'De novo amyloid proteins from designed combinatorial libraries', *Proc Natl Acad Sci U S A*, 96: 11211-6.

Whitworth, A. J., and L. J. Pallanck. 2017. 'PINK1/Parkin mitophagy and neurodegeneration-what do we really know in vivo?', *Curr Opin Genet Dev*, 44: 47-53.

WHO. 2015. 'http://www.who.int/features/factfiles/dementia/en/'.

Williams, D.B., and C.B. Carter. 2009. *Transmission Electron Microscopy: A Textbook for Materials Science* (Springer US).

Williamson, W. R., and P. R. Hiesinger. 2010. 'On the role of v-ATPase V0a1-dependent degradation in Alzheimer disease', *Commun Integr Biol*, 3: 604-7.

Winklhofer, K. F., J. Tatzelt, and C. Haass. 2008. 'The two faces of protein misfolding: gain- and loss-of-function in neurodegenerative diseases', *Embo j*, 27: 336-49.

Woerner, A. C., F. Frottin, D. Hornburg, L. R. Feng, F. Meissner, M. Patra, J. Tatzelt, M. Mann, K. F. Winklhofer, F. U. Hartl, and M. S. Hipp. 2016. 'Cytoplasmic protein aggregates interfere with nucleocytoplasmic transport of protein and RNA', *Science*, 351: 173-6.

Wong, E., and A. M. Cuervo. 2010. 'Autophagy gone awry in neurodegenerative diseases', *Nat Neurosci*, 13: 805-11.

Wong, Y. C., and E. L. Holzbaur. 2014. 'The regulation of autophagosome dynamics by huntingtin and HAP1 is disrupted by expression of mutant huntingtin, leading to defective cargo degradation', *J Neurosci*, 34: 1293-305.

Wyss-Coray, T., and J. Rogers. 2012. 'Inflammation in Alzheimer disease-a brief review of the basic science and clinical literature', *Cold Spring Harb Perspect Med*, 2: a006346.

Xiao, Q., P. Yan, X. Ma, H. Liu, R. Perez, A. Zhu, E. Gonzales, D. L. Tripoli, L. Czerniewski, A. Ballabio, J. R. Cirrito, A. Diwan, and J. M. Lee. 2015. 'Neuronal-Targeted TFEB Accelerates Lysosomal Degradation of APP, Reducing Abeta Generation and Amyloid Plaque Pathogenesis', *J Neurosci*, 35: 12137-51.

Xie, Zhiping, and Daniel Klionsky. 2007. *Autophagosome formation: core machinery and adaptations*.

Xiong, H. Y., B. L. Buckwalter, H. M. Shieh, and M. H. Hecht. 1995. 'Periodicity of Polar and Nonpolar Amino-Acids Is the Major Determinant of Secondary Structure in Self-Assembling Oligomeric Peptides', *Proc Natl Acad Sci U S A*, 92: 6349-53.

Yang, H., and H. Y. Hu. 2016. 'Sequestration of cellular interacting partners by protein aggregates: implication in a loss-of-function pathology', *FEBS J*, 283: 3705-17.

Yang, P. H., X. Sun, J. F. Chiu, H. Sun, and Q. Y. He. 2005. 'Transferrin-mediated gold nanoparticle cellular uptake', *Bioconjug Chem*, 16: 494-6.

Yang, W., C. Li, D. M. Ward, J. Kaplan, and S. L. Mansour. 2000. 'Defective organellar membrane protein trafficking in Ap3b1-deficient cells', *J Cell Sci*, 113 (Pt 22): 4077-86.

Yu, A., Y. Shibata, B. Shah, B. Calamini, D. C. Lo, and R. I. Morimoto. 2014. 'Protein aggregation can inhibit clathrin-mediated endocytosis by chaperone competition', *Proc Natl Acad Sci U S A*, 111: E1481-90.

Zhen, L., S. Jiang, L. Feng, N. A. Bright, A. A. Peden, A. B. Seymour, E. K. Novak, R. Elliott, M. B. Gorin, M. S. Robinson, and R. T. Swank. 1999. 'Abnormal expression and subcellular distribution of subunit proteins of the AP-3 adaptor complex lead to platelet storage pool deficiency in the pearl mouse', *Blood*, 94: 146-55.

Zuber, B., I. Nikonenko, P. Klauser, D. Muller, and J. Dubochet. 2005. 'The mammalian central nervous synaptic cleft contains a high density of periodically organized complexes', *Proc Natl Acad Sci U S A*, 102: 19192-7.

6. List of Abbreviations

3D	Three-dimensional
AA	Amino acid
AD	Alzheimer's disease
AgDD	Aggregating destabilizing domain
Agg	Aggregate
ALS	Amyotrophic lateral sclerosis
AP	Adaptor protein
ATP	Adenosine triphosphate
ATPaseV	V-type ATPase
BCN1	Beclin-1
BSA	Bovine Serum Albumin
CCD	Charge coupled device
CFTR	Cystic fibrosis transmembrane conductance regulator
CTF	Contrast transfer function
CTS	Cathepsin
DAPI	4',6-diamidino-2-phenylindole
DD	Destabilizing domain
dfTAT	Dimerized fluorescent trans-activator of transcription
DMEM	Dulbecco's modified Eagle's medium
DMSO	Dimethyl sulfoxide
DNA	Deoxyribonucleic acid
En	Endosome
ER	Endoplasmic reticulum
ER-GFP	Endoplasmic reticulum targeted green fluorescent protein
FBS	Fetal Bovine Serum
FCCP	Carbonyl cyanide-4-(trifluoromethoxy)phenylhydrazone
FEG	Field emission gun
FIB	Focused ion beam
FIB/SEM	Focused ion beam & scanning electron microscope
FITC	Fluorescein isothiocyanate
FLM	Fluorescence light microscope
GFP	Green fluorescent protein
HBSS	Hanks’ balanced salt solution
HD	Huntington's disease
HEK	Human embryonic kidney cells
HEXA	Hexosaminidase A
HPF	High pressure freezing
HPRT	Hypoxanthine-guanine phosphoribosyltransferase
HtrA1	High temperature requirement A1
IC	Ice contamination
ILV	Intraluminal vesicle
L-15	Leibovitz's L-15
LAMP1	Lysosomal-associated membrane protein 1

LC3	Cytosolic Microtubule-associated protein 1A/1B-light chain 3
LC3-II	Cytosolic Microtubule-associated protein 1A/1B-light chain 3 phosphatidylethanolamine conjugate
LE	Late endosome
LM	Light microscope
LSD	Lysosomal storage disease
Lys	Lysosome
MCOLN1	Mucolipin-1
MCS	Membrane contact site
MEM	Minimal essential medium
Mit	Mitochondrion
MMP	Mitochondrial membrane potential
MPI	Max Planck Institute
NA	Numerical aperture
NDD	Neurodegenerative diseases
NPC	Nuclear pore complex
Nuc	Nucleus
PBS	Phosphate-buffered saline
PD	Parkinson's disease
PDB	Protein data bank
PM	Plasma membrane
PN	Proteostasis network
PVDF	Polyvinylidene fluoride
qPCR	Quantitative polymerase chain reaction
rDD	Recombinant destabilizing domain
RNA	Ribonucleic acid
ROI	Region of interest
S1	Shield-1
SDS	Sodium dodecyl sulfate
SEM	Scanning electron microscope
SQSTM1	Sequestosome-1
TAT	Trans-activator of transcription
TEM	Transmission electron microscope
TFEB	Transcription factor EB
TRiC	TCP-1 Ring Complexes
UPS	Ubiquitin-proteasome system
VPP	Volta phase plate
Z-FR-R110	Rhodamine 110, bis-(N-CBZ-L-phenylalanyl-L-arginine amide), dihydrochloride

Acknowledgements

I would like to thank the many people without whom this thesis would have not been possible. I would like to thank all the members of the department, especially of our group, for the great working atmosphere. In particular, I would like to thank my direct supervisor Dr. Ruben Fernandez-Busnadiego, who taught me the basics of cryo-electron tomography and has supported me throughout my time as a PhD student with his foresight, ideas and helpful advice.

I thank Prof. Dr. Wolfgang Baumeister for providing me the opportunity to hone my skills in microscopy in an excellent environment of top end equipment and skill- and helpful colleagues.

I would like to acknowledge my thesis advisory committee members for their helpful comments during our meetings: Prof. Dr. Wolfgang Baumeister, Dr. Ruben Fernandez-Busnadiego, Prof. Dr. Petra Schwille and Dr. Irina Dudanova.

I also acknowledge our collaborators Dr. Archana Mishra, Irene Riera Tur and Dr. Irina Dudanova from the lab of Prof. Dr. Rüdiger Klein at the MPI of Neurobiology, Dr. Daniel Hornburg from the lab of Prof. Dr. Matthias Mann at the MPI of Biochemistry and the lab of Dr. Nuno Raimundo at the University of Göttingen.

I am grateful to Felix Bäuerlein, Dr. Miroslava Schaffer, Dr. Qiang Guo, Günter Pfeifer and Prof. Dr. Juergen Plitzko for teaching me the details of cryo-EM and for providing advice and a helpful hand when things had gone awry. I also thank Jan, Fabian, Markus, Philip, Laura and Victoria for their support and the good times in the department.

Finally I thank my family for all their support during my studies. I especially thank my wife Isabelle for her encouragement when I encountered setbacks and her helpful insight on how to tackle scientific issues when they arose. Thanks for always being there for me!